Technische Universität München

TUM School of Natural Sciences

Structural investigation of Serum Amyloid A fibrils using solid-state NMR and the effect of Heparin on SAA aggregation

Arpita Sundaria

Vollständiger Abdruck der von der TUM School of Natural Sciences der Technischen Universität München zur Erlangung einer

Doktorin der Naturwissenschaften (Dr. rer. nat.)

genehmigten Dissertation.

Vorsitz: Priv.-Doz. Dr. Gerd Gemmecker

Prüfer der Dissertation:

1. Prof. Dr. Bernd Reif
2. Prof. Dr. Franz Hagn

Die Dissertation wurde am 26.06.2023 bei der Technischen Universität München eingereicht und durch die TUM School of Natural Sciences am 08.08.2023 angenommen.

Contents

Acknowledgments vi

Abbreviations viii

1. Summary x

1.1 Summary x

1.2 Zusammenfassung xii

2. Introduction 1

2.1 Proteins 1

2.2 Diseases related to amyloidosis 4

2.3 Systemic amyloidosis 5

2.3.1 AL amyloidosis 6

2.3.2 ATTR amyloidosis 6

2.3.3 Aβ2M amyloidosis 7

2.3.4 AA amyloidosis 7

2.4 Serum Amyloid A protein 9

2.5 Role of Glycosaminoglycan in SAA aggregation 11

2.6 Nuclear Magnetic Resonance (NMR) 16

2.6.1 Magic Angle Spinning (MAS) 18

2.6.2 Cross-Polarization (CP) 19

2.6.3 Assignments by solid-state NMR 21

2.6.4 Prediction of Long-range interactions 22

2.6.5 Characterizing Dynamic part of Amyloids 25

2.7 Scope of the Study 26

3. Materials and Methods 28

3.1 Materials 28

3.1.1 Chemicals 28

3.1.2 Equipment 28

3.1.3 Enzymes, Standards and Kit 30

3.1.4 Bacterial Strain 30

3.1.5 Buffer and solutions for Bacterial growth 30
3.1.6 Software 31
3.1.7 Database 31
3.2 Methods 32
3.2.1 Transformation of E. coli 32
3.2.2 Isolation of plasmid DNA from E. coli 32
3.2.3 Protein Expression and Purification of SAA 1.1 32
3.2.4 Protein Characterization 34
4. Result 40
4.1 Characterization of mSAA and investigation of SAA fibril structure using solid state NMR 40
4.1.1 The biophysical analysis of mSAA 1.1: 40
4.1.2 SAA structural transformation characterization by CD and Fluorescence spectroscopy 44
4.1.3 Kinetic study of fibril formation 45
4.1.4 Characterizing the morphology of SAA fibril 46
4.1.5 Solid-state NMR assignment of SAA fibrils 47
4.1.6 Comparative analysis of ssNMR and cryo-EM structure 53
4.1.7 TEDOR for SAA fibrils 59
4.1.8 Comparison of non-seeded in vitro fibrils with the seeded in vitro fibrils 60
4.1.9 Conclusion and Discussion 62
4.2 Effect of heparin on the aggregation mechanism of SAA and on the structure of SAA fibrils 64
4.2.1 Effect of Heparin on the kinetics of fibril formation 64
4.2.2 Effect of Heparin on the structure of SAA fibrils 66
4.2.3 Heparin stabilizes the SAA fibrils 68
4.2.4 SAA fibrils are more apolar in presence of heparin 72
4.2.5 Heparin reduces the heterogeneity of non-seeded SAA fibrils 72
4.2.6 Effect of heparin on the non-structured region flanking from SAA fibrils 76
4.2.7 Binding of Heparin with SAA fibrils 77

4.2.8 Mechanism involved in SAA fibrillation in presence of heparin 80
4.2.9 Conclusion and Discussion 83
4.3 Interaction of SAA with Lipids 88
4.3.1 SAA aggregation in presence of lipids 88
4.3.2 Binding of SAA with Nanodiscs 89
4.3.3 Effect of lipids on the stability of SAA 90
4.3.4 The influence of lipids on the structure of SAA 93
4.3.5 The structural study of SAA with nanodiscs 95
4.3.6 Conclusion and Discussion 99
5. References 101
Appendix I 114
Appendix II 116

Acknowledgments

An immense thank you to my Ph.D. supervisor *Prof. Bernd Reif*, for providing me the opportunity to work on this exciting project. The regular meetings, discussions, and feedback kept me enthusiastic and persevered despite having hurdles on the way. Your easy-to-approach attitude and readiness to discuss the problems motivated me to look at the situation with different approaches and keep trying new solutions. Furthermore, your critical opinions encouraged me to find solutions for the ongoing issues.

I am very grateful to the thesis committee members, *Prof. Dr. Franz Hagn* and *Dr. Gerd Gemmecker* for their participation as an examiner and chair, respectively.

I would like to thank *Prof. Marcus Fändrich*, *Dr. Christian Haupt*, and *Dr. Matthias Schmidt* for the good collaboration and providing the vector for my studies. A special thank you to *Dr. Carsten Peters*, for your assistance with Electron Microscope.

I sincerely thank my graduate school GRK1721 and funding agency SFB1035, for providing various opportunities to meet great professors, alumni, and trainers who paved a path for my overall growth and development.

Thank you, *Dr. Riddhiman Sarkar*, for all your support with the solid-state NMR experiments and discussion on NMR analysis. Your enthusiasm for analyzing the NMR experiments and trying new experiments was contagious and motivated me to repeat my attempts. Thank you, *Dr. Sam Asami*, for all the optimized NMR pulses in solution NMR.

Thank you, *Benita Koch*, for keeping the lab organized and providing support for the lab experiments whenever needed. *Dr. Saba Suladze*, thank you for all the scientific and non-scientific discussions, which led me to try different experiments. Your suggestions for colors in figures and presentations were always helpful. Thank you, *Dr. Tejaswini Pradhan*, for all the first introductions, from putting rotors in the ssNMR to the graduate school meetings. Thank you, *Dr. Matthias Brandl*, for solving all my computer problems and all the good discussions on NMR and conferences. Thank you, *Markus Fleisch*, for keeping the fun and warmth in the office and introducing me to different instruments like CD and DLS. Thank you, *Natalia Rodina*, for all the EM experiments and all the good discussions. Discussing all the ThT assays and EM images was always fun and beneficial. I will never forget your great cakes and food *Olga Sieluzycka*. It was helpful that I could always get NMR time from you.

Thank you, *Asita Djamschidi*, for your assistance with the paperwork and all the life advices. *Dr. Zheng Niu*, *Dr. Manuel Hora*, *Dr. Kai Xue*, *Dr. Diana Rodriguez*, *Dr. Maria Stavropoulou*, and *Dr. Carina Motz*, although you are not currently part of the group, however, it was great to learn from you and get your advice. I would like to thank you for all your support, suggestions, and feedback you have provided me during the initial period of my Ph.D. All of those learnings stayed with me in my journey.

I sincerely thank all the colleagues from BNMRZ for cultivating a great scientific environment where one can comfortably discuss scientific topics. The friendly and open surroundings are advantageous to get introductions on equipment, new possible experiments, and analysis methods.

I am thankful to my parents, sister, and family for encouraging me to follow my dreams and motivating me to keep going, irrespective of the difficult time. I am incredibly grateful to my husband, *Abhijeet Nath*, who provided me a comfortable environment to do multiple things simultaneously. Your hard work is contagious and pushed me to stay focused.

Abbreviations

Abbreviations	Full name
AA amyloidosis	Amyloid A amyloidosis
ACN	Acetonitrile
Aβ	Amyloid-β peptide
BMRB	Biological Magnetic Resonance Data Bank
CD Spectroscopy	Circular Dichroism Spectroscopy
CP	cross polarisation
CSA	Chemical shift anisotropy
CSI	Chemical shifts index
DARR	Dipolar assisted rotational recoupling
DLS	Dynamic Light Scattering
DNA	Deoxyribonucleic acid
DSS	Sodium trimethylsilylpropanesulfonate
E. coli	*Escherichia coli*
ECG	Electrocardiogram
ECM	Extracellular Matrix
EM	Electron Microscope
FDA	Food and Drug Administration
FID	Free induction decay
GAG	Glycosaminoglycan
HDL	High Density Lipid
HPLC	High performance liquid chromatography
HSQC	Heteronuclear single quantum coherence experiment
IDP	Intrinsically disordered proteins
INEPT	Insensitive nuclei enhancement by polarization transfer
IPTG	Isopropyl β-D-1-Thiogalactopyranoside
LB	Luria broth
MAS	magic angle spinning
MD	Molecular Dynamics
ND	nanodisc
NMR	Nuclear Magnetic Resonance
NUS	Non-uniform sampling
OD_{600}	Optical density at 600nm
PAR	Proton assisted recoupling
PDB	protein data bank

PDSD	proton-driven spin diffusion
REDOR	rotational echo double resonance
RMSF	root mean square fluctuation
RNA	Ribonucleic acid
RPC	reverse phase chromatography
S/N ratio	signal-to-noise ratio
SAA	Serum amyloid A
SAP	Serum Amyloid P protein
SDS-PAGE	Sodium dodecyl sulfate-polyacrylamide gel electrophoresis
SEC	size exclusion chromatography
ssNMR	solid-state Nuclear Magnetic Resonance
SUV	small unilamellar liposomes/vesicles
TEDOR	Transferred echo double resonance
TEM	Transmission Electron Microscope
TEV	Tobacco Etch Virus
TFA	trifluoroacetic acid
ThT	Thioflavin T
Tm	melting temperature
TNF	Tumor necrosis factor

1. Summary

1.1 Summary

AA amyloidosis is a type of systemic amyloidosis caused by the aggregation of the acute phase protein Serum Amyloid A (SAA). It is one of the most abundant systemic amyloidoses affecting humans as well as a large range of other species. It is known for its prion-like characteristics causing transmission of amyloidosis across species. Amyloidosis is triggered by injection of purified fibrils and oligomers or by oral uptake. The disease arises from misfolded SAA protein and is initiated by upregulation of SAA as a consequence of infection, inflammation, or injury. Aggregates deposit in many organs like liver, spleen, etc. Involvement of the kidneys leads to health burdens and may require an organ transplant or can be even lethal.

In this thesis, I investigated the stability of SAA and its propensity to aggregate as a function of the solution conditions (buffer and temperature) using ThT aggregation assays, CD spectroscopy, and solution-state NMR spectroscopy. The structure of seeded fibrils using solid-state NMR spectroscopy was analyzed. For this purpose, chemical shift assignments for SAA fibrils that were prepared using *in vitro* generated seeds were obtained that yield the topology of the secondary structure elements. Additionally, the polymorphic properties were studied by comparing seeded and non-seeded SAA fibrils. Scalar coupling based experiments allowed to identify the regions of the protein within the fibril structure which are highly dynamic. We finally compared the topology obtained by solid-state NMR with the structure deduced from cryo-EM. The aim of this part of the thesis was to identify structural differences for the two methods, given that the cryo-EM structure is obtained by reconstitution of individual particles that are resolved on the EM grid and the fact that the signal obtained by solid-state NMR is obtained from the bulk without having the possibility to filter for certain polymorphs.

Extracted SAA fibrils contain lipids, glycosaminoglycan (GAGs), and serum amyloid protein (SAP) that co-aggregate with SAA. GAGs are not only found in AA deposits but are as well characteristic in other amyloidoses, such as AL amyloidosis. So far, it has not been explored how these cellular components affect amyloid fibril structure. It is only known that GAGs influence aggregation kinetics. Using MAS solid-state NMR, I have explored the effects of heparin on the structure and polymorphism of SAA fibrils. In addition, TEM, CD, fluorescence spectroscopy, and ThT assays was employed to better understand the effects of heparin on the mechanism of protein aggregation.

Since SAA is a member of the apolipoprotein family, I studied the behavior of SAA in the presence of lipids as well. The native SAA protein is unstable at room temperature. Two models, liposomes and nanodiscs, were used to investigate the stability of SAA in a lipid context. It has been previously found that SAA is stable in the presence of lipids. Using CD spectroscopy, first liposomes with different diameters were utilized to characterize the stability of SAA at different temperatures. Additionally, the aggregation propensity was investigated in the presence and absence of liposomes using a ThT assay. Furthermore, nanodiscs were incubated with SAA and the stability of SAA using CD, fluorescence, and NMR spectroscopy was explored. In addition, the SAA-nanodiscs complex were imaged using TEM. Finally, the SAA fibril formation kinetics was determined in the presence of nanodiscs using a ThT assay. For both models, it was found that SAA does not aggregate in the presence of lipids and stabilizes by clustering together in small amorphous aggregates.

In summary, this work provides insights into the structure of *in vitro* prepared SAA fibrils in bulk and the possible polymorphs that can be adopted by SAA. I also investigated the role of cellular components such as lipids and heparin to better understand structural differences between *in vivo* and *in vitro* formed fibrils. The current study provides a basis of how cellular components can affect the mechanism and stability of SAA fibrils. This knowledge will be helpful in the future in designing therapeutics for *in vivo* fibrils and will allow to explain why only a few polymorphs are formed under physiological conditions.

Keywords: AA amyloidosis, SAA, NMR, structure of fibrils, polymorphs

1.2 Zusammenfassung

Die AA-Amyloidose ist eine Form der systemischen Amyloidose, die durch die Aggregation des Akute-Phase-Proteins Serum-Amyloid A (SAA) verursacht wird. Sie ist eine der häufigsten systemischen Amyloidosen, die sowohl den Menschen als auch eine Vielfalt anderer Spezies betrifft. Sie ist bekannt für ihre Prionen-ähnlichen Eigenschaften, und bringt eine Transmission der Amyloidose auf andere Spezies mit sich. Die Amyloidose wird durch Injektion von gereinigten Fibrillen und Oligomeren oder durch orale Aufnahme zwischen verschiedenen Spezies ausgelöst. Die Krankheit resultiert aus falsch gefaltetem SAA-Protein und wird durch eine Hochregulierung von SAA ausgelöst, die eine Folge von Infektionen, Entzündungen oder Verletzungen ist. Die Aggregate lagern sich in vielen Organen wie Leber, Milz usw. ab. Die Beteiligung der Nieren führt zu gesundheitlichen Belastungen und kann eine Organtransplantation erforderlich machen oder sogar tödlich sein.

In dieser Doktorarbeit untersuchte ich die Stabilität von SAA und seine Neigung zur Aggregation in Abhängigkeit von den Lösungsbedingungen (Puffer und Temperatur) mithilfe von ThT-Aggregationstests, CD-Spektroskopie und NMR-Spektroskopie im Lösungszustand. Die Struktur der ge-*seedeten* Fibrillen wurde mit Hilfe der Festkörper-NMR-Spektroskopie analysiert. Zu diesem Zweck wurden chemische Verschiebungszuordnungen für SAA-Fibrillen, die mit in vitro erzeugten *Seeds* hergestellt wurden, ermittelt, die die Topologie der Sekundärstrukturelemente ergeben. Zusätzlich wurden die polymorphen Eigenschaften durch den Vergleich von ge-*seedeten* und nicht ge-*seedeten* SAA-Fibrillen untersucht. Mit Hilfe von Experimenten, die auf skalarer Kopplung beruhen, war es möglich, die hochdynamischen Bereiche des Proteins innerhalb der Fibrillenstruktur zu identifizieren. Schließlich verglichen wir die Topologie, die wir durch Festkörper-NMR erhalten hatten, mit den Strukturen, die durch Kryo-EM ermittelt wurden. Das Ziel dieses Teiles der Doktorarbeit war es, strukturelle Unterschiede zwischen den beiden Methoden zu identifizieren, da die Kryo-EM-Struktur durch die Rekonstitution einzelner Partikel erhalten wird, die auf dem EM-Gitter aufgelöst werden, und das durch Festkörper-NMR erhaltene Signal aus der Gesamtprobe erhalten wird, ohne die Möglichkeit zu haben, nach bestimmten Polymorphen zu filtern.

Extrahierte SAA-Fibrillen enthalten Lipide, Glykosaminoglykane (GAGs) und Serum-Amyloid-Protein (SAP), die mit SAA koaggregieren. GAGs finden sich nicht nur in AA-Ablagerungen, sondern sind auch charakteristisch für andere Amyloidosen wie die AL-Amyloidose. Bislang wurde nicht untersucht, wie diese zellulären Komponenten die Struktur der Amyloidfibrillen betreffen. Es ist nur bekannt, dass GAGs die Aggregationskinetik

beeinflussen. Mit MAS Festkörper-NMR habe ich die Auswirkungen von Heparin auf die Struktur und den Polymorphismus von SAA-Fibrillen erforscht. Zusätzlich wurden TEM, CD, Fluoreszenzspektroskopie und ThT-Assays eingesetzt, um die Auswirkungen von Heparin auf den Mechanismus der Proteinaggregation besser zu verstehen.

Da SAA zur Familie der Apolipoproteine gehört, habe ich auch das Verhalten von SAA in Gegenwart von Lipiden untersucht. Das native SAA-Protein ist bei Raumtemperatur instabil. Zwei Modelle, Liposomen und Nanodiscs, wurden verwendet, um die Stabilität von SAA in einem Lipidkontext zu analysieren. Es wurde bereits festgestellt, dass SAA in Gegenwart von Lipiden stabil ist. Mittels CD-Spektroskopie wurden zunächst Liposomen mit unterschiedlichen Durchmessern verwendet, um die Stabilität von SAA bei verschiedenen Temperaturen zu charakterisieren. Außerdem wurde die Aggregationsneigung in Anwesenheit und Abwesenheit von Liposomen mit Hilfe eines ThT-Tests untersucht. Darüber hinaus wurden Nanodiscs mit SAA inkubiert und die Stabilität von SAA mittels CD-, Fluoreszenz- und NMR-Spektroskopie untersucht. Des Weiteren wurde der SAA-Nanodiscs-Komplex mittels TEM abgebildet. Schließlich wurde die Kinetik der SAA-Fibrillenbildung in Gegenwart von Nanodiscs mit Hilfe eines ThT-Tests bestimmt. Für beide Modelle wurde festgestellt, dass SAA in Gegenwart von Lipiden nicht aggregiert und sich durch Zusammenballung in kleinen amorphen Aggregaten stabilisiert.

Insgesamt liefert diese Arbeit Erkenntnisse über die Struktur von in vitro hergestellten SAA-Fibrillen sowie möglicher anderer SAA Polymorphe. Ich habe weiterhin die Rolle von zellulären Komponenten wie Lipiden und Heparin untersucht, um die strukturellen Unterschiede zwischen in vivo und in vitro gebildeten Fibrillen besser zu verstehen. Diese Studie zeigt wie zelluläre Komponenten den Mechanismus Fibrillenbildung und die Stabilität von SAA-Fibrillen beeinflussen können. Dieses Wissen wird in Zukunft bei der Entwicklung von Therapeutika für in vivo gebildete Fibrillen hilfreich sein und kann erklären, warum unter physiologischen Bedingungen nur wenige Polymorphe gebildet werden.

Stichwörter: AA-Amyloidose, SAA, NMR, Struktur der Fibrillen, Polymorphien

2. Introduction

2.1 Proteins

Proteins are the polymers of amino acids [1]. Central dogma states that the DNA contains the information transformed into RNA and further translated to proteins. These are the complex macromolecules responsible for many critical functions in an organism. The proteins are the functional unit responsible for structure, regulation, and signaling in cells or tissues. 20 different types of amino acids serve as building blocks for proteins. A protein's primary structure is constituted of linear sequence of amino acids. However, tertiary and quaternary structure decides the function of a protein. The protein attains a specific three-dimensional structure with the process of folding, and this structure is responsible for the protein's biological function.

As postulated by Noble prize Laureate Christian B. Anfinsen [2], the unique sequence of amino acids defines the three-dimensional structure of a protein constituting it. He gave the Anfinsen dogma, which states that the interaction in the amino acid sequence leads to a stable structure and at the unchallenged global minima of free energy. There is no possibility of any other conformation to attain free energy less than the native structure of the protein. However, the Anfinsen dogma does not consider misfolding of protein, the protein fold switch, folding by chaperones, and amyloid formation.

The structure depends on the hydrophobic interactions of polar amino acids, van der Waals forces, and salt bridges formed by the interaction of ionic residues, hydrophilic, and hydration energy [3-6]. The native structure of a protein is at the minima of free energy and kinetically stable [7]. However, it does not stand true for the proteins with domain switch, intrinsically disordered proteins, large complexes of protein, and functional amyloids. The protein's three-dimensional structure with domain switch attains a local minimum in the free energy landscape and switches to another conformation depending on the environment [8-10].

The protein folding starts during the process of translation. The N-terminal begins to fold while the ribosomes translate the C-terminal [11]. However, in some scenarios, protein is not able to fold itself. Then the chaperones come into the action and fold the protein to its native structure. They also play a critical role in forming large protein complexes and folding the misfolded proteins [12-14]. The native structure of a protein is essential for its function, but for some proteins the native structure comprises of dynamic regions. These dynamic parts of

the protein are also critical for the protein's functionality. In some scenarios, the folding machinery fails leading to the formation of misfolded proteins. These misfolded proteins

1 A.

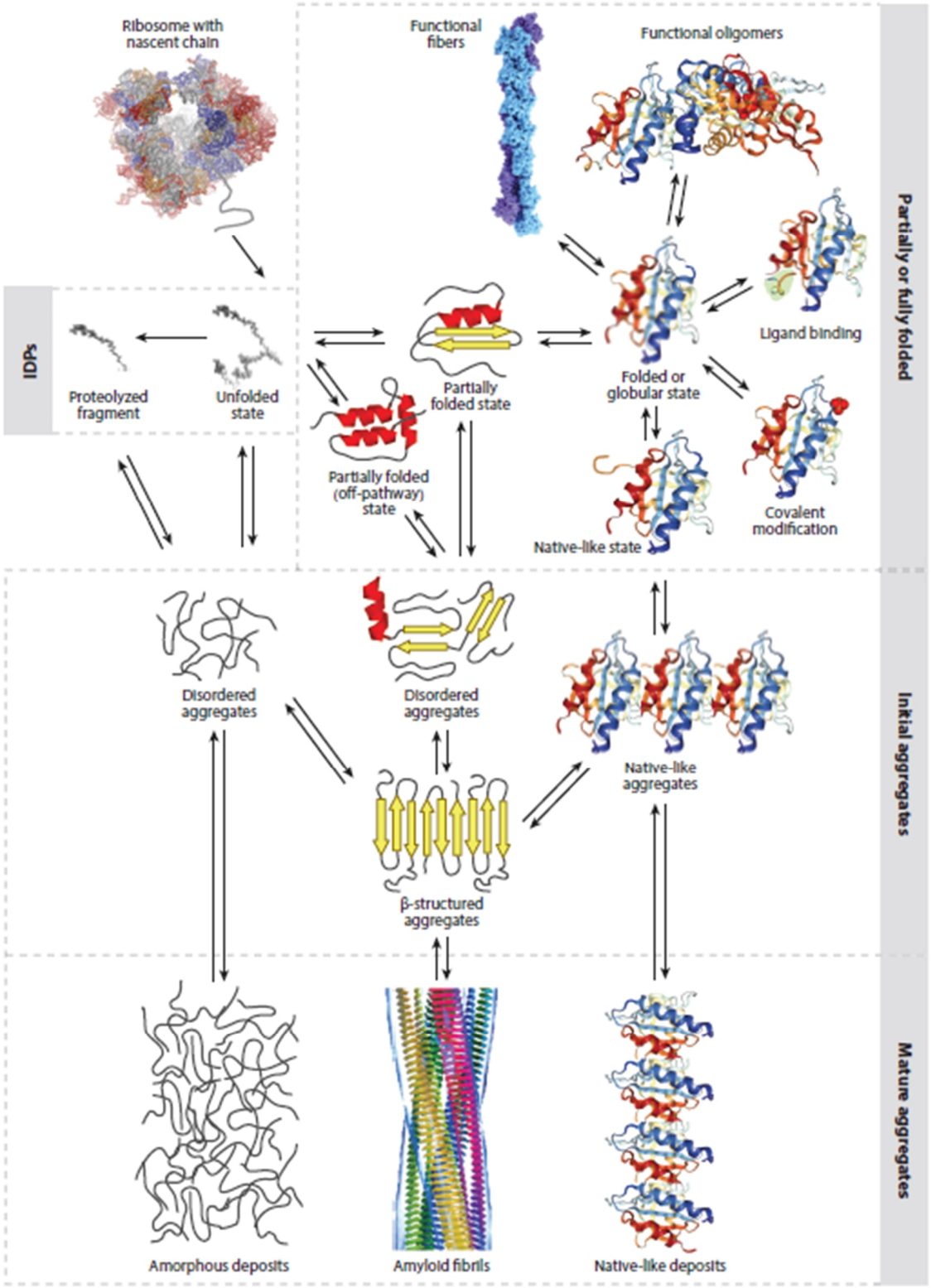

Figure 1. Folded, aggregates or amorphous states of protein. *A, Schematic representation of possible states of protein structure after protein synthesis [15].*

cannot attain their native structure and are mostly inactive. Certain misfolded proteins also become toxic and can cause allergies, as in the case of antibodies or form amyloids, as in neurodegenerative diseases and systemic amyloidosis. Figure 1 depicts the different possible states attain by a polypeptide chain after translation.

The misfolding of protein leads to exposure of hydrophobic residues. These residues interact with residues from another misfolded protein which further forms amyloid - these aggregates deposit in the organs, compromising the normal function of organs and tissues [16]. The amyloids are characterized as long fibrils with secondary structures rich in β-sheet, which run perpendicular to the axis of the fibrils [17-19].

The misfolding of a protein can be caused by various reasons which direct the protein toward amyloid formation. Amyloidosis can occur because of genetic mutation as observed for Hereditary amyloidosis where amyloidosis occurs at an early age caused by a mutation in gene, that translates a protein which cannot fold to its native state. This misfolded protein will aggregate to make fibrils. These mutations are primarily autosomal dominant; therefore, amyloidosis will develop even if only one gene is mutated. Generally, amyloids are identified in old age. Amyloidosis, in these instances, is a consequence of failure in regulation or cellular machinery because of aging, which leads to amyloid formation. The amyloids can also form by the infection of another misfolded protein. Prions are the aggregated proteins that can generate a kinetic reaction to unfold a folded protein and push it toward amyloid formation. It has been observed in diseases like Kuru, where eating the brains of infected animals caused amyloid formation in healthy beings [15, 20-22].

These amyloids are involved in many diseases related to neurodegeneration, cardiomyopathy, or renal issues. A single sequence of amino acids can also lead to different amyloid conformations. This phenomenon is known as polymorphism. The amyloid polymorphs have different morphologies but similar molecular or atomic structures [23-25]. Protease digestion can cause amyloid formation for some proteins, as in AA amyloidosis. However, amyloids are resistant to proteolysis and degradation [26, 27].

In addition to misfolded proteins, intrinsically disordered proteins (IDP) can also lead to amyloid formation. An IDP does not have any specific tertiary structure but a secondary structure. The IDP adopts a specific structure only under cellular signaling or regulation. The IDPs form functional amyloids when they fold to a stable structure on cellular signaling or environmental condition. At the same time, it can create amyloids that are pathogenic when undergoing proteolysis or an unstable structure that can form aggregates [28-31].

2.2 Diseases related to amyloidosis

The process of aggregation of protein in an insoluble form is termed amyloidosis. These insoluble aggregates deposit in various organs and lead to tissue damage or organ dysfunction. Amyloidosis can be localized, like Alzheimer's, which only affects the central nervous system, or systemic, like AL amyloidosis affecting various organs.

Over the past decades, many proteins have been identified as forming amyloids and causing amyloidosis. Among these, some are involved in the amyloidosis caused by aging, which affects the brain and other organs like the heart, pancreas, tendons, and ligaments. For example, proteins like Aβ, α-synuclein, Tau, Islet amyloid peptide, Transthyretin, and Atrial natriuretic factor are involved in the amyloid formation with the aging and affect brain, pancreas, lung, and heart, respectively, as shown in figure 2 [32-39].

2 A.

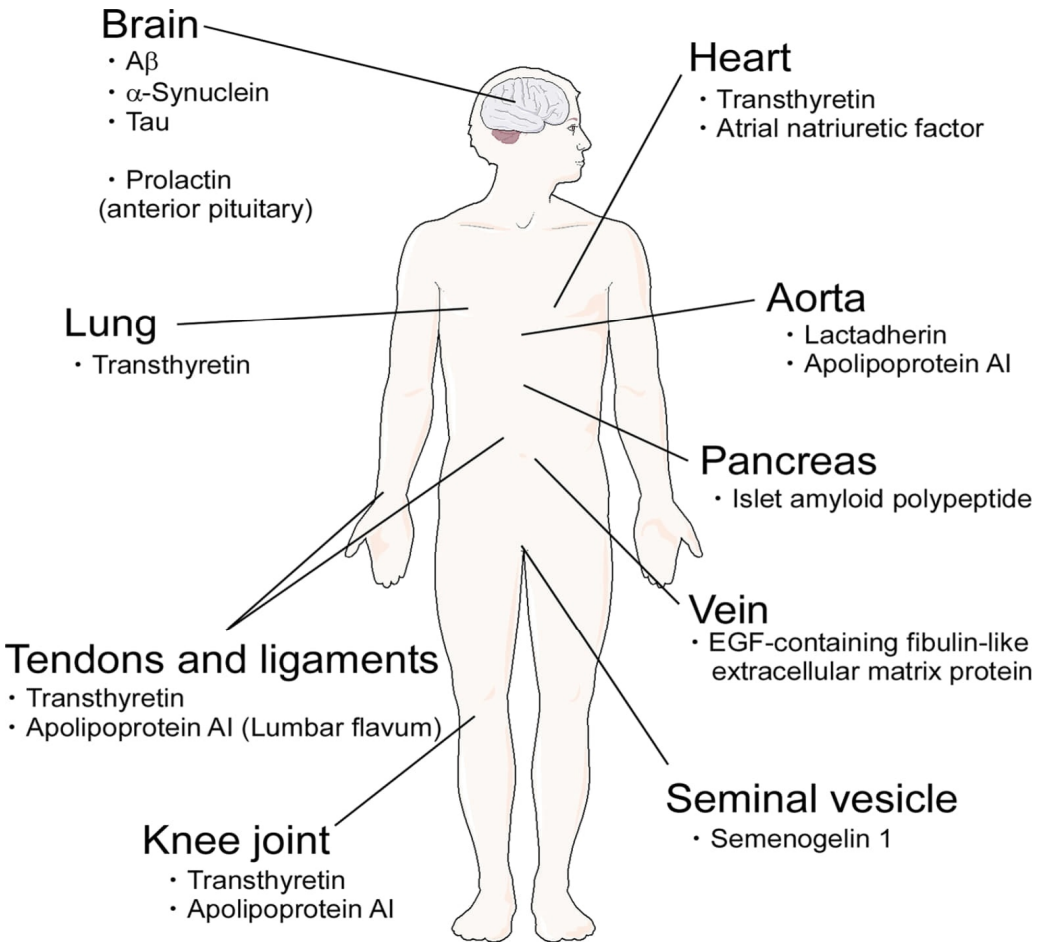

Figure 2. Organs affected by amyloidosis. A**.** *Representation of organs affected by different amyloidogenic proteins in old age [21].*

In addition to aging, amyloidosis can be triggered by various causes. The aggregation of apolipoproteins can be caused by genetic mutation. The failure of tau to bind with microtubules enhances aggregation in Aβ 40 and 42 leading to fibril formation which cause cerebral haemorrhage. Amyloidosis can be triggered by medical conditions like dialysis in case of kidney diseases which cause aggregation of beta-2-microglobulin [40] or by prion infecting other proteins after an organ transplant [41]. Disease like AA amyloidosis occurs by the increase in the concentration of protein after acute infection, chronic disease, or rheumatoid arthritis [42-44].

The pathogenesis of amyloids is caused by the protein aggregates and the toxic oligomers or protofilaments formed in the process. The extent of pathogenicity depends on the amount of fibrils deposited [45, 46]. The atomic details of fibrils are well characterized by cryo-EM and solid-state NMR (ssNMR), which give insight into the stability and polymorphism of amyloid fibrils. Nevertheless, the structural details are insufficient to identify the therapeutic aids for amyloidosis [47, 48]. Therefore, there is a need to identify methods to stop the pathogenic protein's overproduction, not allowing the protein to participate in fibril formation, and ways to eliminate the pre-formed fibrils. Consequently, in addition to the structure of amyloids, it is essential to study the triggers for amyloidosis, pathways involved in the amyloid formation, and the role of co-aggregates in the process of aggregation, pathogenesis by oligomers, and stability of the fibrils.

2.3 Systemic amyloidosis

Amyloidosis results in abnormal deposition of plasma protein in the extracellular matrix. It can be localized, i.e., the protein aggregates where it is synthesized, or systemic when a protein is synthesized in one organ and aggregates deposit in different organs. The organs mainly affected by systemic amyloidosis are heart, kidneys, liver, ligaments, and soft tissues. Around 17 proteins are responsible for causing systemic amyloidosis. The four most common systemic amyloidosis are AA amyloidosis, AL amyloidosis, ATTR amyloidosis, and Aβ2 microglobulin, which are described in the following subsections [49]. Table 1 illustrates the classification of different precursor proteins for amyloid formation.

Classification of Amyloids		
Type	**Precursor Protein**	**Syndrome**
AA	Serum Amyloid A protein	Systematic amyloidosis associated with chronic infection and inflammation
AL	Immunoglobulin light chains	Systemic amyloidosis associated with abnormal plasma cells
$A\beta_2M$	β_2-microglobulin	Systemic amyloidosis caused by prolonged

		dialysis
ATTR	Plasma transthyretin	Systemic amyloidosis causing cardiomyopathy
	Genetically variant transthyretin	Autosomal dominant systemic amyloidosis
Aβ	β-precursor protein	Prominently affects central nervous system. Rare genetic variants
IAPP	Islet amyloid polypeptide	Associated with β-cell death
ApoAI	Apolipoprotein A I protein	Autosomal dominant systemic amyloidosis mainly causing nephropathy
ApoAII	Apolipoprotein A II protein	Autosomal dominant systemic amyloidosis causing renal amyloidosis

Table 1. *Classification of amyloids, depicting the protein and the amyloidosis caused by it with the clinical syndrome [50].*

2.3.1 AL amyloidosis

AL amyloidosis, also known as primary amyloidosis, is the most commonly found systemic amyloidosis [51]. It is caused by the abnormal generation of the immunoglobulin light chain, either kappa or lambda, by an abnormal clone of plasma cells [52]. Incidents with the whole chain and only variable chains have been reported in the AL amyloid deposits. The amyloid deposits affect heart the most, but several other clinical manifestations, like kidney failure, neuropathy, and pulmonary issues, have also been observed [49]. Currently, suppression of B cells clone is the most utilized method to prevent the generation of immunoglobulin light chains and, thus, amyloid formation [53]. Additionally, chemotherapy for suppressing causative abnormal plasma cell, stem cell transplantation therapy, and combining chemotherapy with specific drugs like thalidomide are other treatment methods in use [54, 55].

2.3.2 ATTR amyloidosis

Main precursor protein of ATTR amyloidosis, Transthyretin (TTR), is produced in the liver and plays a vital role in the transport of thyroid hormone and retinol [56, 57]. Amyloidosis in TTR can happen by a genetic mutation in TTR genes [58-60]. These mutations can be inherited; therefore, ATTR amyloidosis can be genetic. While in some cases, with age, TTR becomes unstable and forms fibrils. TTR is a tetramer with four identical subunits, and in the case of amyloidosis, it becomes unstable, breaks, aggregates, and deposits in different organs [61, 62]. TTR amyloids can affect the heart, spinal canal, lungs, leg, and wrist and cause shortness of breath, chest pain, fatigue, numbness, or tingling sensation depending on the organs affected [63-66]. Magnetic Resonance Imaging (MRI), bone scan, blood test,

Electrocardiogram (ECG), and biopsy are commonly used to diagnose ATTR and locate it in the body. FDA approves various medication methods for the treatment of ATTR. Additionally, treatment methods like fibril disruption by green tea extract, silencing TTR protein by drugs, or medication to stabilize the TTR protein and not allowing it to make fibrils are investigated [67-69].

2.3.3 Aβ2M amyloidosis

Aβ2 microglobulin (Aβ2M) amyloidosis, also known as Dialysis related amyloidosis, is caused by the deposition of β2 microglobulin protein [70]. β2 microglobulin is a protein that constitutes the light chain of the MHC I complex [71]. It is highly expressed during infection, inflammation, or lymphoproliferative disorder [72, 73]. In normal circumstances, the excess protein is removed by the kidneys. However, in the situation of renal failure, the β2 microglobulin cannot be removed via haemodialysis. This causes the increase of local concentration of β2 microglobulin in the plasma and further leads to aggregation [74, 75]. Aβ2M is an excellent example of aggregation by proteolysis. It has been observed that the fibrils are heterogeneous, and it has fragments of β2 microglobulin [76, 77]. A six amino acid long fragment is removed from β2 microglobulin by proteolysis, leading to fibril formation [78]. It can also be hereditary due to variation at Asp76Asn, leading to amyloidosis even with normal renal function [79]. Clinical manifestations like carpal tunnel syndrome, pain in the shoulder, and cysts are observed in amyloidosis [80]. CT scan, MRI are useful for diagnosing the distribution and destructive lesions, and ultrasonography is a reliable method to detect aggregates in the shoulders [81].

2.3.4 AA amyloidosis

AA amyloidosis is the second most common type of amyloidosis. AA amyloidosis is mainly found in the acute phase response like chronic infection or inflammation [82]. For the same reason, it was one of the most prevalent types of amyloidosis during the eruption of tuberculosis [43, 83]. However, with the development of antibiotics, the cases of AA amyloidosis subsided. Serum amyloid A 1.1 is the main component of AA amyloidosis [84, 85]. Although it is a 104 amino acid long protein, the complete protein is never found in the extracted fibrils. The N-terminal of the protein forms the fibrils, while the C-terminal is cleaved by proteases [86]. However, whether the C-terminal is cleaved after the fibril formation or cleaving C-terminal is a trigger for aggregation is still unknown. Different lengths are deposited, which are specific to organs. For example, 76 amino acid long fragments are observed in renal glomeruli, while 100 amino acid long fragments are found in the renal medulla. Fibrils from the short fragment of 44 amino acids are recognized in blood vessels [87-89].

AA amyloidosis has shown prion-like characteristics and was transmissible in animals with high SAA plasma concentrations [90]. The transmissibility was observed in mink, cheetahs, mice, rodents, and ducks. In addition, it has been demonstrated that transmission depends on the seeding mechanism (figure 3) and can even cross species barriers [91-93].

AA amyloidosis mainly affects the kidneys and can even lead to renal insufficiency. In addition to the kidneys, the aggregates were also found in the pituitary, thyroid, and adrenals [94, 95]. Diagnosis methods used for detecting other amyloids are also utilized for AA amyloidosis. Staining the biopsies with congo red was the most common method used for detecting it [96]. The AA amyloidosis occurs because of the increase in the local concentration of SAA 1.1. Therefore, methods utilized to treat AA amyloidosis aim to reduce either the production of protein or stabilize it. Antisense oligonucleotides and monoclonal antibodies are used to suppress SAA production by the liver and cytokines, respectively [97, 98]. SAP and heparan sulfate are associated with extracted fibrils and are hypothesized to play a vital role in the aggregation of SAA, stability, and structure of SAA fibrils. However exact role and mechanism are still unknown. It was demonstrated that interference with small molecules or sulfonate in the binding of SAP or heparin to the SAA could inhibit amyloidosis [99-102].

3 A.

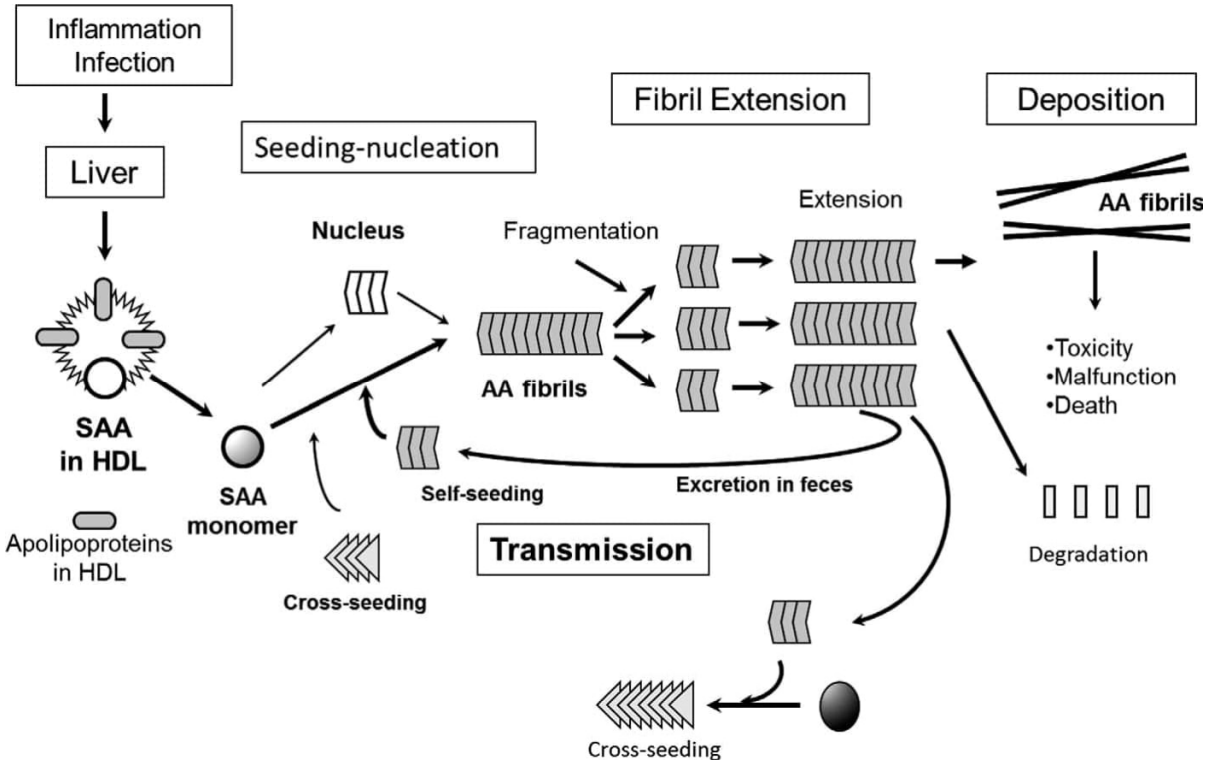

Figure 3 Mechanism of fibril formation. *A, Representation to depict the fibril formation by SAA and transmission possibility [91].*

Systemic amyloidosis significantly affects human body organs and hence many people's lives. Therefore, the development of precise diagnosis methods which can prevent misdiagnosis of the type of amyloidosis is very important. There are many common symptoms for different types of systemic diagnoses. Therefore, it is crucial to learn more about the proteins and triggers responsible for amyloidosis, structure and stability of the fibrils, and the unique characteristics of different types of amyloids.

2.4 Serum Amyloid A protein

Serum Amyloid A protein is an apolipoprotein for high density lipid (HDL) in the acute phase serum [103]. It is the major precursor for AA amyloidosis and was initially found as a serum component in AA (amyloid A) amyloidosis [104, 105]. Hepatocytes produce SAA under the action of cytokines like Tumor necrosis factor (TNF) and Interleukin-6 (IL-6). It plays a vital role in HDL remodeling, lipid metabolism, and cholesterol transport. It also mediates the removal of cholesterol from the sites of inflammation by binding to HDL.

In humans, SAA proteins are coded by 4 SAA genes that code for a family of 103-104 amino acids. SAA1 and SAA2 are responsible for coding the acute phase protein, SAA 4 codes for the constitutive phase protein, and SAA 3 is a pseudogene. In mice, SAA3 also codes for a functional protein [106-108]. SAA 1 is a polymorphic gene and codes for four proteins (SAA1.1, SAA1.2, SAA1.3, and SAA1.4) with a few amino acid variations. Among these SAA1.1 is the main component of AA amyloidosis [109]. Since the SAA family of proteins in mice is homologous to humans, the mice SAA proteins are ideal for functional and structural studies [110].

Being an acute-phase protein, the expression of SAA increases around 1000-fold during the infection or inflammation. The increased local concentration of SAA can lead to its aggregation. Additionally, it also acts as a biomarker for many chronic infections and inflammations [111]. The elevated expression of SAA 1 and SAA2 is utilized as a biomarker in many tumor prognoses. The expression of SAA 1 and SAA 4 are elevated in uterine cervical carcinoma, high level of SAA 1 is observed in lung cancer and nasopharyngeal carcinoma [112, 113].

SAA is also important for an organism's immunity and host defense system. It has a binding affinity with Omp-A, which is a constituent of extracellular membrane of Gram-negative bacteria [114]. The SAA binds to the bacteria leading to its opsonization [115]. In addition, it sends a signal to monocyte-derived macrophages, which drives the production of TNF-α and IL-10. It also binds to retinol and indirectly reduces the bacterial burden in the intestine [116].

The first structure of human SAA 1.1 was deduced by X-ray crystallography, as shown in figure 4. It is an α-helical protein with four helices in a conical bundle, and C-terminal stabilizes the protein by wrapping around the bundle with multiple contact points. In the native state, SAA adopts a hexameric structure with six identical subunits [117]. Previous studies additionally showed that SAA is octameric for a short period of time and then adopts a stable hexameric structure [118]. The structural mutational studies identified that HDL could bind to the apex, whereas heparan sulfate can bind to the apex and center of the hexamer. Hence, heparin competitively binds to SAA and can disrupt HDL from SAA leading to its aggregation. The helices 1 and 3 are prone to aggregation. However, the helices are concealed in the native hexameric structure and cannot lead to amyloidosis. Hence, the native structure of the SAA protein is non-pathogenic.

4 A. B.

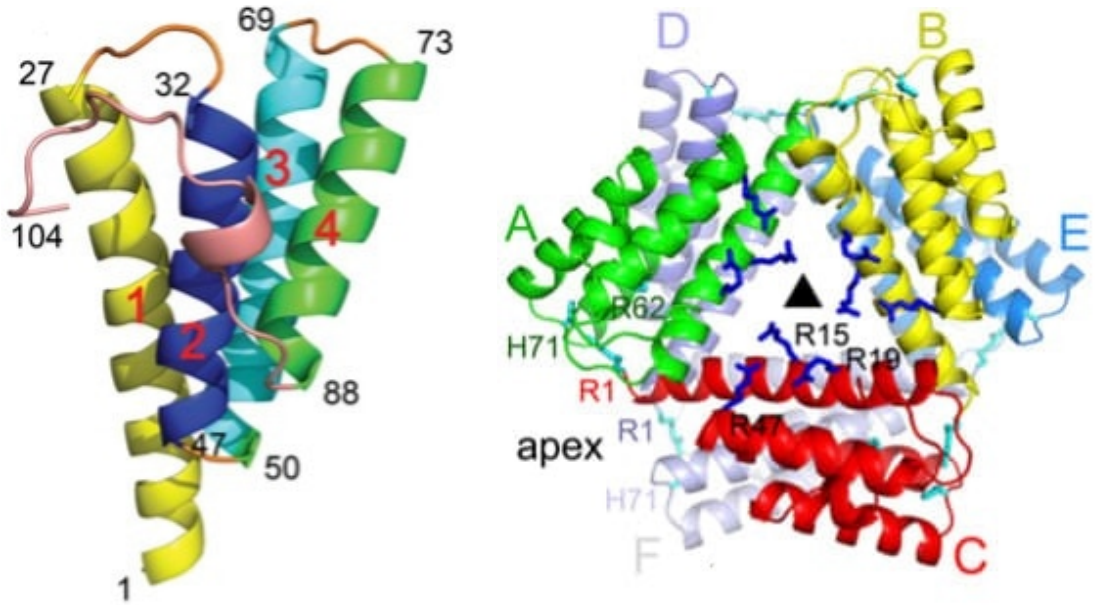

Figure 4 Structure of SAA *A. Structure of monomeric and B. Hexameric SAA deduced by X-ray crystallography [117].*

Previous studies have established that SAA in solution is unstructured at room temperature and has a very low melting point. However, lipids stabilize the protein and lead to the α-helical secondary structure of SAA [119]. It is amphipathic, which implicates the binding of SAA with lipids. It is verified that 95% of SAA remains bound to HDL in the blood, and only 5% of SAA is free in the cells' plasma. The binding of SAA with HDL is represented in figure 5. Unlike other amyloidogenic proteins, lipids inhibit the aggregation of SAA. *In vitro* studies of SAA have verified that SAA does not show any aggregation kinetics or very long lag phase in the presence of lipids. When incubated with SUVs, they form large nanoparticles that stabilize the SAA and do not allow fibril formation [120].

The fibrils formed by SAA are polymorphic, and the *in vitro* prepared fibrils are structurally different from the extracted fibrils [27]. The C–terminal of the protein was not observed in the cryo-EM structure of *in vivo* fibrils of humans and mice. Therefore, the importance of the role of cleaving the C-terminal still stands strong. The extracted fibrils from AA amyloidosis comprise GAGs, lipids, SAP, and the constituent protein. The co-aggregation of extracellular components with fibrils indicates their role in having structured and large core in the extracted fibrils compared to the *in vitro* fibrils. Therefore, exploring the dynamics of SAA fibrils and the role of extracellular components on the aggregation and structure of SAA is crucial.

5 A.

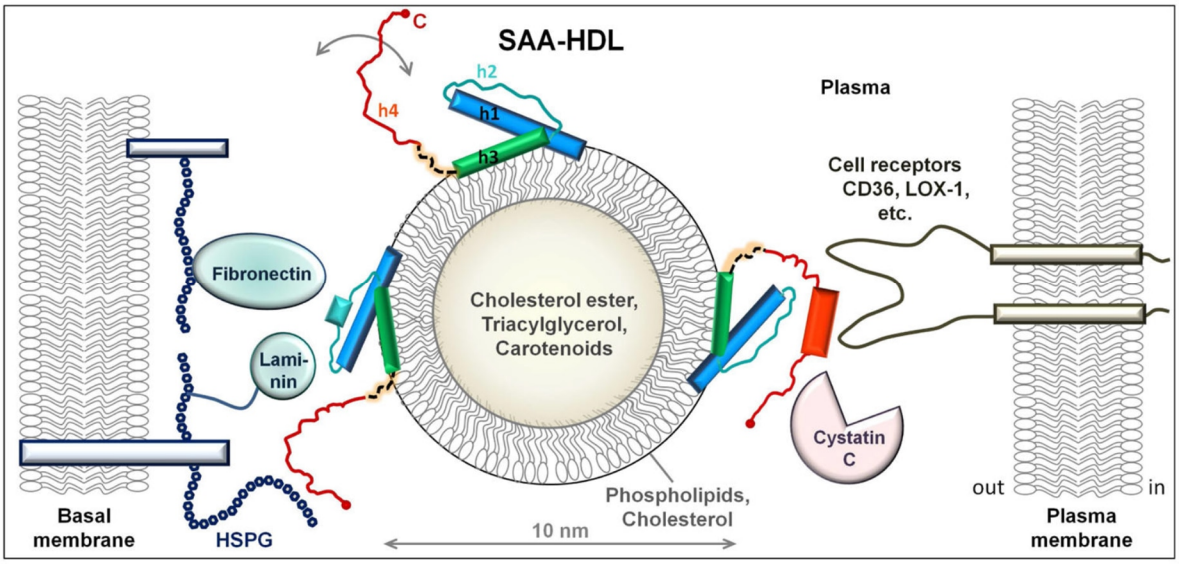

Figure 5. Binding of SAA with HDL *A. Model describing the binding of SAA with HDL particle [121].*

2.5 Role of Glycosaminoglycan in SAA aggregation

Glycosaminoglycans (GAGs) are long linear polymers that consist of repeating units of disaccharides of uronic acids and amino sugars. GAGs are highly polar and constitute an essential part of the extracellular matrix (ECM). It plays a vital role in cell signaling by interacting with proteins, providing flexibility to the cell membrane, acting as a shock absorber, and providing elasticity to the cell. GAGs are crucial in cell interaction, signal transduction, sensors, and transport. GAGs are also highly sulfated negatively charged entities with diverse lengths and structures because of their non-template synthesis. The GAG family is categorized in four main groups: Hyaluronic acid (HA), heparin and heparan sulfate, chondroitin and dermatan sulfate, and keratan sulfate.

Hyaluronic acid (HA) is the longest and the most unique among all the GAGs because of its anionic, non-sulfated nature. It resides in the plasma membrane and is widely distributed in connective, epithelial, and neural tissues. It can retain a high amount of water, is viscoelastic, and works as a lubricant in ECM. It plays a major role in cell migration and proliferation. It is also responsible for the migration of malignant tumors. The polymer chain comprises of repeating β-1,4-D-GlcA and β-1,3-N-GlcNAc units.

Keratan sulfate (KS) is a sulfated glycosamine with repeating galactose and N-acetyl glucosamine units. It is the only class of GAG that does not have uronic acid. KS is predominantly found in the cornea, cartilage, and bone. It is also produced in the central nervous system and engages in organism’s development. It has the propensity to water, which assists it in acting as a cushion against the mechanical shock to the joints. Both the KS's disaccharide units can be sulfated, but often only Glucosamine is sulfated.

Chondroitin sulfate is again a polymer of D-glucuronic and glucosamine. However, when the D-glucuronic acid is changed to L-iduronic acid by the process of epimerization, then it is known as dermatan sulfate. It is part of the ECM of endothelial cells, leukocytes, and platelets and provides a negative charge to the surface. It also plays a vital role in platelet activation. They are also crucial for cell processes like cell adhesion, migration, and signaling. In addition, it participates in neural growth and directs neuronal axons' development after an injury or accident. It is also used as a medicine to treat arthritis.

On the other hand, Heparin and Heparan sulfate are highly sulfated and acidic polymers. The structure of heparin chain is shown in figure 6A. They are composed of uronic acid and glucosamine repeating units, where uronic acid can be iduronic or glucuronic acid. As shown in figure 6B, glucosamine can be acetylated or sulfated. The heterogeneity in the heparin chain arises from its different chain lengths and variable sulfation. Heparin is usually higher sulfated than heparan sulfate and has a shorter polydisperse chain. Heparan sulfate is longer, with 50-200 disaccharide units where every unit has 1-2 sulfation. Iduronic acid is more common in heparin, while glucuronic acid is observed mainly in heparan sulfate. They are both synthesized in the endoplasmic reticulum and further transferred to the Golgi apparatus, modified with different enzymes. They play essential role in cell signaling and signal transduction via interaction with different proteins. Heparin is also crucial for the anticoagulation of blood.

It can be seen that GAGs are essential for cell development, signaling, migration, and proliferation. In addition, they are essential in binding with proteins, lubricating, absorbing mechanical shocks, and blood anticoagulation. However, in addition to all the vital functions, GAGS are also involved in pathological developments, especially in amyloidosis. It is evident

from many previous studies that GAGs promote the aggregation of proteins. For example, heparin and heparan sulfate promotes aggregation of a-beta and tau in Alzheimer's disease and tauopathies, respectively [122]. Adding heparin while fibril growth can lead to new morphologies of fibrils that are different from the structure of fibrils involved in pathology, as verified for tau fibrils [123].

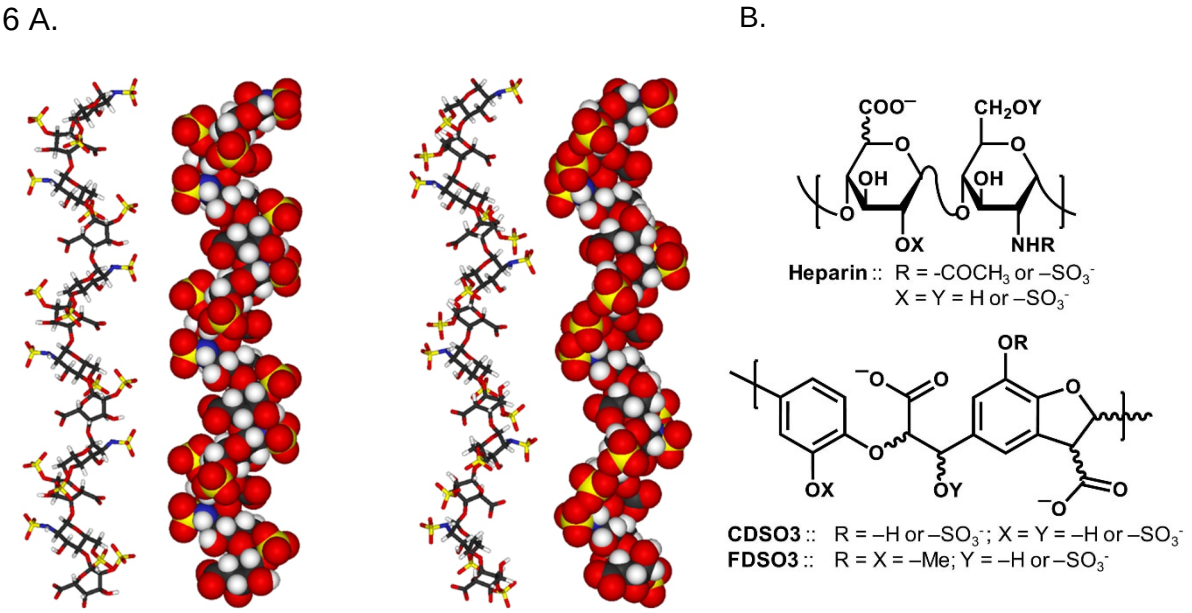

Figure 6 Structure of Heparin *A. Model representing the structure of heparin. B. The units constituting heparin and possible sulfation sites https://en.wikipedia.org/wiki/Heparin#References.*

GAGs are also co-aggregated with many extracted fibrils, such as Serum Amyloid A in AA amyloidosis and Light-chain Immunoglobulin in AL amyloidosis [124, 125]. Heparin and Heparan sulfate promote protein aggregation during the *in vitro* fibril formation [126]. Among GAGs, chondroitin sulfate inhibits the aggregation of SAA, while both heparin and heparan sulfate enhance aggregation [127]. The heparin and heparan sulfate reduce the lag phase to different folds depending on the chain length and degree of sulfation [128]. They also promote the oligomer formation for light-chain immunoglobulin in AL amyloidosis [129].

It has been demonstrated that in chronic infection or inflammation, like acute pancreatitis, the heparin-binding proteins are overexpressed, including SAA [130]. The heparin competitively binds to SAA and can dissociate HDL from SAA, marking the start of AA amyloidosis [131, 132]. The previous mutational study found that heparan sulfate and HDL have the same potential binding site on SAA [117]. Additionally, heparin prefers the N-terminal of SAA, while heparan sulfate binds to the C-terminal of the SAA as well [126]. The fragment study of SAA demonstrated that heparin influences mostly the aggregation of 1-27 residues of SAA and has a negligible effect on the aggregation of 43-63 and has no effect on residues from 77-104 [133]. It has been established that arginines and lysines in the SAA sequence play a vital role in the heparin-binding [134]

The previous researches illustrates that heparin binds to the basic residues of the proteins and promotes aggregation kinetics [135]. Heparin binding to a protein is not site, structure, or sequence-specific. Various hypotheses have been postulated to describe the effect of heparin on fibril formation. Heparin promotes aggregation of β2-microglobulin at lower concentrations and inhibits at higher concentrations, as depicted in figure 7. It has been postulated that heparin makes a matrix at a lower concentration where protein can bind, leading to an increase in the local concentration of protein, which results in fibril formation. On the other hand, charge repulsion occurs at higher concentrations of heparin, resulting in lower local protein concentration, which inhibits the aggregation [136]. The molecular modeling of heparin and proteins showed that basic residues followed by non-basic residues could lead to the binding of heparin. The heparin-binding domains mostly contain XBBBXXBX and XBBXBX consensus sequences [137]. It was postulated for Apomyoglobin that heparin identifies the basic residues in the turn of the native protein or all the basic residues in the unfolded protein and acts as an immobilized charged surface. The surface provides an orientation platform for the monomeric protein, which generates the seeds for the aggregation or induces the conformation transition of a protein to β-sheets. It has been found that reduction in lag phase by the addition of heparin, reduces the formation of toxic oligomers [138].

Furthermore, heparin demonstrates a complex behavior for the aggregation of Hen egg lysozymes. It enhances the aggregation at lower and higher concentrations while inhibiting it at intermediate concentrations (approx. 10 mg/ml). It was hypothesized that at a lower concentration, hetero-oligomer interaction occurs, which promotes aggregation, while increasing the concentration of heparin to 10 mg/ml can stabilize the native state of a protein. However, any more increment in the concentration of heparin leads to salting-out effect, which further causes aggregation, as shown in figure 8 [139].

The significant role of heparin and heparan sulfate in the aggregation of proteins exhibits them as a potential drug target. The component inhibiting physiological function of heparan sulfate in zebra fish can prevent tau pathologies [122]. Heparinise treatment in human islets can inhibit IAPP aggregation and protect against islet cell deaths [140]. In some instances, the length of heparin chains is also critical for amyloidosis. The overproduction of heparinise in transgenic mice leads to short heparan sulfate chains, which do not promote amyloid formation. As a consequence, the organs overproducing heparinise are protected from the aggregation of SAA [141]. Therefore, heparin and heparan sulfate are supposed to be therapeutic candidates for inhibiting amyloid formation. However, the mechanism of heparin binding, its impact on the stability of fibrils, and its mechanism of promoting aggregation are yet to be explored.

7 A.

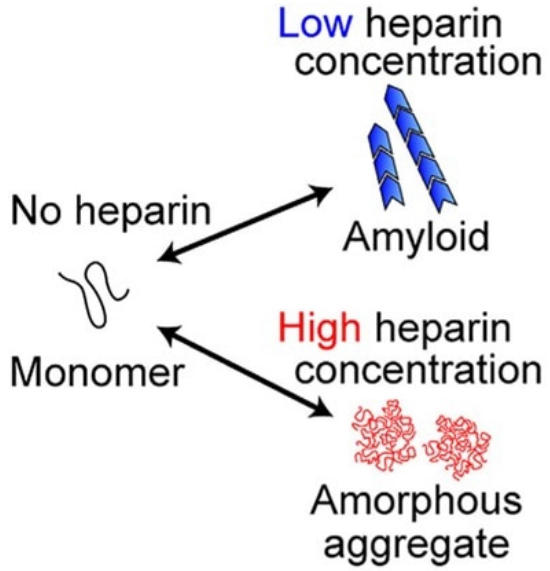

B.

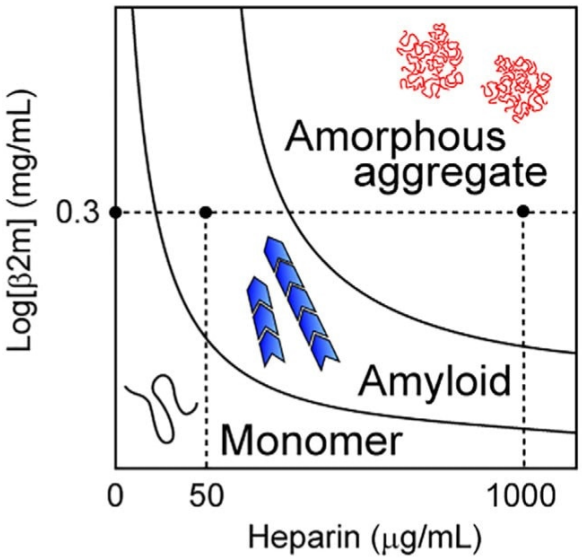

Figure 7. Impact of different concentration of heparin on β2-microglobulin aggregation *A. Model representing the effect of concentration of heparin on the aggregation of β-2 microglobulin [136].*

8 A.

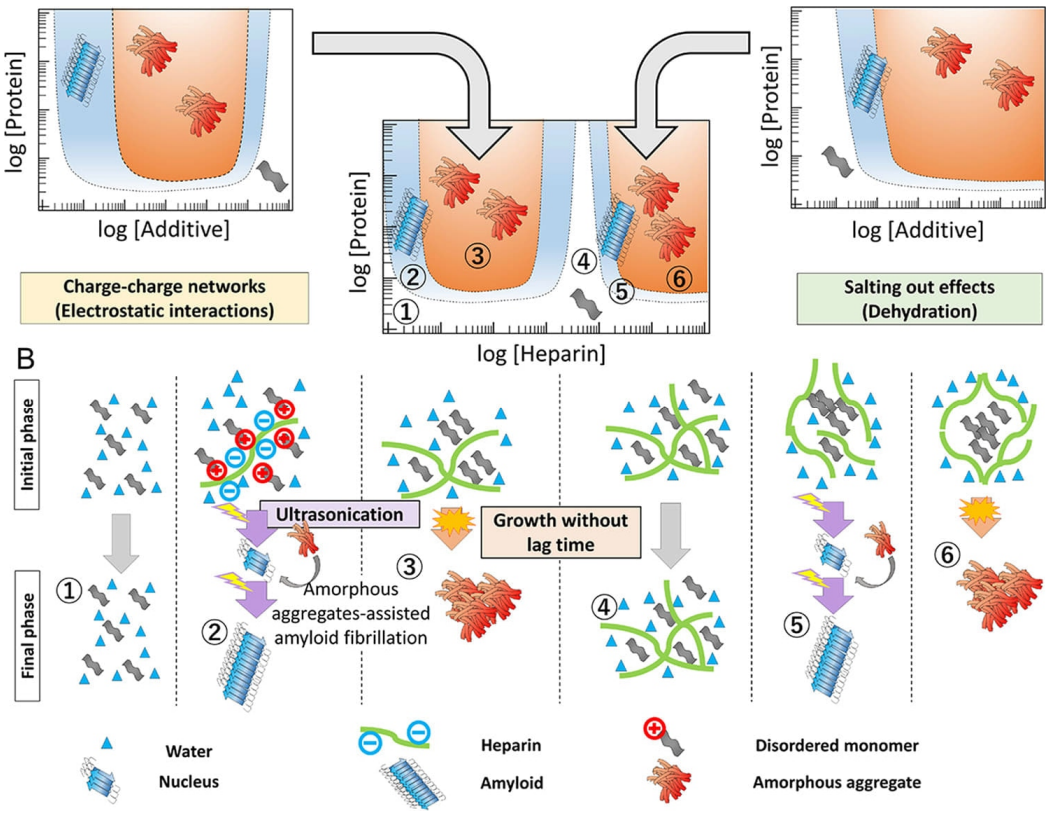

Figure 8. Mechanism of HEWL protein in the presence of heparin *A, Effect of heparin on the aggregation of Hen egg while lysozyme (HEWL) protein and the mechanism behind the aggregation [139].*

2.6 Nuclear Magnetic Resonance (NMR)

Nuclear Magnetic Resonance (NMR) spectroscopy is a non-disruptive, powerful tool to study the structure and dynamics of biomolecules. It has been extensively utilized to study the structure of proteins and their interaction with other proteins, chaperones, or small molecules. In addition, studies of dynamic processes like ring flip or local structural changes, the effect of salt, pH, buffer, concentration, and temperature are successfully performed using NMR spectroscopy.

Over the past few years, NMR has demonstrated technical advancements to understand and solve biological systems [142]. With the availability of high magnetic fields and cryogenic probes, the sensitivity of NMR has increased. Multidimensional (3D-7D) experiments have solved the problem of chemical shift overlap and spectral degeneracy [143]. The developed processing algorithm and non-uniform sampling [144, 145] have improved data collection capabilities without time restraints. Technical advancements like TROSY [146, 147] and Residual Dipolar Coupling (RDC) [148] allowed solution NMR to solve the structure of larger proteins.

NMR can be utilized to study protein in solution as well as precipitates and crystallites, *i.e.*, situations where anisotropic interactions are not averaged due to molecular tumbling. The structure of a protein could be elucidated by solution NMR only when it is soluble in a buffer. Therefore, solution NMR cannot characterize the structure of amorphous, small crystallites or samples without long-range order. On the other hand, solid-state NMR is a great tool to characterize membrane proteins, amyloid fibrils, or microcrystals. The developments in pulse sequences, labeling methods, and fast spinning have provided significant advancements to structure elucidation by solid-state NMR.

Unlike other spectroscopies, NMR spectroscopy is based on observing signals originating from nuclei with non-zero spin angular momentum. NMR for biological samples is popular for the nuclei with spin ½. However, the constituting isotopes of biological samples like ^{12}C or ^{14}N either do not have any overall spin or is less sensitive with large quadrupole moment. Therefore, isotopic labeling with ^{13}C and ^{15}N by recombinant expression is a common practice for preparing NMR samples. The general principle to determine the spin quantum number (I) or total angular momentum of nuclei is based on the number of neutrons and protons in the nucleus. A nucleus has zero spin if the number of protons and neutrons is even. While, ½ integral spins (1/2, 3/2) are the result if neutrons plus protons are odd. In case the neutrons and protons are both odd, then nuclei have an integral spin (1,2,3) [149].

At standard conditions and room temperature, all the spins are randomly oriented and have a energetically degenerate state [149, 150]. Since the spins are quantized, the application of

magnetic field (B0) lifts the degeneracy with spins in 2I+1 possible orientations, where I is the spin quantum number of the nuclei. Each energy level is denoted by the magnetic quantum number m. For spin ½, the nuclei can orient in two $\left(\left(2 * \frac{1}{2}\right) + 1\right)$ orientations denoted as -1/2 or +1/2 energy levels. From the traditional NMR perspective, -1/2 is denoted as α, and ½ is denoted as β. When the magnetic field is applied in the z-direction, then the energy for that particular level is given by:

$$E = -\mu_z B_0$$

where μ_z is the magnetic moment. The relation between the magnetic moment and the angular moment is given by the gyromagnetic ratio, which is specific to the nucleus, as follows:

$$\gamma = \frac{\mu}{I}$$

Hence, the energy of a level can be denoted as: $E = -\gamma I_z B_0 = -\gamma m \hbar B_0$ where $\hbar$ is the reduced Planck's constant.

The transition energy is the energy difference between two levels, is given by:

$$\Delta E = \gamma \hbar B_0$$

The above equation proves that the transition energy depends on the applied magnetic field and the nuclei. Therefore, the signal intensity in NMR is proportional to the energy gap and dependent on the applied magnetic field and the gyromagnetic ratio. Hence the sensitivity of the NMR experiment can be improved by a higher magnetic field and the use of a nucleus with a high gyromagnetic ratio.

The spin precess in the presence of a magnetic field because of its intrinsic angular momentum. The angular frequency of precession is known as Larmor frequency (ω). The relationship between energy and frequency is defined as:

$$E = \hbar\omega$$

where Larmor frequency is described as: $\omega = -\gamma B_0$.

To excite the spins in the ground state, typically, radio frequency is required to achieve resonance conditions with a magnitude equivalent to the Larmor frequency: $\nu = \omega = -\gamma B_0$. With the application of radio frequency, the net spin magnetization precess at the z-axis inclines away from the axis, as shown in figure 9A. The magnetization relaxes towards the z-axis and attains an equilibrium state when the radio frequency is stopped. This process of magnetization decay from an excited state to its equilibrium state is known as free induction

decay, which is Fourier transformed to provide the NMR signal. The resonant frequency of the nuclei in the presence of a magnetic field is known as a chemical shift. The nuclei are surrounded by electrons, creating small differences in local magnetic fields experienced by the nuclei. This phenomenon is known as shielding. Therefore, chemical shift is highly dependent on the electronic environment around a nucleus or the chemical environment, and the same type of nuclei in the different local environments can be differentiated from others. The chemical shift is represented as part per million as described in the equation below:

$$\delta = \frac{\nu_{sample} - \nu_{reference}}{\nu_{reference}} * 10^6$$

where TMS is mostly used as a reference in solution.

9 A. B.

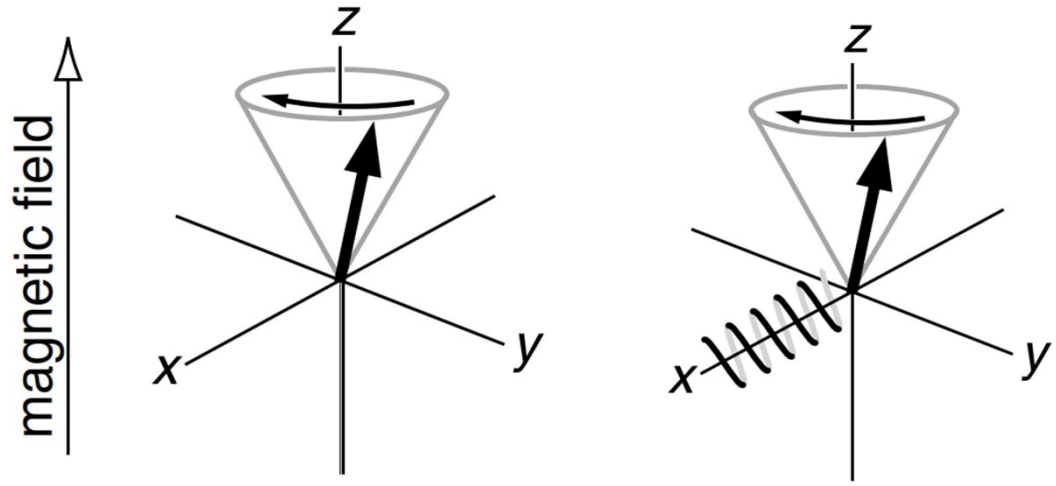

Figure 9 Spin precession in the presence of magnetic field. *A, Precession of magnetization vector, which sweeps a cone at a constant angle to the z-axis. B, The magnetization induces a current in the coil, which is depicted in x-axis [150].*

2.6.1 Magic Angle Spinning (MAS)

The internal interactions among nuclei, like dipolar coupling, anisotropic scalar coupling, and chemical shift anisotropy get averaged out in solution because of tumbling resulting in narrow peaks. The rapid tumbling of molecules averages out the ($3\cos^2$-Θ) (term present in anisotropic chemical shift tensor and hetero dipolar coupling) dependency on transition frequency. Since mobility is reduced in solids, all the orientation-dependent interactions are present in solid-state NMR, leading to broad spectra. The challenge was solved by E.R. Andrew and I.J. Lowe [151], who proposed that artificially rotating the sample at an axis inclined to an angle of 54.7° with respect to the applied magnetic field, figure 10, can

suppress these interactions. This angle is known as magic angle. The fast spinning (spinning frequency faster or a few times faster than the interaction) of the sample at magic angle can remove heteronuclear dipolar coupling, chemical shift anisotropy, and second-order tensor interactions [152]. The spinning of the sample reduces the powder pattern to mostly a sharp line with some spinning sidebands. Spinning sidebands are sharp lines in addition to the isotropic chemical shift which are spinning speed apart. The isotropic chemical shift does not change its position with a change in spinning speed, which is a way to differentiate the isotropic chemical shift from the spinning sidebands.

10 A.

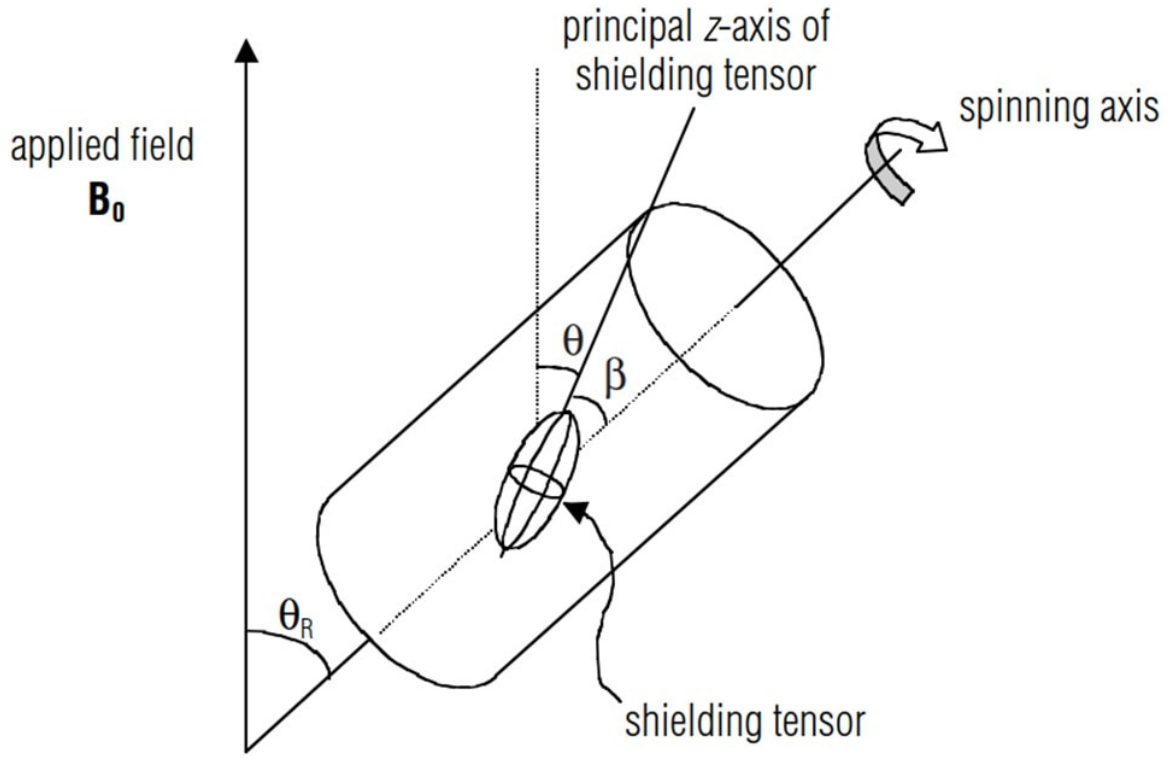

Figure 10 Spinning at magic angle. *A, Schematic representation of magic angle experiment, where rotor is inclined at 54.7^{o} with the applied magnetic field [152].*

2.6.2 Cross-Polarization (CP)

The non-crystalline, microcrystalline, or insoluble proteins or aggregates are extensively characterized by solid-state NMR. However, solid-state NMR has certain disadvantages like homonuclear coupling, line broadening, etc. The naturally abundant magnetically active protons cannot be detected by solid-state NMR because of the strong dipolar coupling between protons. Instead of protons, rare nuclei like ^{13}C and ^{15}N are used for solid-state NMR experiments. However, these nuclei are not abundant in nature and require isotopic labeling of the proteins. Additionally, these nuclei have a low gyromagnetic ratio resulting in low sensitivity and attenuated signal. Cross-polarization is used for transferring the

magnetization from abundant nuclei like ^{1}H to rare nuclei like ^{13}C and ^{15}N, hence enhancing the sensitivity. It is based on the heteronuclear dipolar coupling and of prime importance in most of the solid-state NMR pulse sequences. The cross-polarization is achieved by matching the Hartmann-Hahn condition [153]. In a cross-polarization pulse sequence, a 90^{o} x -pulse is applied on ^{1}H, which creates magnetization in the –y direction, as shown in figure 11. Two simultaneous contact pulses are applied on ^{1}H and X in such a way that their amplitude matches the Hartmann-Hahn condition in the rotating frame.

$$\gamma_H B_1(^1H) = \gamma_X B_1(X)$$

The matching of the Hartmann-Hahn condition creates an equal energy gap between spin states of ^{1}H and X. Therefore, the transition energy of ^{1}H spin states can be compensated by the relaxation of spin states of X nuclei while maintaining a constant energy of the system in the rotating frame. This allows the enhancement of the signal from the dilute nuclei.

11 A.

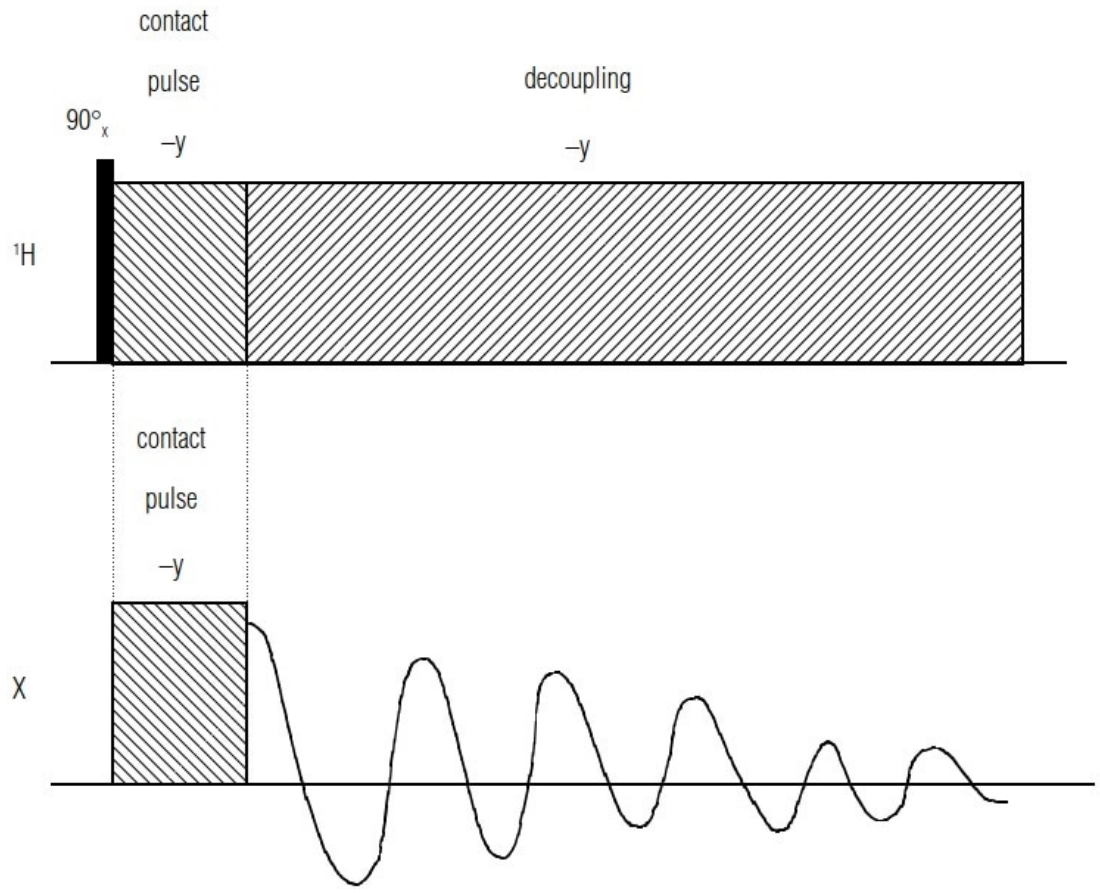

Figure 11 Pulse sequence for a cross-polarization. *A, Depiction of pulse sequence of cross-polarization, which is utilized to transfer mangnetization from abundant nuclei (1H) to dilute nuclei(X) [152].*

2.6.3 Assignments by solid-state NMR

The assignment of nuclei is an essential prerequisite to determine the structure of proteins by NMR. The assignment of proteins in solution follows a standard procedure with a ^{1}H-^{15}N correlation spectrum (HSQC) as a basis for the double-labeled (^{13}C,^{15}N) protein followed by 3D spectra such as HNCA, HNCO, HN(CA)CO etc. The nuclei (^{1}H, ^{15}N) of amino acids are sequentially linked with their own and the preceding or the following. The chemical shift of carbon (Cα and Cβ) provides information on the amino acid type, which is further mapped over the protein sequence to assign it. The recent advancements aim to reduce the experimental time by employing methods like NUS, brand-selective excitation, and the possibility of characterizing larger proteins with experiments like TOCSY.

Generally, the ^{1}H suffers from broad linewidths due to the strong homonuclear coupling in the solid-state NMR spectrum, which affects the assignment experiments. ^{13}C detection is preferred over ^{15}N at slow to moderate MAS frequencies (10-60 kHz) because of its higher gyromagnetic ratio. The standard approach for solid-state NMR assignment is to record ^{13}C-^{13}C and ^{13}C-^{15}N correlation spectra followed by ^{13}C-^{15}N 3D correlation experiments.

The assignment begins with the acquisition of ^{13}C-^{13}C correlation spectrum like dipolar-assisted rotational resonance (DARR) [154] or Proton-driven spin diffusion (PDSD) [155]. The 2D correlation with short mixing time depicts only the intra-amino acid correlations. The quality and homogeneity of the sample can also be determined from this spectrum. Amino acids like Isoleucine, Valine, Serine, and Threonine have specific aliphatic chemical shifts which can easily be counted. The homogeneity of the sample is investigated by comparing the amino acids observed in the spectrum with the sequence. The spectrum displays aromatic and carbonyl resonances with the aliphatic carbons allowing the pairing of resonances easier, hence reducing the ambiguities.

The NCA experiment provides information on amino acids visible in the sequence. The experiment will observe all the resonances in the structured region of the homogenous amyloid sample. The magnetization is transferred from ^{1}H, via cross-polarization, to ^{15}N, which is then further transferred to $^{13}C\alpha$. The experiment depicts the correlation of ^{15}N-$^{13}C\alpha$ of the same amino acid where the chemical shift is evolved on ^{15}N and magnetization is transferred to ^{13}C for detection.

After identifying the C-C spins and the residues, the assignment of resonances is performed by 3D experiments like NCACX and NCOCX, as shown in figure 12A [156]. NCACX and NCOCX are sufficient for smaller proteins to identify all the resonances. However, CONCA or CANcoCX is recorded in addition to NCACX and NCOCX to reduce the ambiguities in the assignments. The i^{th} resonance is identified in the NCACX, sequentially linked to the $i\text{-}1^{th}$

resonance in the NCOCX spectrum, as depicted in figure 12B. For 3D experiments, the first step is cross-polarization to transfer magnetization from ^{1}H to ^{15}N, which is then selectively transferred to $^{13}C\alpha$ (NCACX) and ^{13}CO (NCOCX). The magnetization is further transferred to nearby ^{13}C nuclei via a DARR or PDSD step. The chemical shift is evolved at ^{15}N and $^{13}C\alpha$ (for NCACX) or ^{13}CO (for NCOCX) and detected at ^{13}C nuclei.

12 A. B.

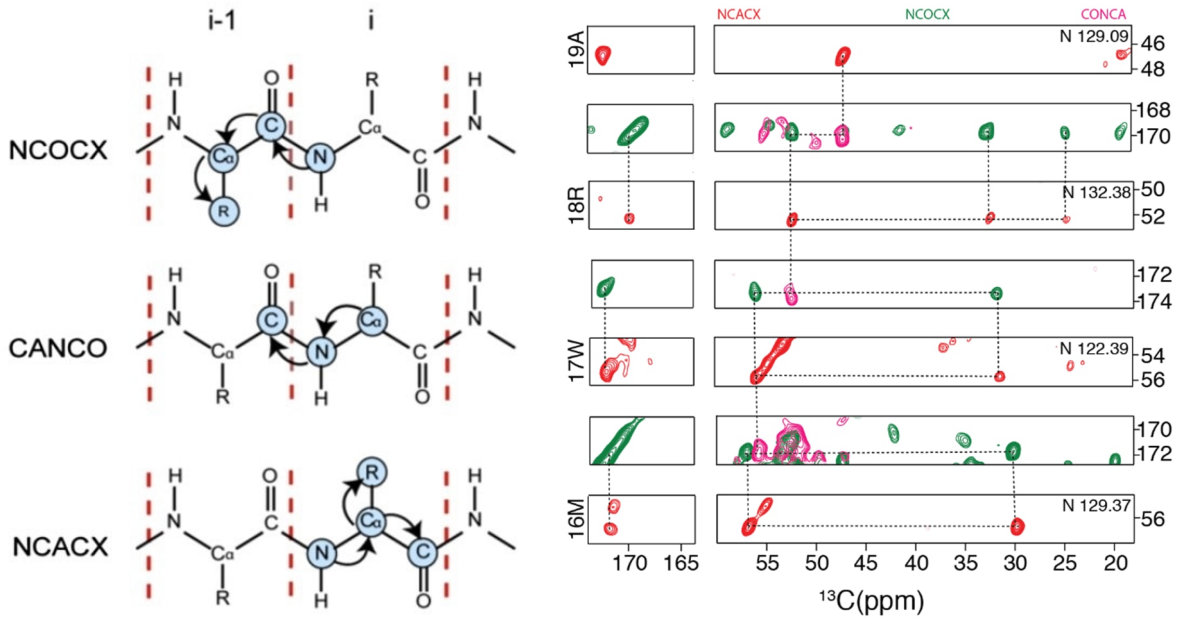

Figure 12 Sequential assignment by solid-state NMR. *A, Schematic representation of magnetization transfer in NCACX, NCOCX, and CANCO experiment [157].B, Sequential assignment of protein using solid-state NMR 3D experiments.*

2.6.4 Prediction of Long-range interactions

Following the assignment of the protein, the secondary structure is identified. The secondary structure of the amyloid is predicted using the information on chemical shifts of Cα and Cβ resonances [158]. The difference between the observed chemical shifts with the chemical shifts of the random coil provides the secondary structure of the region. For Cα, the resonances are in the alpha-helical region if the difference in chemical shifts is positive, while it is negative for the β-sheets. The random coil has a chemical shift index (chemical shift observed – chemical shift random coil) of zero. The chemical shifts for Cβ display opposite behavior, where the negative difference suggests alpha-helical environment while a positive difference means β-sheets. The dihedral angles are predicted mainly through software called TALOS (Torsion Angle Likelihood Obtained from Shifts and sequence similarity) [159], which utilizes the high-resolution crystal structure of a protein. The TALOS predicts the average ϕ and ψ angles by comparing the sequence and amino acids in the

database. It also displays a window with the color-coded protein sequence, where green signifies a good prediction, yellow means ambiguous and red signifies bad.

13 A.

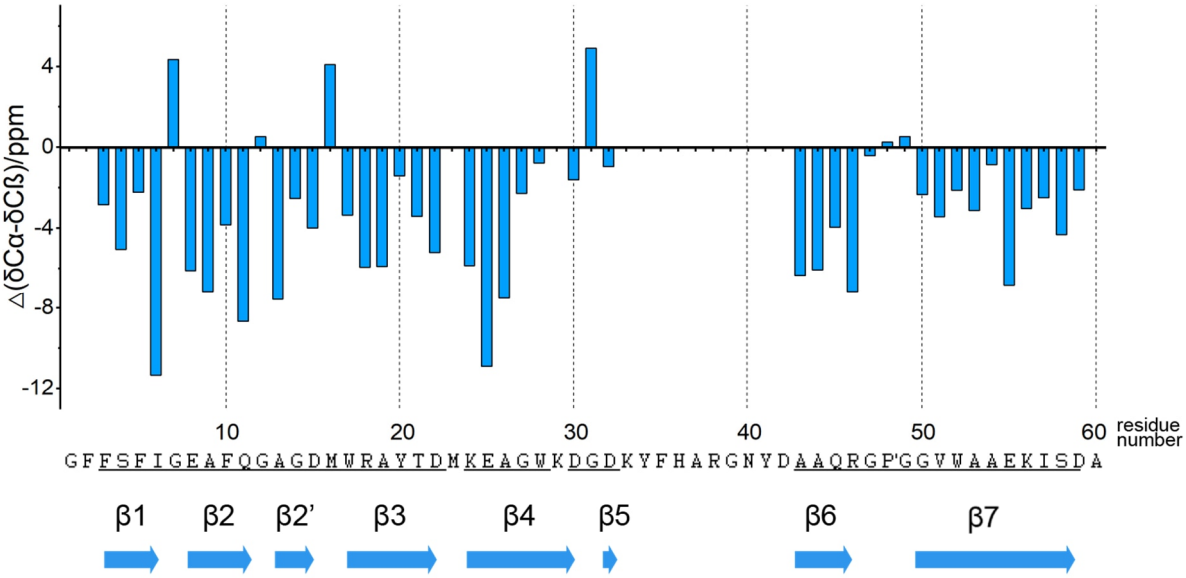

Figure 13. Chemical shift index *A, Secondary structure prediction of protein from the difference of observed chemical shift from the chemical shift of random coil.*

The long-range connectivities are determined by long-mixing proton driven spin diffusion experiments like DARR or PDSD [154]. In addition to these experiments, Proton Assisted Recoupling (PAR) experiments are recorded for reducing the ambiguities. The off-diagonal resonances in the spin diffusion experiments provide information on nearby ^{13}C nuclei in space [160]. The DARR is a rotor and proton driven mechanism, where satisfying the rotary resonance condition recovers ^{13}C-^{1}H interaction. This is achieved by a CW irradiation on ^{1}H, with which the ^{1}H intensity fulfils rotary resonance condition of $\nu_1 = n\nu_R$. This leads to overlap of sideband of one resonance to the dipolar powder pattern of other resonance, which give rise to spectral overlap necessary to create energy conservation for efficient polarization between two ^{13}C spins. These spin diffusion experiments contain information on internuclear distances (in proportion to 1/r6). Therefore, DARR or PDSD with shorter mixing times provides intra-amino acid connectivities, while longer mixing times provide information on long-range correlations.

Proton-assisted recoupling (PAR) is a third spin-assisted recoupling (TSAR) [161] mechanism to transfer the polarization from 1H to dipolar ^{13}C-^{13}C or ^{15}N-^{15}N spins. It is a second-order recoupling method unaffected by dipolar truncation or attenuation. Dipolar truncation is the biggest disadvantage faced by the RFDR in studying long-range

interactions. This affects the distance extraction from uniformly labelled ^{13}C-^{13}C protein by RFDR. Different peaks observed in DARR and PAR is shown in figure 14.

14 A.

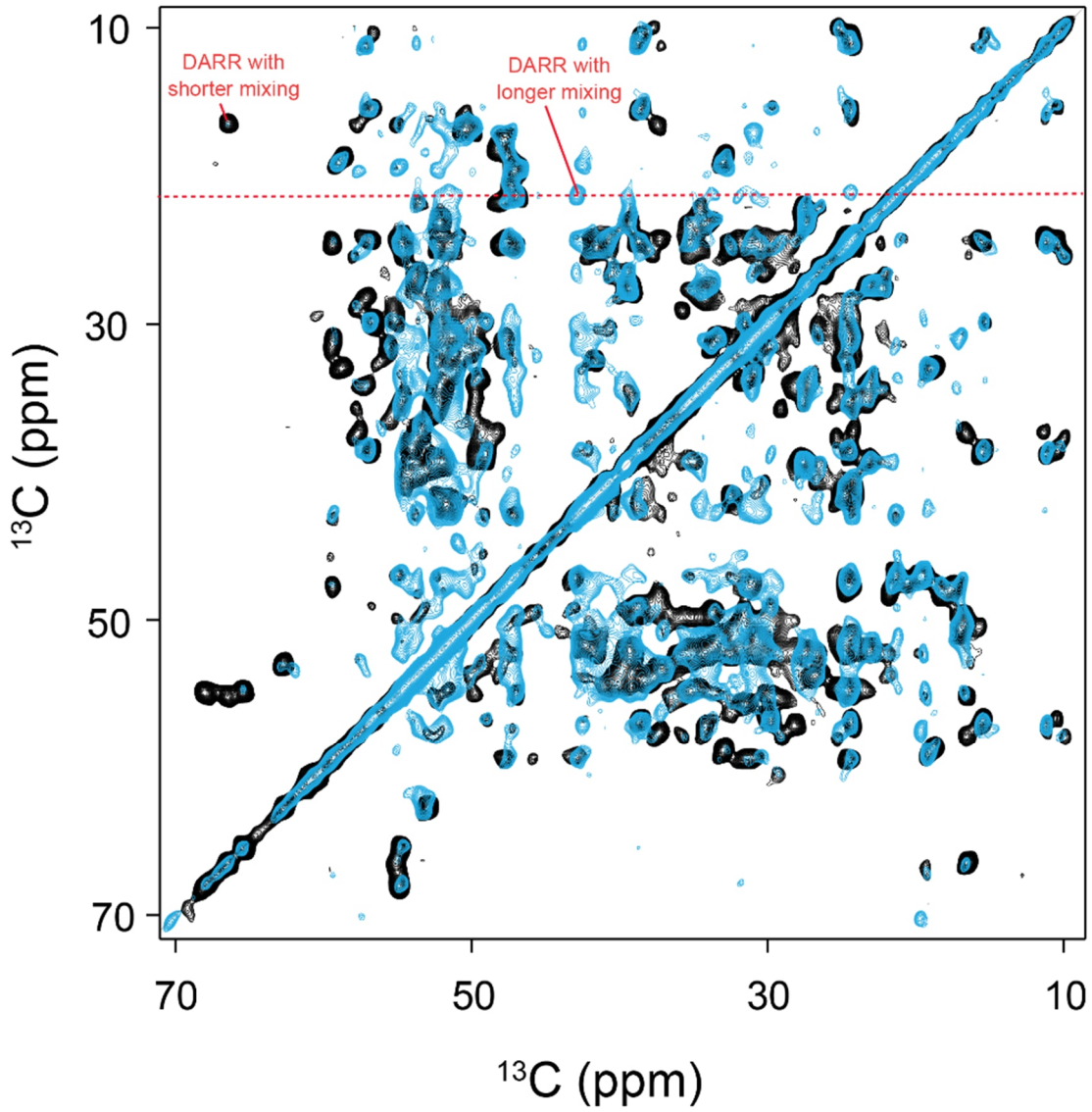

Figure 14. Long-range connectivities. *A, Overlay of DARR with different mixing times to predict the long-range interactions.*

The long-range interactions between dipolar coupled heteronuclear spins are further identified with Transferred Echo Double Resonance (TEDOR), as shown in figure 15A. It is a rotor-synchronized solid-state NMR pulse sequence to observe dipolar coupled nuclei (I, S) [162]. First, cross-polarization transfers the magnetization from protons to rare nuclei I (^{13}C or ^{15}N). Next, rotor synchronized π-pulses are applied on S-spins to dephase the magnetization on I. This leads to coherence transfer after n rotor periods, which is transferred to S by applying a simultaneous π/2 pulse on I and S at the end of the rotor period. Finally, the transferred coherence is observed by applying rotor synchronized π-

pulses on I-spins. The signal from S-spin can be observed in 1D, 2D, or 3D experiments. The detrimental effect of homonuclear J-coupling in TEDOR is minimized by utilizing z-filter periods, leading to pure absorptive spectra [163].

15 A.

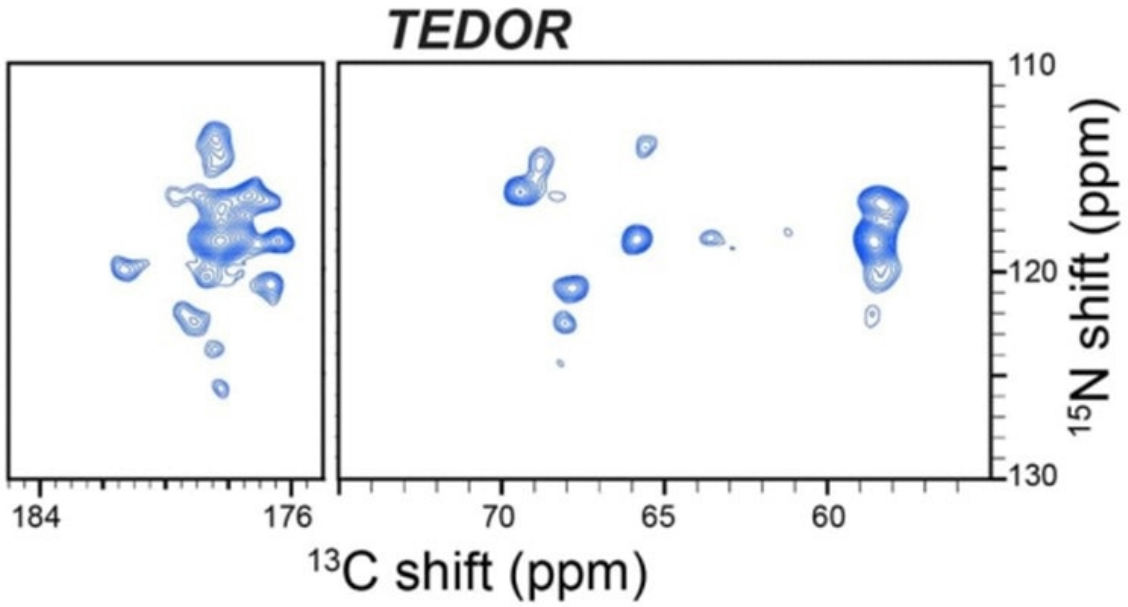

Figure 15. Prediction of long-range connectivities by amide side-chain *A, TEDOR spectra to depict the long-range connectivities [164].*

2.6.5 Characterizing Dynamic part of Amyloids

The fibrils may comprise some structured and some flexible regions. Therefore, the overall fibril structure characterization requires understanding the regions and amino acids comprising these regions. Insensitive nuclei enhanced polarization transfer (INEPT) is one of the methods utilized to investigate the highly dynamic and flexible regions by solid-state NMR [165]. INEPT is a commonly used pulse sequence in solution NMR for J-based couplings. However, the rigid regions have shorter T2 relaxation time; hence CP is extensively used in solid-state NMR. Since that is not the case for flexible regions, it is studied using the INEPT.

The J-coupled heteronuclear signal from resonances in the flexible region is achieved using refocused INEPT sequence [166]. The sequence comprises the simultaneous application of π pulse at ^{1}H and ^{13}C with a delay of t before and after the pulse, proportional to 1/(4JCH), creating an antiphase proton coherence. Then, simultaneous π/2 pulses are applied to convert the antiphase proton coherence to antiphase carbon coherence. The antiphase coherence is finally refocussed to an observable ^{13}C signal by application of the t'-π-t' sequence.

2.7 Scope of the Study

Serum Amyloid A 1.1 is the main component of AA amyloidosis. The poor solubility and unstable nature of SAA makes it difficult to characterize it in the solution. The structure of SAA fibrils has been deduced by cryo-EM, which verifies that SAA is polymorphic in nature. However, the cryo-EM provides structure of selected particles. On the other hand, solid-state NMR can characterize the structure of fibrils in bulk. The current study employs solid-state NMR to characterize the structure of fibrils and combining the results with other biophysical methods to understand the structure and stability of SAA. The thesis aims to fulfil following objectives:

Structural Characterization of SAA by solid-state NMR and comparison of structure of SAA fibrils in bulk with the structure deduced by cryo-EM.

The chapter describes the results from the biophysical characterization like CD and Fluoroscence spectroscopy of SAA protein in buffer. It further explores the change in the spectroscopic results with the increase in temperature to understand the aggregation process. The labelled SAA fibrils were investigated using solid-state NMR spectroscopy. The resonances were assigned and long-range connectivities were identified. Finally, the long-range interactions and secondary structure positions were compared with the structure deduced by the cryo-EM and possible morphologies were proposed on the basis of results from molecular dynamics. The effect of seeding with respect to its impact on the structure and polymorphs was also investigated.

Effect of heparin on the aggregation mechanism of SAA and on the structure of SAA fibrils.

As reported before in the section 2.5, heparin and heparan sulfate have considerable effect on the amyloid formation. The study reports for the first time, the mechanism of SAA fibril formation in the presence of fibrils. Furthermore, it identifies the resonances involved in the binding with heparin by comparing the NMR spectra for SAA seeded fibrils prepared in the presence of heparin to the seeded fibrils prepared without adding heparin. In addition, it stipulates the effect of heparin on the polymorphism of SAA with the comparison of non-seeded SAA fibrils prepared in the presence of heparin and non-seeded SAA fibrils without heparin.

Interaction of SAA with lipids

The SAA protein in physiological environment remains associated with their lipid counterpart. As a result, free SAA is unstable and has low solubility in the buffer. The chapter exhibits the behavior of SAA in the presence of lipids using biophysical characterization. CD

spectroscopy was employed to investigate the melting temperature, secondary structure and aggregation process in the presence of lipids and nanodiscs. The fluorescence spectroscopy depicted the role of non-polar environment on the stability of SAA protein. Finally, TEM was used to identify the result of nanodiscs and SAA protein constitution.

On the whole, these results identify the solution conditions, where SAA form fibrils and role of lipids in the stability of protein. It further determines the role of seeding in the homogeneity of the structure of fibrils and give an insight on the difference between structure of bulk fibrils with the selected fibril particles. In addition, it investigates the role of cellular component like heparin on the stability, structure, and mechanism of SAA fibrils. The conclusions from the current project provide an insight on the mechanism and impact of these GAGs on AA amyloidosis and can be utilized in future for therapeutic purposes.

3. Materials and Methods

3.1 Materials

3.1.1 Chemicals

The isotopically labeled glucose (^{13}C) and ammonium chloride (^{15}N) was supplied by Cambridge Isotope Laboratories (Tewksbury, USA). All the chemicals were purchased from Sigma Aldrich Chemie (Taufkirchen, Germany), Iduron (Manchester UK), VWR International (Ismaning, Germany), Carl Roth (Karlsruhe Germany), Roche Diagnostics (Unterhaching, Germany), Serva Electrophoresis (Heidelberg, Germany). The lipids were purchased from Avanti Polar lipids Inc. (USA).

3.1.2 Equipment

Equipment	Supplier
Autoclave Varioclave EP-Z	H+P
Centrifuge	
Centrifuge 5804 R, Rotor: A-4-44	Eppendorf
Avanti J25 and J26 XP	Beckman coulter
Universal R	Hettich
Sorvall Lynx 6000 centrifuge	Thermo Fischer Scientific
Table top centrifuge 5414 C	Eppendorf
CD spectrometer J-715 Spectropolarimeter	Jasco
Cold circulation thermostat	Julabo
Temperature control CD spectrometer	PTC-348WI Jasco
Clean bench Herasafe KS	Thermo Fisher Scientific
Chromatography systems	
AKTA FPLC (purifier)	GE Healthcare
AKTA prime	GE Healthcare
HPLC Purification system UltiMate 3000	Thermo Fisher Scientific Waltham

Chromatography columns	
Desalting column	GE Healthcare
HiSTrap FF	Cytiva
HPLC column ECOPLUS (TAC10/250G2-SR-1)	Kronlab Chromatography Technology Dinslaken, Germany
MBPTrap HP Column	Cytiva
Ni-NTA resin	Qiagen
Superdex® 200 Increase 10/300 GL	Cytiva
Dynamic Light Scattering Detector DynaPro NanoStar	Wyatt Technology
Electronic balance	
BP 121 S	Sartorius
BL 310	Sartorius
Electron Microscope 1400 plus microscope	JEOL
Fluorescence Spectrometer FP-3800	Jasco
Fluorescence spectrometer - Temperature control	ETC-815 Jasco
French Press HTU DIGI-F	G.Heinemann
Frac -950 fraction collector	GE Healthcare
Super loops	GE Healthcare
Gel documentation System Biotec II	Biometra
Gel electrophoresis systems Julabo	Serva
Homogeniser Ultra Turrax DIAX900	Heidolph
Incubator cell cultures MaxQ™8000	Thermo Scientific
Incubator 37ºC for plates Heraeus	Thermo Fisher Scientific
Liposome extruder	Hamilton
Lyophilizer Alpha 2-4 LD plus	Christ Osterode am Harz
Magnetic stirrer Heidolph MR200	Heidolph
NanoDrop 2000 Spectrophotometer	Thermo Scientific
Nuclear Magnetic Resonance	
pH electrode Blue Line 14	SI analytics
pH meter tabletop unit Lab 850	SI analytics
Plate reader SpectraMax®iD5	Molecular Devices
Plate reader GENios	Tecan
Rotors	Brucker

Rotor packing tool	Giotto
Shaker Rotamax 12	Heidolph Instruments
Sonicator Sonoplus	Bandelin
Sonicator with water bath Sonorex	Bandelin
Thermomixer	Eppendorf
Thermoblock TB	Biometra
Ultra-Filtration cell 8050	Amicon
Vortex MS2	IKA
Water bath F6-K	Haake

3.1.3 Enzymes, Standards and Kit

The DNA and protein ladders were purchased from Serva. NEB or Promega supplied the dyes and enzymes. The antibiotics were obtained by Sigma Aldrich. The DNA purification kit, used for miniprep, was purchased by Wizard plus Promega.

3.1.4 Bacterial Strain

The pMAL-c2 vector with Histidine and maltose-binding protein (MBP) tag and TEV cleavage site was a kind gift from Prof. Marcus Fändrich (Institute of Protein Biochemistry, University of Ulm). In addition, *E. coli* XL1-Blue cells were supplied from Stratagene (Agilent Technologies Deutschland GmbH, Waldbronn, Germany).

3.1.5 Buffer and solutions for Bacterial growth

Buffer	Composition
LB media	10 g Peptone 140 5 g Yeast Extract 5 g Sodium Chloride
M9 (10X)	Na2HPO4 (60 g) KH2PO4 (30 g) NaCl (5 g)
Trace elements (100 X)	EDTA pH 6.5 (5 g) $FeCl_3.6H_2O$ (0.83 g) $ZnCl_2$ (84 mg) $CuCl_2.6H_2O$ (13 mg) $CoCl_2.6H_2O$ (10 mg) H_3BO_4 (10 mg)

	$MnCl_2.6H_2O$ (1.6 mg)
Minimal Media	M9 100 ml Trace elements 10 ml MgSO4 1 M $CaCl_2$ 1 M Thiamin- HCl 1 mg/ml Biotin 0.1 mg/ml Glucose 0.2 % $^{15}NH_4Cl$ 0.05 %
Antibiotics	Ampicilin 1 mM

The media was always sterilized by autoclaving at 121^{o}C for 20 minutes. The antibiotics and other heat-sensitive enzymes and chemicals were filter sterilized using 0.22 µm filters and stored at -20^{o}C.

3.1.6 Software

Software	**Provider**
Adobe Illustrator	Adobe
Amylofit	Knowles Group
ApE- A plasmid editor	Equi4 software (M. Wayne Davis)
CcpNMR 2.4.2	Plone and python (Funded by UK Medical Research Council)
EndNote	Clarivate
Topspin 3.5 (NUS plugin)	Bruker

3.1.7 Database

Database	**Link**
BMRB	https://bmrb.io/
PDB	https://www.rcsb.org/
Pubmed	https://pubmed.ncbi.nlm.nih.gov/
ProtParam	https://web.expasy.org/protparam/

3.2 Methods

3.2.1 Transformation of E. coli

The pMAL-C2 plasmid was transformed into competent BL-21 *E.coli* cells to express the SAA1.1 protein. A 50 µl *E.coli* aliquot was thawed on ice and around 100 ng of DNA was added to the competent cells. The mixture was incubated at ice after mixing gently, for 30 minutes. The heat shock treatment was given to cells by incubating them at 42^{o}C for 45 seconds and placed on ice for 2 minutes. The cells are incubated in 1 ml LB for 1 hour and centrifuged at 6000 rpm for 2 minutes. The pellet was suspended in the remaining liquid after discarding the supernatant. This was spread on an LB agar plate containing Ampicillin. The exact transformation process was repeated for the plasmid containing the MSP gene for nanodisc preparation. The suspended pellet was spread on an LB agar plate containing Kanamycin.

3.2.2 Isolation of plasmid DNA from E. coli

Single colonies were picked from an LB agar plate incubated with the competent cells with the required vector. The bacteria were incubated overnight at 37^{o}C under constant shaking. Then, the cultured cells were centrifuged at 4000 rpm at 4^{o}C for 10 minutes. The cell pellet obtained after centrifugation was used with the subsequent isolation steps provided as per the manufacturer's instructions with a Miniprep DNA purification kit. The elution was carried out with 20 µl ddH2O. The eluted plasmid is stored at -20^{o}C after determining the concentration.

3.2.3 Protein Expression and Purification of SAA 1.1

The pMAL-C2 vector consists of the gene expressing the SAA1.1 protein and the antibiotic-resistance gene for ampicillin. The transformed cells are incubated in 100 ml LB media at 37^{o}C overnight in the presence of ampicillin. The overnight culture is termed as pre-culture. For unlabeled protein, the inoculation was added in LB media containing ampicillin such that the initial OD was 0.1. The labeling was performed using M9 media with ^{15}N labeled ammonium chloride and ^{13}C labeled glucose as energy sources. The cells were allowed to proliferate at 37^{o}C until an OD of 0.6 had reached. The cells were induced with 1mM IPTG at this OD and were further allowed to grow at 37^{0}C for 6 hours.

After 6 hours, these cells were harvested by centrifuging at 6000 rpm for 20 minutes. Then, the supernatant was discarded, and the cell pellet was suspended in Amylose A buffer. Cell pellets were stored at -80^{o}C after freeing with liquid nitrogen, when the purification does not continue after harvesting.

For the purification of SAA 1.1, the following buffers were used:

Cell lysis and MBP Purification	
Amylose A	Tris pH 7.5: 20 mM NaCl: 200 mM
Amylose B	Tris pH 7.5: 20 mM NaCl: 200 mM Maltose: 10 mM

NiNTA purification	
NiNTA A	Tris pH 8.0: 20 mM NaCl: 150 mM
NiNTA B	Tris pH 7.5: 20 mM NaCl: 150 mM Imidazole: 500 mM

Reverse phase purification	
RPC A	TFA: 0.1% H2O
RPC B	Acetonitrile: 86% TFA: 0.1% H2O

Cells were suspended in the cell lysis buffer, and a tablet of EDTA-free protease inhibitor (Roche, Penzberg, Germany) and DNase was added. The cells were lysed by the French press followed by centrifugation at 24000 g at 4^{o}C. The supernatant was filtered to remove the remaining cell debris, and the filtrate was used for purification.

The supernatant was applied to a 5ml MBP column equilibrated with Amylose A buffer. First, the washing was performed using the Amylose A buffer. Next, the protein was eluted with 100% Amylose B buffer. The fraction with UV280 peak (≥200mAU) was collected and incubated with 8M urea for 1.5 hours at room temperature with very slow stirring. After 1.5 hours, the protein was diluted with 5X of NiNTA A buffer.

The diluted protein was applied to the NiNTA column and equilibrated with NiNTA A buffer. The washing was performed with 5% NiNATB buffer. The protein was eluted with 40%

NiNTA B buffer. The purified protein was diluted with 8X NiNTA A buffer and subjected to TEV cleavage overnight at 34°C, at a rotation of 50 min^{-1}, with a maximum of 5mM DTT. The TEV cleaves the MBP tag from the SAA protein. The pure protein was separated from the tag using the second NiNTA column. The pure protein was obtained in the flowthrough.

Reverse-phase chromatography was employed to perform the final step of the purification. First, the column was equilibrated with RPC A buffer, and the protein with 0.1% TFA was applied to the column. Next, the column was washed with 30% RPC B buffer. Different fractions were collected with a gradient of 30%-100% RPC B buffer. Finally, the fractions containing pure protein were determined using SDS-PAGE gel. These fractions were lyophilized and stored at -80°C.

3.2.4 Protein Characterization

3.2.4.1 SDS-Polyacrylamide gel electrophoresis (SDS-PAGE)

The purity and degradation of protein were analyzed by SDS-PAGE gels. The 15% SDS-PAGE gels were used to confirm the protein expression, fractions containing protein, and protein purity. The 15% SDS-PAGE gel was prepared with the following buffers:

	separating gel (15 %)	stacking gel (5 %)
H2O	35.5 ml	36 ml
40% Acrylamide	37.5 ml	6.25 ml
Tris 1.5 M pH 8.8	25 ml	-
Tris 1.5 M pH 6.8	-	6.3 ml
10% SDS	1 ml	0.5 ml
10% APS	1 ml	0.5 ml
TEMED	40 µl	50 µl

6 µl of 4X SDS dye was added to the 20 µl protein sample and mixed gently. The sample was heated at 95°C for 10 minutes and centrifuged for 5 to 20 minutes. Next, cell samples were centrifuged, and SDS dye was added to the pellet. The prepared sample was incubated at 95°C and centrifuged at 13000 g. Finally, 15 µl of the sample was loaded into the wells of the gel (15 µl supernatant was used for cells). The gel was run at a constant 15W for 40 minutes while gel chambers were cooled at 10°C.

The gel was taken out and placed in the fixation buffer. The gel was heated for 30 seconds and then allowed to shake for 5 minutes in the fixation solution. Then gel was stained with Coomassie staining buffer. The gel was again heated for 30 seconds and incubated for 10 minutes with constant shaking. Finally, the extra stain was removed, and the protein bands

were visible after treatment with the destaining buffer. The gel was heated in the destaining buffer for 30 seconds and then incubated at constant stirring until bands were visible.

3.2.4.2 Circular Dichroism (CD) Spectroscopy

CD Spectroscopy was used to determine the protein's secondary structure, melting curve, and stability. Measurements were performed using a J715 CD spectrometer with a Peltier unit (PTC-348WI), a thermostat (Julabo725), and a 0.1 cm path length quartz cuvette (Hellma). In order to perform CD measurement minimum 20 µM sample with a volume of 200 µl was used. The secondary structure of the protein was deduced by wavelength scan from 260 nm to 190 nm for five scans with a scanning speed of 100 nm/min. The structural characterization of SAA was performed at 4^{o}C.
Melting curves were recorded at the minimum wavelength observed in the corresponding CD spectra. Temperature scans were performed from 4^{o}C to 90^{o}C. The measurement was performed for every 0.5^{o}C with a temperature increase of 60^{o}C/h. The reverse temperature scan was performed to assess the refolding and the effect of the temperature on the protein.

3.2.4.3 Dynamic Light Scattering (DLS)

The DLS experiments were performed with DynaPro NanoStar instrument at 4^{o}C with 60 µl filtered sample. The measurements are executed with 10 scans to ensure accuracy. The correlation function obtained by measurements was converted to particle size using DYNAMICS software. The experiments were performed to analyze the diameter of the protein, its derivative, and its binding capabilities.

3.2.4.4 Transmission Electron Microscopy (TEM)

The amyloid fibrils and lipid and heparin-binding with SAA were characterized by negative stain transmission electron microscopy (TEM). The 300-mesh carbon coated Copper grids were activated by glow-discharge in an argon atmosphere for 30 seconds. 5 µl of 50 µM sample was incubated on grids for 1.5 minutes. The grids were washed with distilled water, and the excess water was removed by filter paper. The protein was stained with 2% Uranyl acetate for 30 seconds, and the excess stain was removed by filter paper.

Micrographs were recorded by JEOL 1400 plus microscope (JEOL) operated at 120 kV. The scale bar was applied using IMAGE J software.

3.2.4.5 Fluorescence Spectroscopy

The fluorescence intensity for tryptophan was recorded at 295 nm with a range of 250 to 700 nm. 10 µl, 100 µM protein samples were used with three scans to ensure the accuracy of the data. The spectra were recorded using a quartz cuvette at JASCO Spectrofluorometer FP-8300 equipped with a water bath cooling system. The difference in the fluorescence intensity and shift in maxima determines the change in the local environment of the tryptophan. The spectra describe the folding and unfolding of the protein.

3.2.4.6 ThioflavinT (ThT) Assay

ThioflavinT assay was performed to monitor the kinetics of fibril growth. The assay was executed in a 96-well plate in triplicates. The ThT assay was utilized in the current project to understand the mechanism of fibril growth of SAA and the effects of heparin and lipids. The fibril kinetics of SAA was performed with different concentrations of SAA ranging from 20 µM to 100 µM with 10 µM ThT dye. In addition, the effect of seeding was analyzed by adding seeds to varying concentrations of seeds from 1% to 10% seeds to 50 µM of SAA. Similarly, the impact of heparin was determined by using a range of heparin from 10X heparin to 100X heparin with 50 µM SAA.

The assay was prepared with one stock of filtered protein to maintain the uniformity of the sample. The protein and other additives (like heparin) were always kept at 4^{o}C not to allow the precipitation or aggregation of SAA protein. The 96-well plate was kept sealed for the whole duration of the experiment to avoid the evaporation of the buffer. The experiment was performed at 37^{o}C with constant stirring by exciting at 440 nm and recording the emission at 480 nm. The data was collected as an excel file and was plotted using Origin. The analysis was performed using the Amylofit software [167].

3.2.4.7 Pull-Down Assay

The pull-down assay was utilized to study the interaction of SAA with lipids:

1. The histidine-tagged MSP protein was reconstituted with lipids to form nanodiscs.
2. These histidine-tagged nanodiscs were incubated with SAA protein.
3. The Ni-NTA beads slurry was added to different Eppendorf to prepare the samples.
4. The storing solution was removed by centrifuging the beads at 500 g at 4^{o}C for 1 minute and discarding the supernatant. The beads were further washed with Milli-Q water by repeating the process of centrifuging at 500 g two times.
5. The beads were incubated with the protein sample by gently resuspending with the sample and allowed to rotate slowly for 1 hour at 4^{o}C.

After incubation, the samples were collected and centrifuged at 500 g for 2 minutes. The pellet and supernatant were collected separately. The pellet was again washed with 20 mM tris buffer (pH 8.5). The pellet, supernatant, and wash were prepared for SDS-PAGE, and the gel was run. If the protein binds with lipid, then the protein band will appear in the pellet; otherwise, it will be in the supernatant. The pull-down assay is used to isolate the complex where proteins are interacting. Hence the presence of a protein band in the pellet or supernatant infers the interaction between protein and lipids.

3.2.4.8 Nuclear Magnetic Resonance Spectroscopy

The SAA was characterized by solution and solid-state NMR to determine different properties of the protein and fibrils. The folding, interaction with lipids, and stability of SAA were analyzed using solution-state NMR. At the same time, the structure of SAA fibrils and the effect of heparin were established with solid-state NMR studies.

3.2.4.8.1 Solution Nuclear Magnetic Resonance Spectroscopy

All the solution state NMR measurements were performed in NMR tubes (500 µl) or Shigemi tubes (250 µl). The NMR samples were prepared in 10 mM Tris buffer at pH 8.5. The locking was performed at 10% D_2O, and the data was processed in TOPSPIN.

1D Spectrum

The protein sample was poured into the NMR tube and centrifuged to remove residual air bubbles. The signal was locked at 10% D_2O, shimming was performed, and finally, the signal was tuned and matched for ^{1}H, ^{15}N, and ^{13}C channels. The 1D experiments (optimized) were performed with a determined offset (O1) and calibrated 1H pulse (p1).

Titration and Temperature Studies

The effect of lipids and GAGs was identified using the ^{1}H-^{15}N HSQC of 50 µM SAA with additives (lipids or GAGs) at different concentrations. All the titration experiments were recorded at 277 K, and all the stability experiments were recorded by increasing the temperature from 277 K to 310 K with 5 K steps. The pulse of ^{1}H and ^{15}N was calibrated, and the water signal was suppressed before recording the spectra. The SAA is not stable at higher concentrations and temperatures in the buffer. Therefore, backbone assignment was not recorded for SAA in the buffer.

3.2.4.8.2 Solid state NMR

The magic angle setting was calibrated using powder Potassium bromide (KBr) for solid-state NMR. All the measurements were performed using Bruker 1.9 mm ZrO2 MAS rotor and MAS probe 750 MHz spectrometer. The chemical shift referencing was performed internally using the DSS solution.

Sample preparation

The non-seeded fibril sample was prepared by incubating SAA at 37°C at a concentration of 50 µM in 20 mM Tris at pH 8.5 in a shaker at 120 rpm for 10–14 days. Approximately, 10 mg of protein was utilized to prepare a solid-state NMR sample. The obtained fibrils are packed into a 1.9 mm ZrO2 rotor (Bruker) using a rotor packing device from Giotto Biotech. The packing tool was placed into a Beckman Coulter ultracentrifuge using an SW32Ti swinging bucket rotor. The centrifuge was operated at 28.000 rpm, yielding direct sedimentation of the fibrils into the MAS solid-state NMR rotor. The seeded sample was prepared similarly, except 5 % w/w *ex-vivo* seeds were added to the 50 µM SAA protein solution to catalyze fibril growth. To avoid bacterial growth, 0.02 % sodium azide was added to all the samples.

Assignment and long-range connectivities

The ^{13}C-^{13}C correlation of SAA-seeded fibrils was acquired by DARR with 30 ms mixing time and spinning at 16650 Hz MAS. For the long-range interactions, ^{13}C-^{13}C DARR correlations were obtained at 100, 300, 400, and 600 ms mixing times. In addition, the ^{13}C-^{15}N correlation spectrum was recorded at the same spinning. The 3D assignment was performed using NCACX, NCOCX, and CONCA experiments. For NCACX and NCOCX experiments, cross polarisation from ^{1}H to ^{15}N was performed using ramp shapes and subsequently ^{15}N -> CO or Ca cross polarisation employing rotor synchronised shaped pulses optimised employing optimal control. SPINAL 64 decoupling at 100 kHz was used for proton decoupling The sequential assignment was performed using CCPNMR 2.4.2

To investigate the salt bridges in SAA fibrils, z-filtered TEDOR with mixing times of 1.9 ms and 10 ms were recorded with spinning at 16650 Hz MAS in a 750 Hz magnet. The magnetization was transferred from ^{1}H to ^{13}C using ramp CP followed by rotor synchronized π-pulses to reintroduce ^{13}C-^{15}N dipolar couplings.

Experiments to determine dynamic region

The dynamic region of SAA fibrils was explored using ^{1}H-^{15}N and ^{1}H-^{13}C INEPT experiments. The refocused INEPT-based HSQC with MISSISSIPPI was recorded with decoupling during acquisition at a spinning speed of 16650 Hz. The resonances were

ambiguously identified using the random coil chemical shift and predictions from CCPNMR 2.4.2. However, the sequential assignment was not performed because of low S/N.

Molecular Dynamic Simulation

The conformational dynamics of SAA fibrils were studied by MD simulations on the PDB 6dso and PDB 6zch morphologies. The group of Dr. Nadine Schwierz performed the simulations. Two additional models were created with an alternative interface based on morphology 6zch. Model 1 is based on 6zch, where the interface is formed between K29-E25, and model 2, derived from 6zch, has an interface formed by E25-K24-D22-G1-E55-K56-D59-R61. The MD simulations were performed with a box length of 156.89 A^o and 166.60 A^o for fibrils with two or three stacks, respectively. It was performed at fixed particle number (N), pressure (P), and temperature (T) using the Gromacs simulation package (version 2018) [168, 169]. The force field parameters for peptides were obtained from Amber99sb-star-ildn [170], TIP4P-Ew [171] for water, and Mamatkulov Schwierz for NaCl [172]. The periodic treatment of Coulombic interactions was achieved by applying periodic boundary conditions and the particle-mesh Ewald method. The system equilibrium was achieved by the steepest descent algorithm. The systems were equilibrated first in a canonical ensemble with a fixed number of particles N, volume V, and temperature T (NVT ensemble) and then in an isothermal-isobaric ensemble with a fixed number of particles N, pressure P, and temperature T (NPT ensemble) for 1 ns. A 100 ns simulation for each model was performed for the production run by velocity rescaling thermostat with the stochastic term, with a time constant of τ_T = 0.1s^{-1} of and Parinello – Rahman pressure coupling with a time constant of τ_p = 5s^{-1}. The root mean square fluctuation (RMSF) and root mean square deviation (RMSD) were calculated from last 50 ns of the simulation with the average structure and the experimental structure (6ds0), respectively, as a reference. Coordinates were written every 40 ps.

4. Result

4.1 Characterization of mSAA and investigation of SAA fibril structure using solid state NMR

4.1.1 The biophysical analysis of mSAA 1.1:

The SAA belongs to the family of apolipoprotein. It remains bound to HDL or other lipids in the tissue. The free SAA is unstable and precipitates at room temperature and high salt concentration. Several pH and temperatures were screened to identify the condition stabilizing the protein. The stability and conformation of SAA were investigated by Circular Dichroism Spectroscopy (CD). The CD spectrum of SAA in 20 mM Tris buffer at pH 8.5 and 4^{o}C shows minima at 222 mdeg and other minima at around 208 mdeg, as shown in figure 16 C. These minima are the signature of an alpha-helical secondary conformation of the protein. Hence, it can be concluded that SAA adopts an alpha-helical conformation at a lower temperature and basic pH. The results concur with the structure of SAA given by X-ray crystallography [117]. The spectra at neutral and acidic pH do not have a well-defined minimum at 222 mdeg, and CD spectra look like a mixture of α-helical and random coil conformation, as shown in figure 16A and B.

16 A. SAA in pH 5

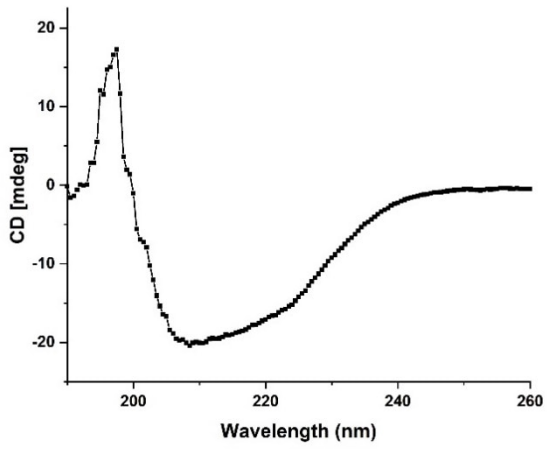

B. SAA in pH 7

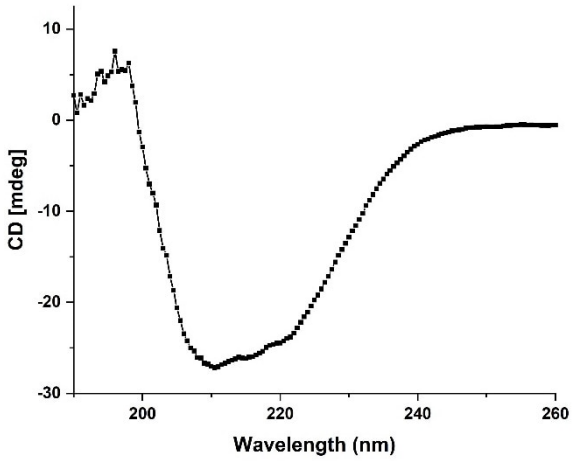

The results were confirmed with the ^{1}H-^{15}N HSQC spectrum by NMR. Every peak in a ^{1}H-^{15}N HSQC correlation spectroscopy corresponds to an amino acid in the protein sequence (except proline). The spread of peaks in the HSQC spectrum suggests whether a protein is folded, unfolded, or aggregated. As depicted in figure 17 C, the peaks in ^{1}H-^{15}N correlation spectra (HSQC) for SAA in 20 mM tris at pH 8.5 spread from 6.5 to 10.5 ppm, verifying that SAA is folded. In contrast, spectra at pH 4.4 and 7 have peaks from 6.5 to 8 ppm,

suggesting either unfolded protein or aggregation. Since the spectra of SAA change with the pH of the buffer, the SAA can be categorized as an intrinsically disordered protein (IDP).

C. SAA at pH 8.5

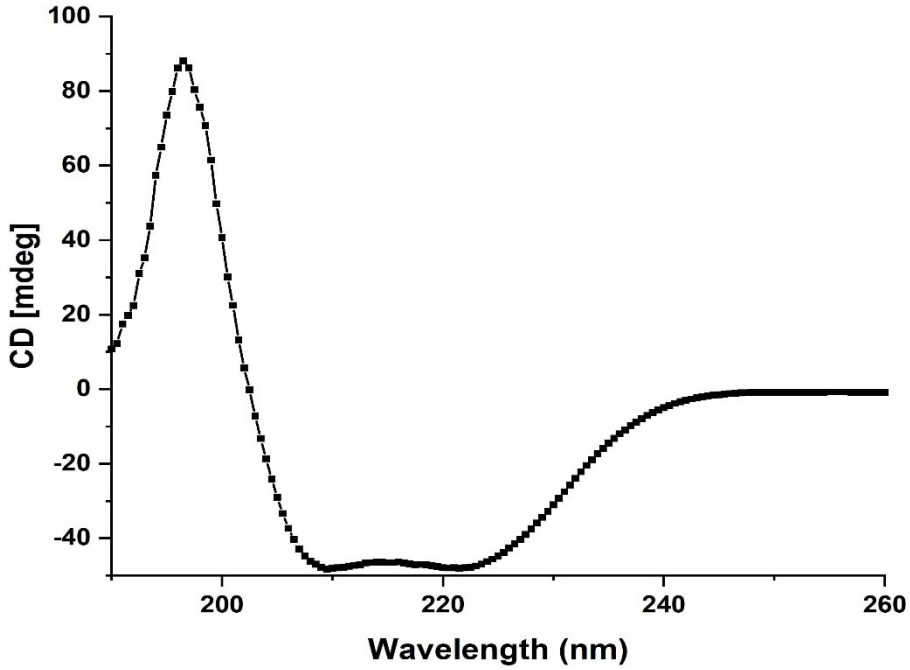

Figure 16. CD spectra of SAA at 4ºC and different pH. *(A) SAA in acetic acid at pH 5, (B) SAA in phosphate buffer at pH 7, and (C) SAA in tris buffer at pH 8.5*

17 A. SAA in acetate buffer (pH 5)

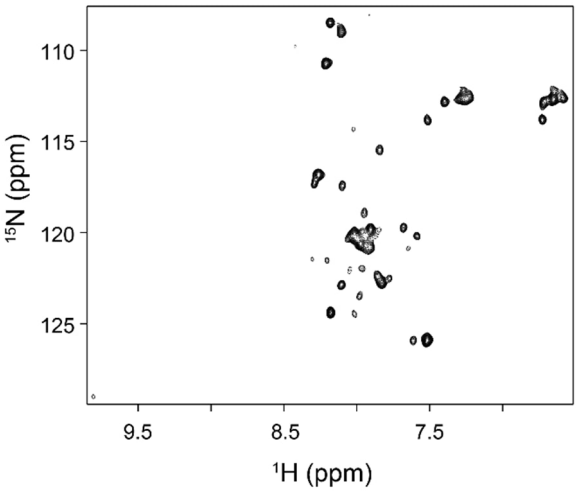

B. SAA in phosphate buffer (pH 7)

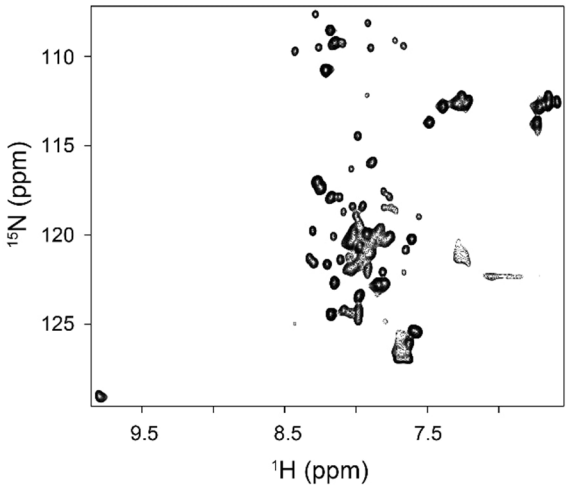

Further, the stability of SAA was investigated with the temperature screen and the thermal melting curve. As shown in figure 18 A, the SAA has an α-helical curve at 4ºC, transforming into a random coil curve at 37ºC (figure 18 B). It has been noticed that the intensity of the CD signal decreases, which depicts the instability and aggregation of the SAA. The thermal melting curve in figure 18 C shows that SAA has a Tm (the temperature where 50%

population of the protein unfolds) of approx. 18ºC. It can be inferred that SAA remains stable only at lower temperatures. With higher temperatures, the unfolding of free SAA starts leading to fibril formation.

C. SAA in tris buffer (pH 8.5)

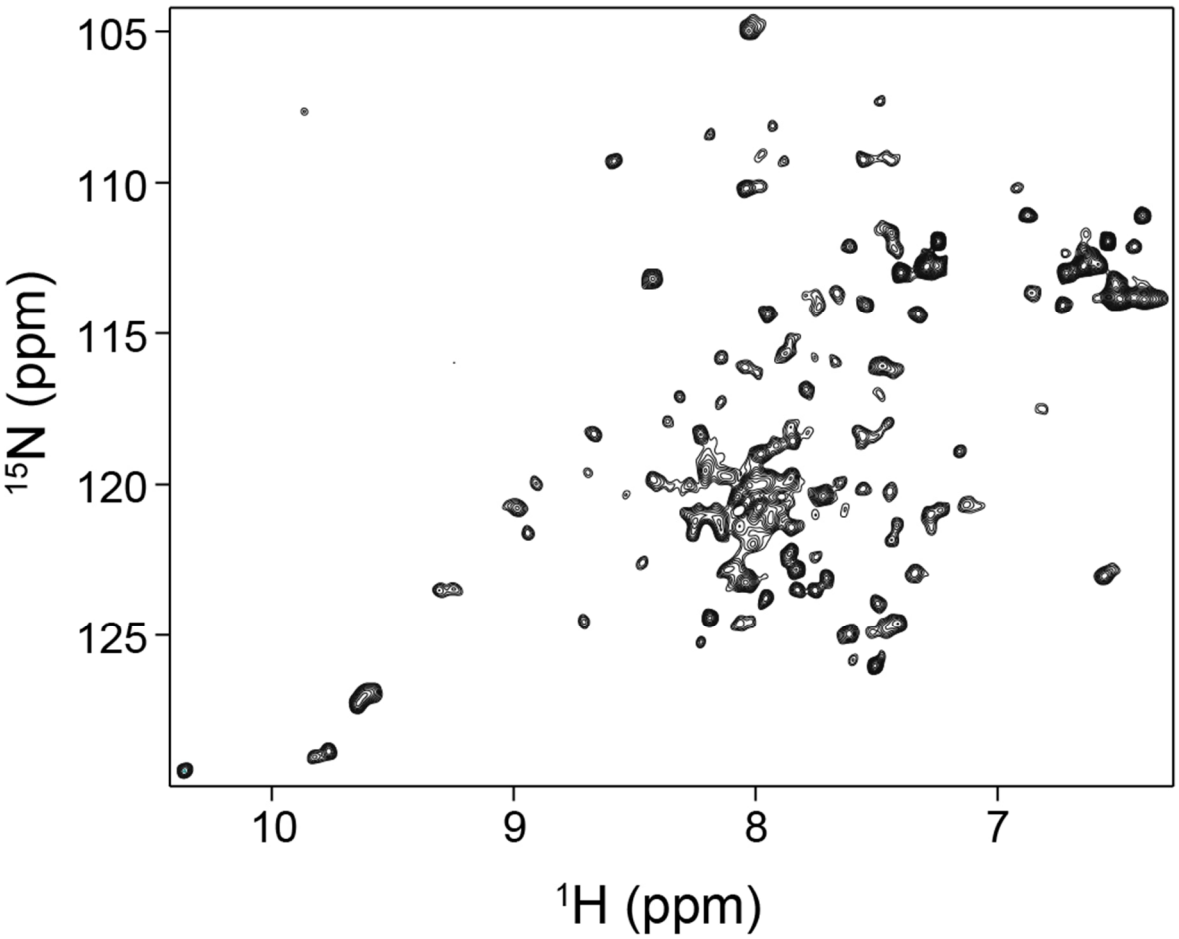

Figure 17. ^{1}H-^{15}N correlation NMR spectra of SAA at 4ºC and different pH. *(A) SAA in acetic acid at pH 5, (B) SAA in phosphate buffer at pH 7, and (C) SAA in tris buffer at pH 8.5*

18 A. SAA at 4ºC

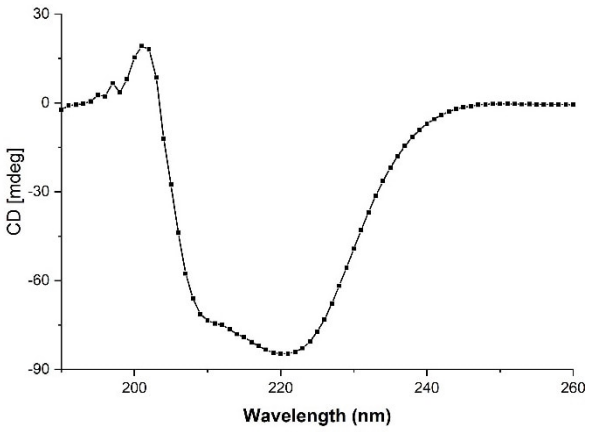

B. SAA at 37ºC

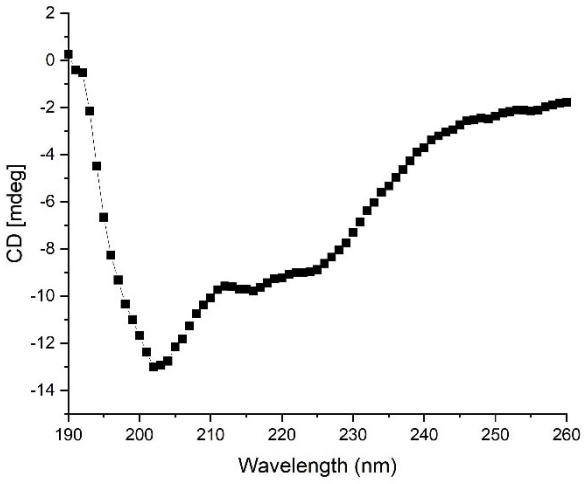

C. Melting temperature of SAA

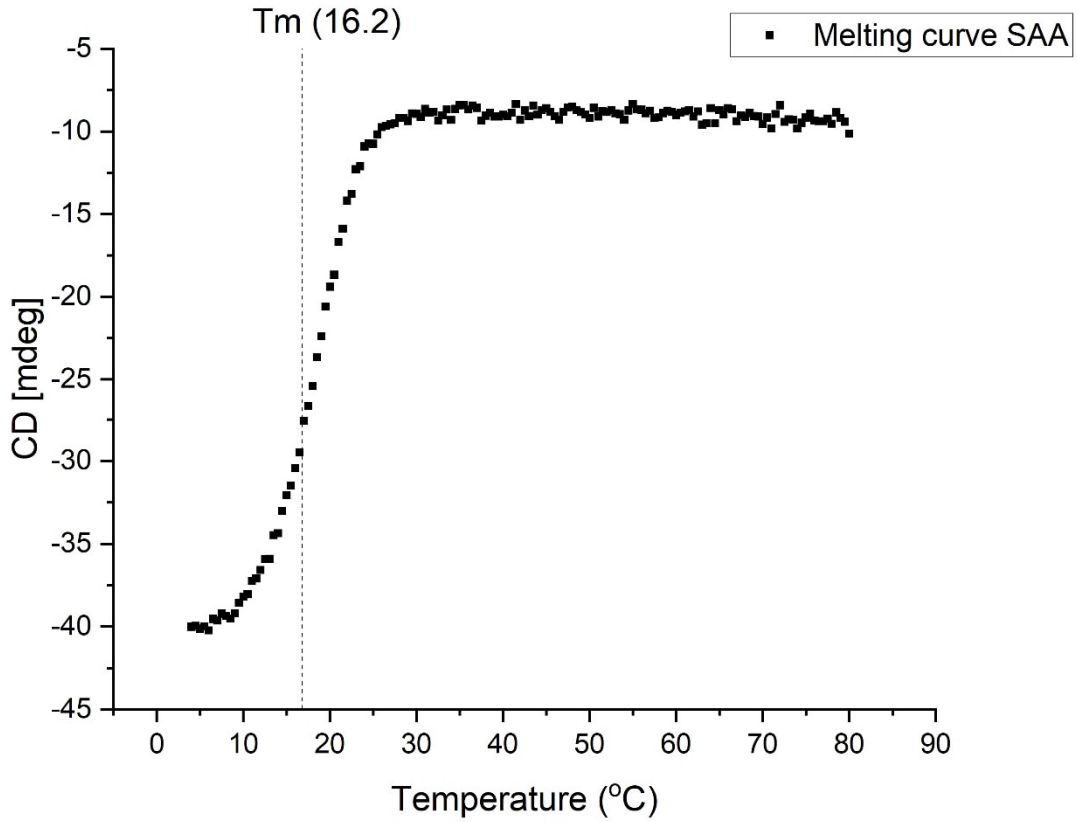

Figure 18. CD spectra of SAA in 20 mM tris at pH 8.5 *(A) SAA at 4°C, (B) SAA at 37°C (c) the temperature scan of SAA using CD spectroscopy from 0°C to 100°C to determine melting temperature.*

The effect of temperature on SAA was also confirmed using NMR. The ^{1}H-^{15}N correlation (HSQC) was recorded at 4°C, depicting a folded protein with the spread of peaks from 6.5 to 10.5 ppm, figure 19 A. The three tryptophans are visible as three distinct peaks. The peaks in HSQC dramatically collapse to a range of 6.8 to 8.5 ppm (figure 19 B), which infers aggregation. Also, only one tryptophan is visible at 37°C. The results clearly state that with the increase in temperature, SAA unfolds and transits to aggregation.

19 A. SAA at 4°C B. SAA at 37°C

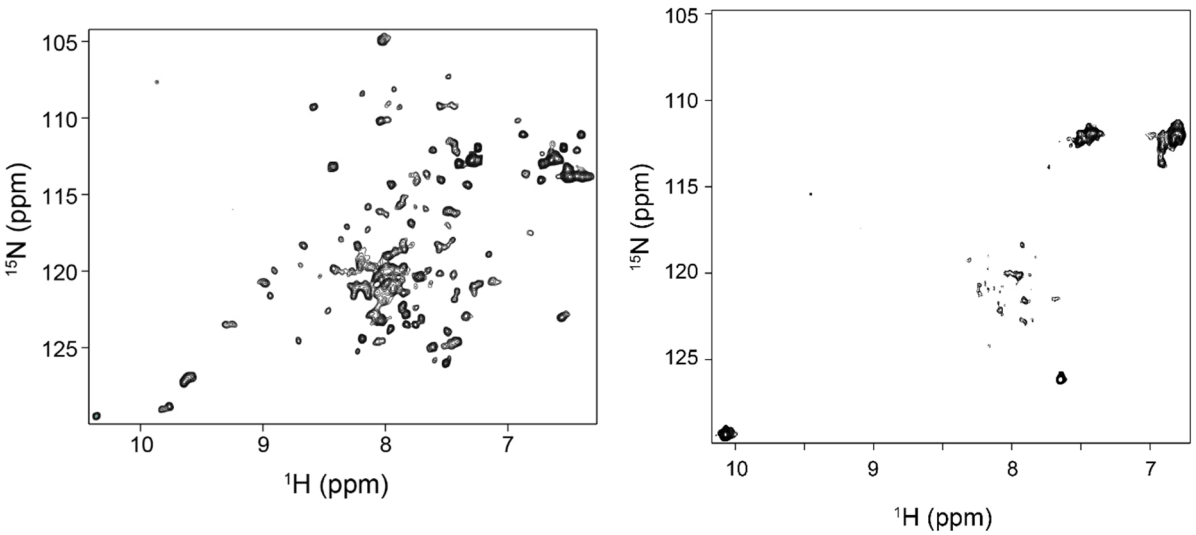

Figure 19. ^{1}H-^{15}N correlation NMR spectra of SAA in 20 mM tris at pH 8.5 at different temperatures. *(A) SAA at 4°C (B) SAA at 37°C.*

4.1.2 SAA structural transformation characterization by CD and Fluorescence spectroscopy

The structural and morphological transformation of SAA were investigated by time-dependent CD and fluorescence spectroscopy. The SAA was allowed to aggregate at 37°C at the rotation of 120 rpm. The sample was taken after every 30 minutes. The CD and fluorescence spectra were recorded at 4°C for the 50 µM sample and 37°C for the 10 µM sample, respectively. The SAA is α-helical at the initial time point. It transforms to the random coil and further attains β-sheet conformation with time, as shown in figure 20 A. Any structural intermediate was not observed in the process. This implies that the amyloidosis process only includes protein unfolding and aggregation of the unfolded protein to β-sheet rich fibrils. The other possibility could be the formation of short-lived structured intermediates, which could not be visualized with the above-described process. However, it is evident that high temperature leads to the unfolding of the free SAA and causes fibril formation. A similar approach could happen in an acute phase condition, where SAA cannot bind to its lipid partner and form aggregates at high concentrations.

The transformation of an unfolded protein to fibrils is studied by Fluorescence spectroscopy. The tryptophan fluorescence is exploited in the process, which changes with respect to the tryptophan environment after excitation at 295 nm. The SAA is unfolded at 37°C, as shown in figure 20 B. The fluorescence spectrum was recorded at the same temperature at the initial time point. Therefore, the maximum intensity of emitted fluorescence was observed at time point zero. With time, the intensity of fluorescence decreases which implicates the

formation of structured entities. The fluorescence spectra correspond well with the CD spectroscopy and prove that SAA undergoes unfolding and then forms stable β-sheet rich fibrils. In addition to the decrease in intensity, the emission maxima have shown a redshift in the fluorescence spectra. In an unfolded SAA, the amino acids are accessible to the buffer; therefore, all the amino acids are in a polar environment. With the formation of fibrils, the non-polar amino acids interact with each other and stabilize the structure with hydrophobic forces. Therefore, Tryptophan experience a hydrophobic interaction which causes a redshift in the fluorescence spectra. The redshift implies that strong hydrophobic interactions are responsible for stabilizing the structure of fibrils.

20 A. B.

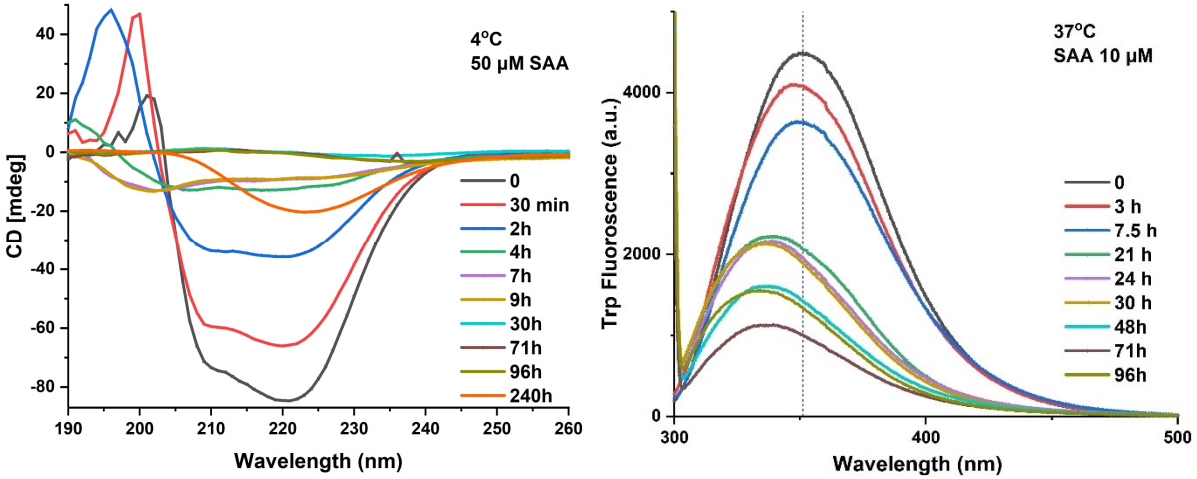

Figure 20. Unfolding and aggregation kinetics of SAA using CD and fluorescence spectroscopy. *(A) The kinetics of SAA using CD spectroscopy with time at room temperature (the measurements were performed at 4°C). (B) the shift of λ_{max} with time for SAA in fluorescence spectroscopy (the measurements were performed at 37°C).*

4.1.3 Kinetic study of fibril formation

The kinetics of fibril formation was studied using ThT assay. As described before (Section 2.2.4.6), thioflavin T (ThT) dye does not bind to the monomeric protein but to the fibrillar aggregates. As shown in figure 21 A, the ThT curve of SAA has three distinct growth phases. An initial lag phase of approximately 15 hours was observed, which describes the nucleation process. The lag phase is followed by a fast exponential growth phase where the fibril grows. Finally, the curve attains a saturation phase where fibrils are in equilibrium with fibril formation and fragmentation.

The kinetics study was also performed at different concentrations. The ThT curve is similar for all the concentrations of SAA. The lag phase decreases with the increase in concentration. The lag phase reduces from 15 hours for 50 µM to approximately 2 hours for

100 µM. However, it does not reduce to zero. Therefore, even at high concentrations, the protein requires some time to form nuclei, leading to fibril formation. Additionally, the intensity of ThT fluorescence at the plateau increases with the concentration of protein. It can be inferred that the amount of fibrils formed is a factor of the initial concentration. The SAA will form amyloids faster and in higher amounts with increased concentration of SAA.

Further, the effect of seeding was investigated on the kinetics of amyloidosis. The seeds provide initial nuclei for the fibril formation; therefore, they should enhance the kinetics of amyloidosis. As ascertained from the spectra, the seeding does abolish the lag phase. Both 5% and 10% of the w/w seeding process do not have a lag phase in the ThT kinetic curve. Additionally, the fluorescence intensity increases with the addition of a higher amount of seeds, although the initial protein concentration is the same in all the conditions. Hence, it implies that the protein can utilize the preformed fibrils as the nuclei and directly lead to the growth phase. Since the nuclei are provided to the monomeric protein, the formed fibrils should be structurally similar to the seeds The property of using preformed fibrils as seeds was employed in many instances to prepare a homogenous and high-quality sample.

21 A. B.

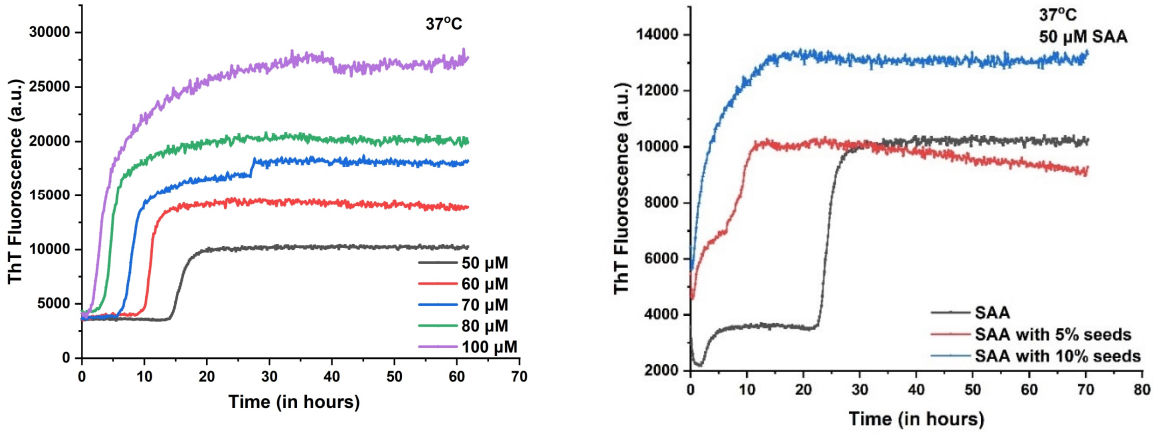

Figure 21. Kinetics of SAA aggregation determined using ThT assay. *(A) The kinetics of SAA aggregation at different concentration of SAA. The lag phase reduces with the concentration. (B) The kinetics of SAA aggregation in the presence of seeds.*

4.1.4 Characterizing the morphology of SAA fibril

The seeding was employed to prepare a homogenous and high-quality solid-state NMR sample, which could be further assigned and investigated. The prepared fibrils were visualized using Transmission Electron Microscopy (TEM). With TEM, it is possible to anticipate fibrils' morphology, including the diameter and turns. As shown in figure 22, the SAA forms highly homogenous thin fibrils. The fibrils are small and do not have any twists

and turns. Additionally, the diameter of fibrils is approx.15 nm, which implies that fibril consists of two protofilaments. The UV-absorbance of the buffer was dropped from 0.58 mg/ml to 0.013 mg/ml, which infers that the monomeric protein completely transformed into fibrils. The fibrils in the TEM images have only one morphology, verifying that seeding was successful.

22 A. B.

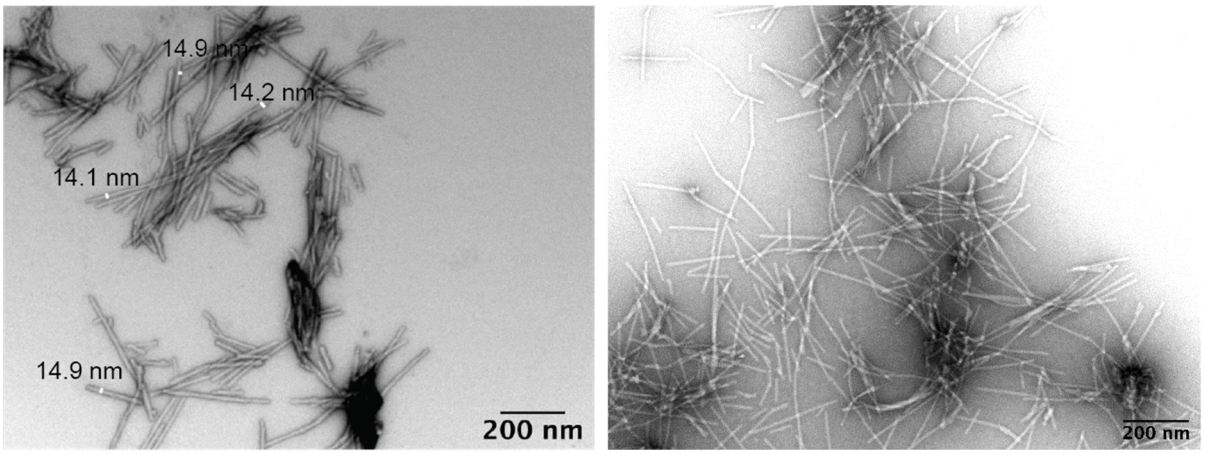

Figure 22. TEM images of seeded fibrils *(A) and (B) The TEM images of SAA fibrils prepared with 5% seeds. The sample was later utilized for solid-state NMR investigation.*

4.1.5 Solid-state NMR assignment of SAA fibrils

As described in the materials and method, the SAA fibrils were prepared and packed in a 1.9 mm rotor using an ultracentrifuge. The pellet of the fibrils was off-white, and the rotor was filled with fibrils. Sodium trimethylsilyl propane sulfonate (DSS) was added as a calibration standard to standardize the chemical shifts. The signal of DSS was calibrated to zero.

Two samples of SAA fibrils were prepared with identical protocols and conditions to confirm the reproducibility. As seen in figure 23 A, the spectra overlay entirely over each other. Some peaks are missing in the blue spectra since the rotor was not completely filled with the sample. Therefore, the blue spectra have less number of peaks, but all the peaks are visible at lower contour levels. It could also be the possible reason for the broadening of peaks in the blue spectra. However, all the carbon resonances for prominent peaks like Serine, Threonine, and Isoleucine, superimpose very well in both spectra. It verifies that at similar conditions and with seeds, SAA forms reproducible fibrils. Hence, the fibril sample was prepared with the above-mentioned procedure with 5% w/w seeds.

Not only the aliphatic region of spectra but also the aromatic region of spectra overlap entirely. All the peaks for tyrosine and tryptophan are present in both spectra at the same position.

23 A.

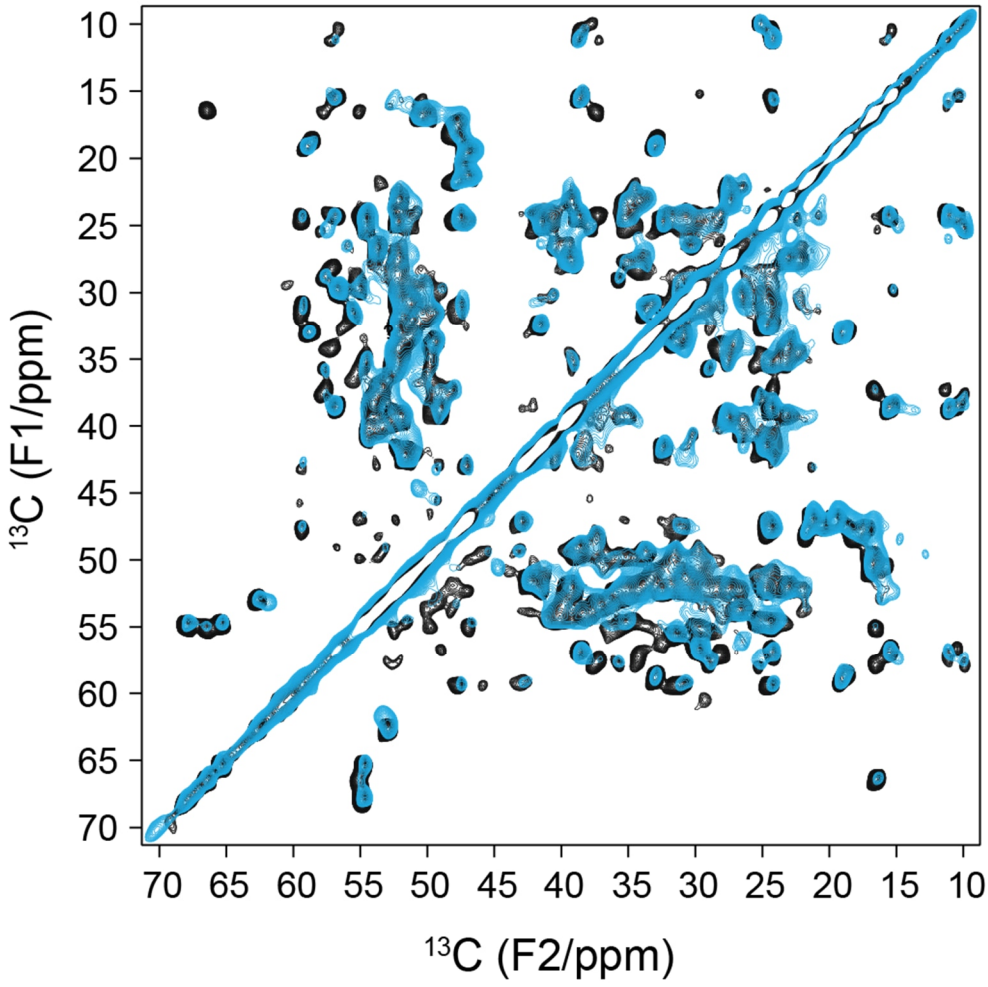

B.

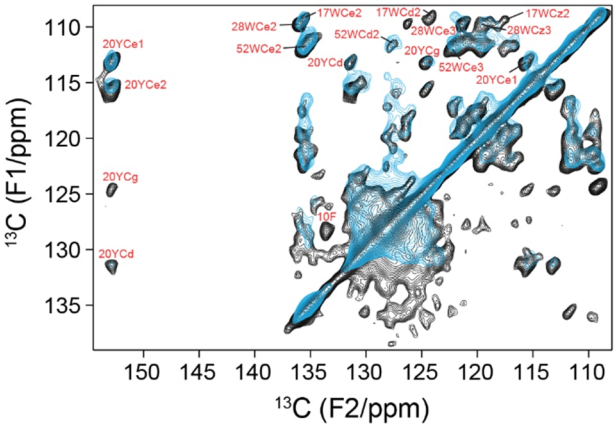

C.

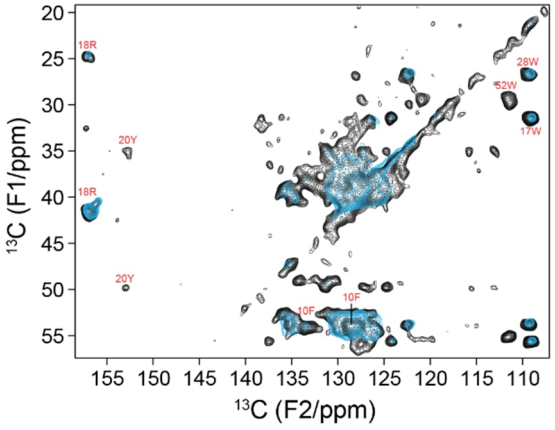

Figure 23. ^{13}C-^{13}C DARR correlation of SAA fibrils prepared with seeds *(A) Overlay of ^{13}C-^{13}C DARR correlation of SAA fibrils prepared with same protocol. (B) and (C) Overlay of the aromatic region of the two fibril samples*

In addition to being reproducible, the SAA fibril sample is also homogenous. The peak for a particular residue in the spectra does not show any multiple peaks. For instance, there are two isoleucines in the sequence of SAA. Only two sets of corresponding peaks are visible.

Similar results are observed for serine, threonine, and valine peaks, where the set of peaks corresponds with the number of residues, and no multiplets of peaks are visible. Hence, a high-quality, non-polymorphic SAA fibril sample was successfully prepared using seeding.

The homogenous sample of SAA was employed for the assignment experiments. The two-dimension ^{13}C-^{13}C correlation (DARR) spectra and ^{13}C-^{15}N correlation (NCA) spectra were recorded to detect the amino acids that constitute the fibrils' structural part. There are around 56 peaks visible in the NCA spectra. Every peak in an NCA spectrum corresponds to an amino acid in the protein sequence. Since only 56 peaks are visible, it implies that only half of the protein makes the structured part of the fibril and constitutes the core. While the other half of the protein either remains flexible in the fibril or disrupts during the process of fibril formation. The DARR was used to tentatively assign the residues and count them according to their peculiar chemical shifts. The amino acids like isoleucine, serine, threonine, valine, and alanine have distinct chemical shifts used to estimate the residues available in the spectra.

24 A.

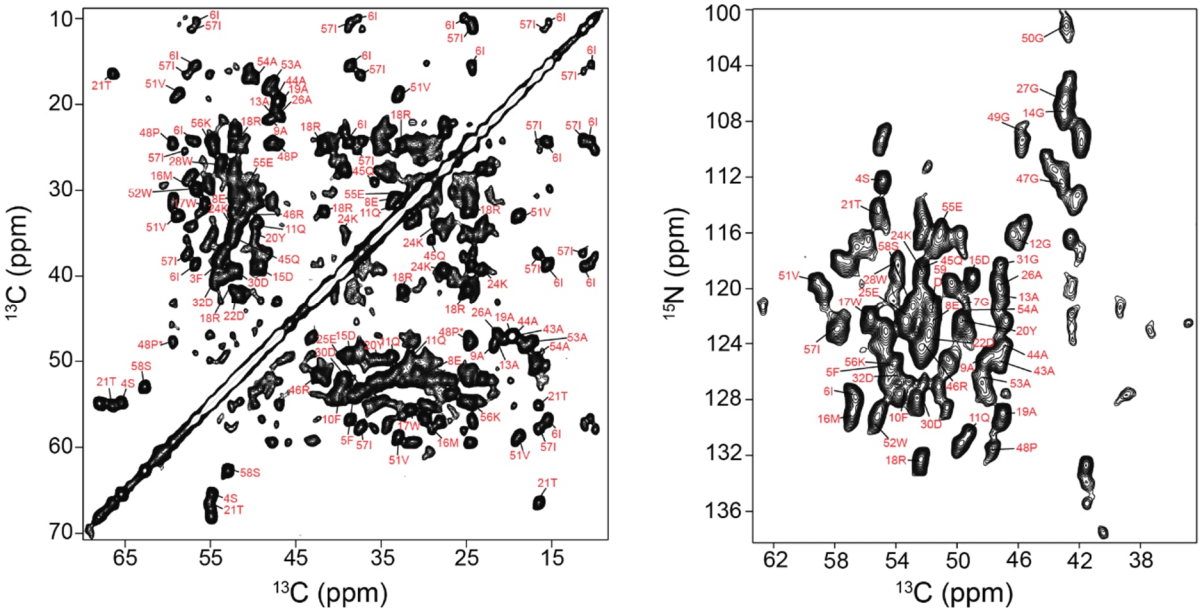

The SAA fibrils also have a well-defined, high-resolution region for the aromatic region. The distinct peaks for tryptophan, phenylalanine, and tyrosine are well resolved. The carbon atoms of tryptophan and tyrosine can be easily assigned with their well-defined peaks. However, the phenylalanine peaks are broad and cannot be counted. The arginine Cγ peak is also well-defined and can be labeled. The three distinct peaks of Cγ of tryptophan confirm that all the tryptophans are in the structured core of the fibril, figure 24 B. The peaks from tyrosine carbon atoms show the most exciting feature. Though peaks for only one Tyrosine

are visible, however, peaks for both Cε1 and Cε2 are visible, as shown in figure 24 C. The Cε1 and Cε2 of Tyrosine are only visible in a static tyrosine ring. If the aromatic ring of Tyrosine is dynamic, then only one peak is visible. The result implies that the aromatic ring of Tyrosine is static and should be involved in interaction responsible for stabilizing the fibril structure. The high-quality and well-resolved aromatic region of SAA fibrils depicts strong hydrophobic interaction in stabilizing the core structure of fibrils. Similarly, highly resolved Cγ for the charged residues, like aspartate, glutamate, arginine, and lysine, proves ionic residues' interaction to form salt bridges and stabilize the fibrils. Hence, it can be postulated that SAA fibrils have strong hydrophobic interactions and salt bridges that maintain SAA seeded fibrils' well-defined structure.

Furthermore, the SAA was sequentially assigned using three-dimensional experiments – NCACX, NCOCX, and CONCA. The NCACX gave the chemical shift of i^{th} residue, which is traced to the CONCA spectrum. The peak in the NCOCX that corresponds to the CONCA spectrum gives the chemical shift of the $i\text{-}1^{th}$ residue. The spectra were of high quality, and SAA fibrils were successfully sequentially assigned. Out of 56 visible peaks from NCA, 46 peaks were sequentially assigned. The residues at the beginning of the N-terminal are not assigned. The assignment starts from the 3rd amino acid, i.e., phenylalanine (3F), and is sequentially assigned till the 22nd aspartate (22D). The second stretch of assignment is from 24th lysine to 28th tryptophan, followed by 30th aspartate to 32nd aspartate.

C. D.

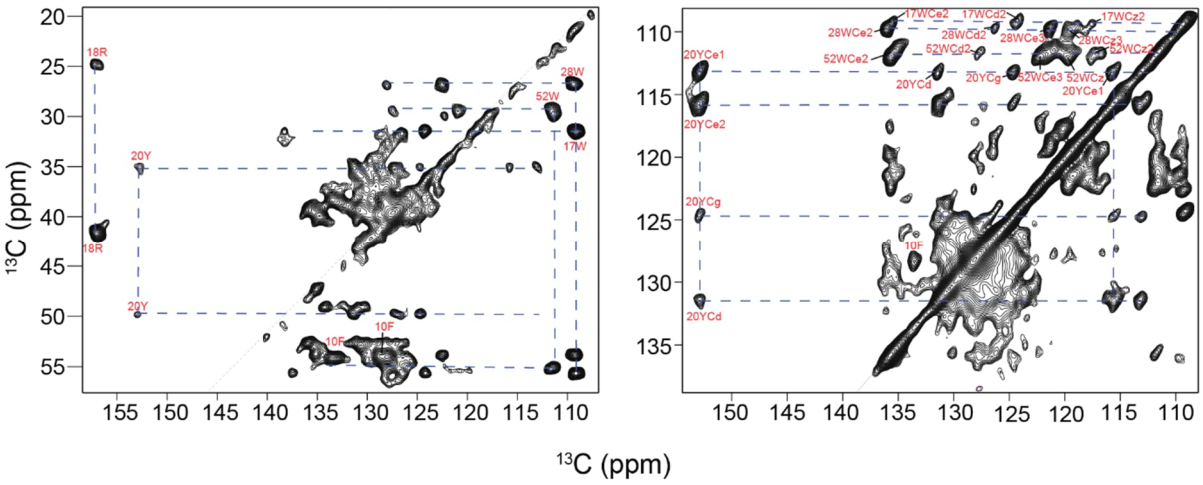

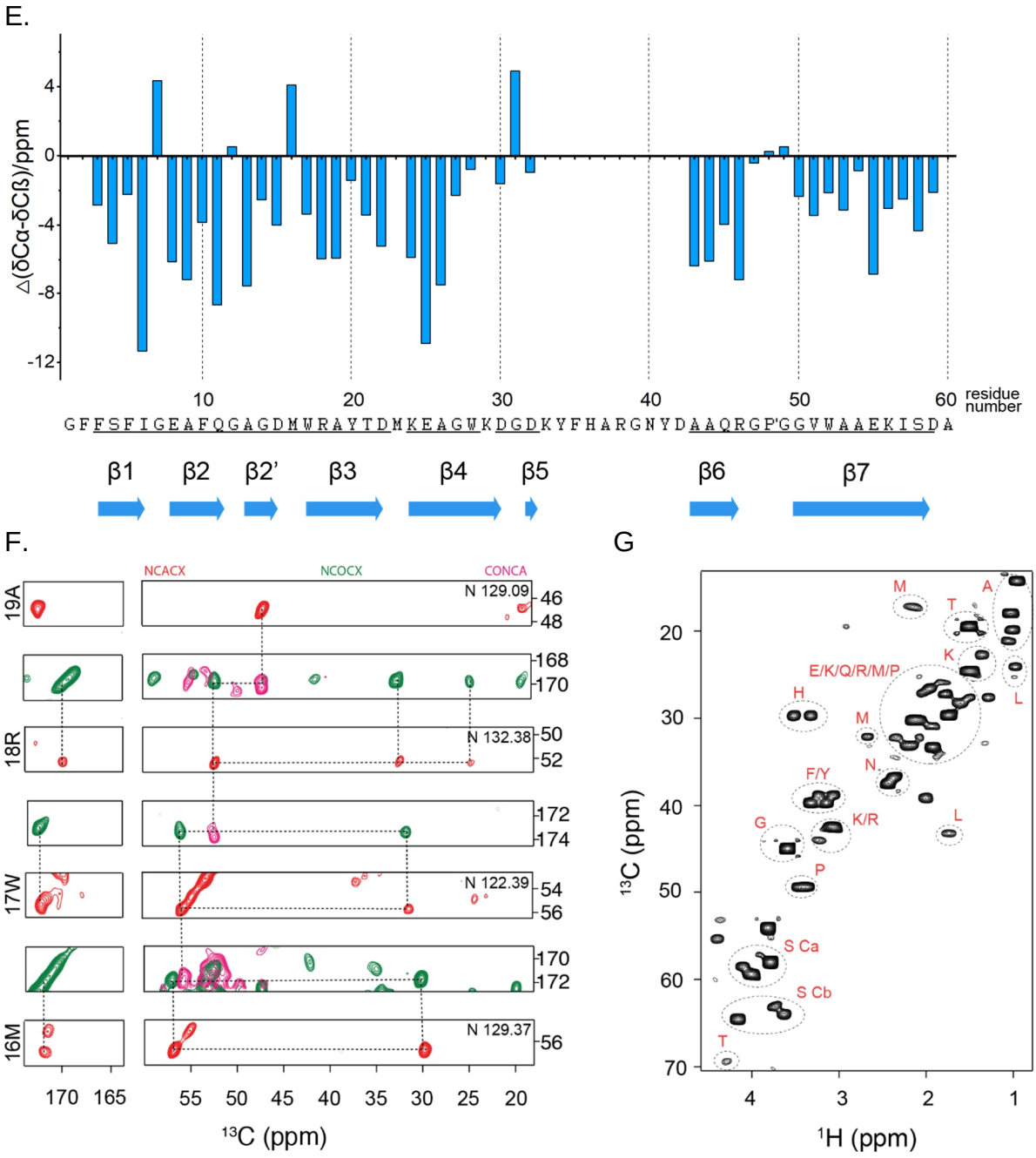

The amino acids from 33rd lysine to 42nd aspartate were not sequentially assigned. However, the residues from 44th alanine to 59th aspartate were also assigned. It is the last stretch of amino acids in the SAA protein sequence, which was sequentially assigned. After the 59th aspartate in the sequence, the residues were not visible in any spectra. It implies that the C-terminal of SAA and residues 33-42 are dynamic and do not have a well-defined structure.

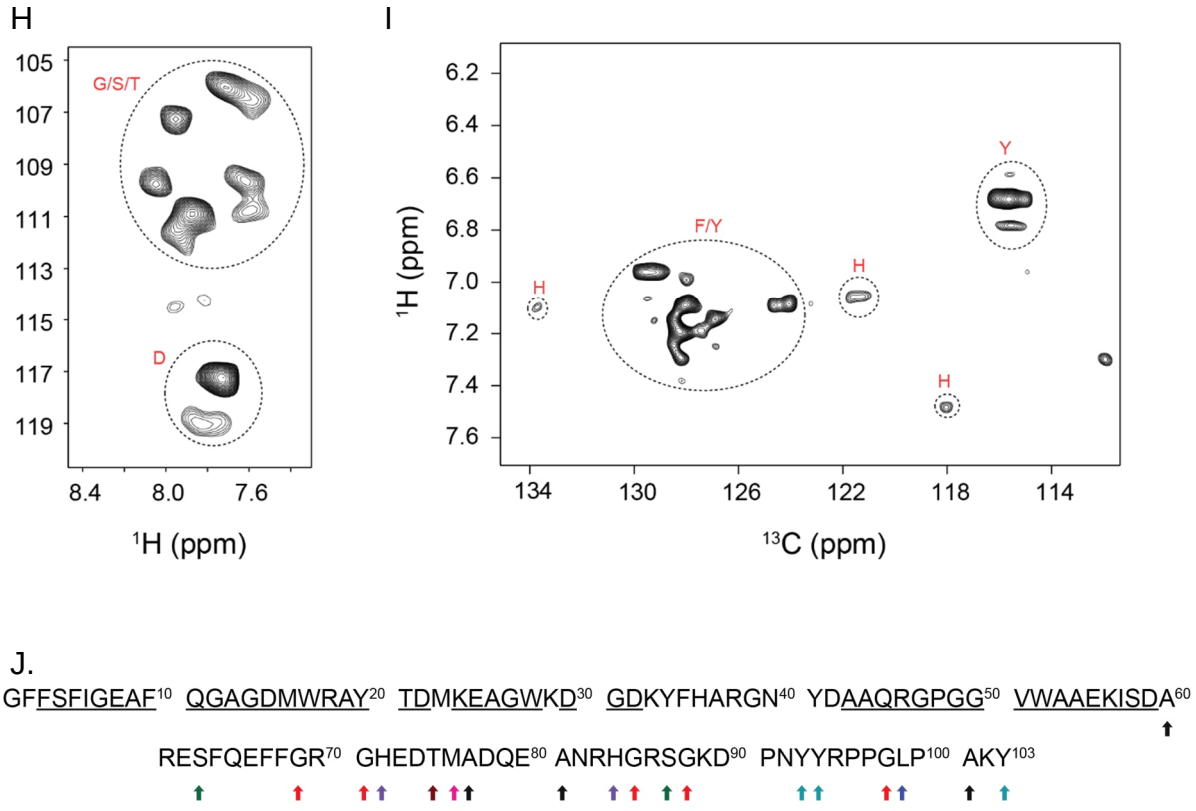

Figure 24. *Solid state NMR characterization of seeded SAA fibrils(A), (B) Assigned residues of SAA fibrils in ^{13}C-^{13}C and ^{13}C-^{15}N correlation spectra, respectively. (C), (D) the aromatic residues observed for SAA seeded fibrils in ^{13}C-^{13}C correlation spectra. (E) Secondary chemical shifts and β-sheet propensity for SAA fibrils obtained from solid-state NMR. (F) Strip plot for sequential assignment for SAA assignment using 3D experiments like NCACX, NCOCX, and CONCA. (G), (H), (I) the flexible residues observed in ^{1}H,^{13}C and ^{1}H,^{15}N INEPT spectra. (J) The dynamic residues observed in INEPT spectra are highlighted with arrow.*

The positions of β-sheets in the fibrils were calculated using the chemical shift index (CSI). The chemical shift index predicts the position of the β-sheet from the difference of observed chemical shift of a residue to the random coil. If the value is negative, then it is a part of the β-sheet. A positive value infers α-helix, and the random coil is depicted by zero. As shown in figure 24 E, the seeded SAA fibrils are composed of seven β-sheets. The positions of β-sheets are β1 (4→6), β2 (8→11), β2' (13→15), β3 (16→22), β4 (24→30), β6 (44→46), and β7 (50-59), respectively.

The role of the C-terminal of the SAA protein in the process of fibrillation is unknown. It has been proven that the aggregation kinetics accelerates without a C-terminal. It was also proposed that SAA undergoes a proteolysis step where C-terminal is cleaved and leads to aggregation. The seeded fibrils of SAA were prepared with the entire length of SAA without cleaving the C-terminal. The ^{1}H-^{13}C and ^{1}H-^{15}N correlation spectra by insensitive nuclei enhanced by polarization transfer (INEPT) were recorded to investigate the flexible regions of the SAA.

There are seven peaks in the ^{1}H-^{15}N correlation spectrum at the glycine, serine, and threonine region. The peaks correspond precisely with the five glycines, two serines, and one threonine at the C-terminal. The number of peaks verifies that the C-terminal remains attached to the fibrils but is dynamic. The ^{1}H-^{13}C correlation spectra further demonstrate similar results as the ^{1}H-^{15}N spectrum. Only one visible methionine peak corresponds to single methionine in the C-terminal. The peak for one leucine, two serines, and one threonine are also visible. However, the assignment experiments for the flexible region using INEPT were not possible because of the low signal-to-noise ratio. Therefore, only a tentative assignment using the chemical shift of a random coil was possible. Nevertheless, the number of amino acids with distinct chemical shifts were estimated and then compared with the residues in the C-terminal. The aromatic amino acids and Histidine have protons around 7 ppm which correlate with carbons in the aromatic rings. The C-terminal constitutes three tyrosine, three phenylalanine, and two Histidine which have a chemical shift of protons around 7-8 ppm and carbons in the range of 110-140 pm. There are seven peaks visible in the region, corresponding precisely with the chemical shift of tyrosine and tryptophan. However, no peak corresponding to the chemical shift of Histidine was observed.

The results of ^{1}H-^{15}N and ^{1}H-^{13}C correlation spectra prove that the C-terminal remains attached to the fibrils but is not part of the core. The N-terminal of SAA constitutes the core and structural region of the fibrils, while the C-terminal is the dynamic tail of the fibrils. The outcome also verifies that it is not critical for SAA to undergo a proteolysis step to aggregate. The free SAA at higher temperatures can unfold and enter the aggregation process with its C-terminal attached.

4.1.6 Comparative analysis of ssNMR and cryo-EM structure

Hydrophobic forces between the polar amino acids and salt bridges between ionic residues stabilize the structure of amyloid fibrils. The study of these interactions paves the path for modeling the fibril structure. The long-range interactions are investigated by long mixing time DARR and PAR. These spectra provide extra peaks than two-dimensional DARR with 50 ms mixing time, demonstrating the interaction between neighboring residues and the long-range interaction.

25 A.

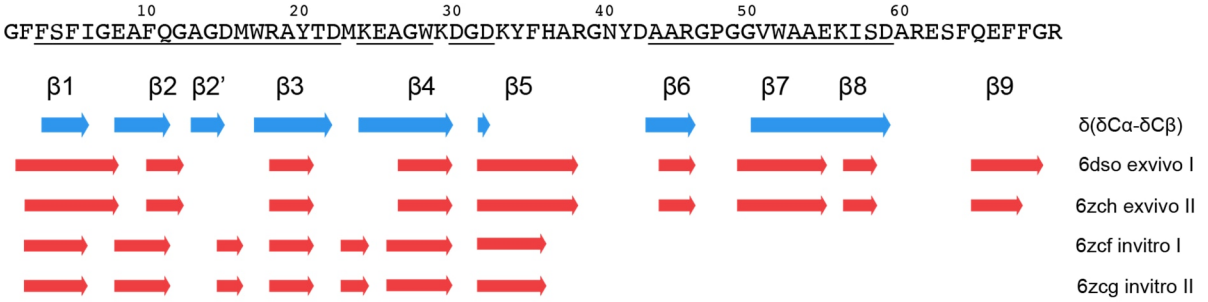

B.

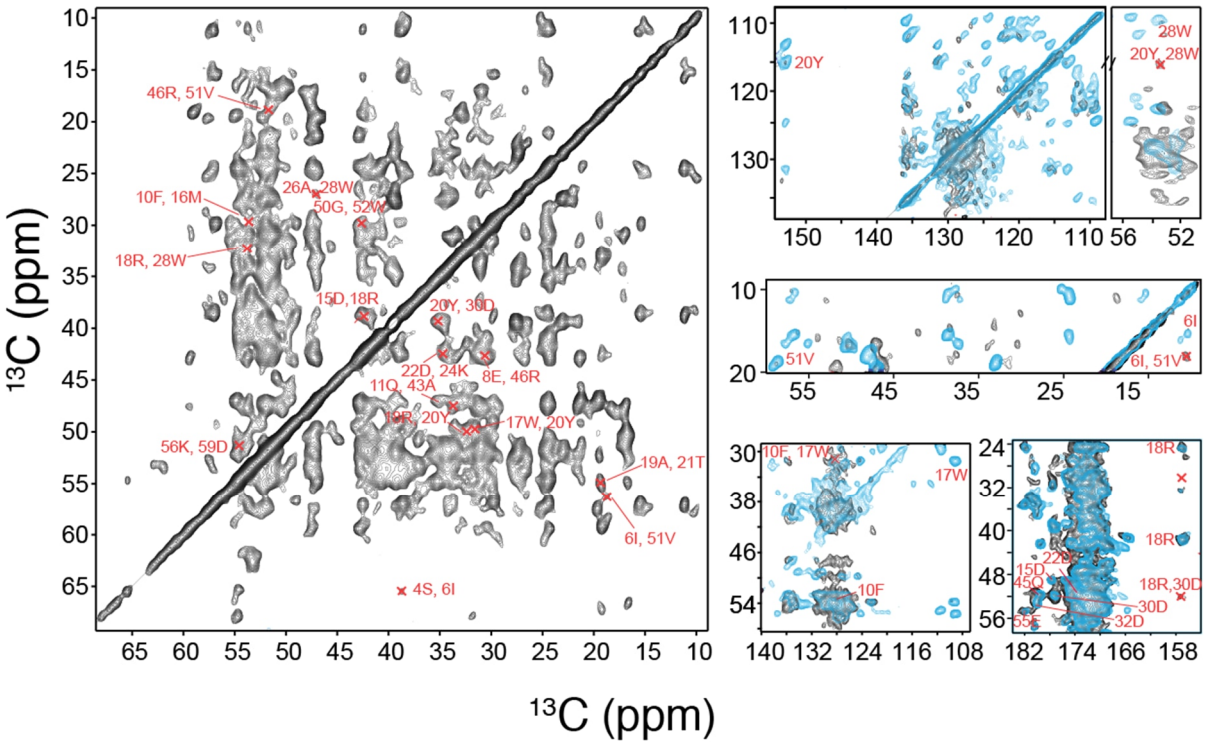

The isoleucine at the 6th position interacts with serine at the 4th position and valine at the 51st position. Similarly, tyrosine at the 20th position interacts with tryptophan at the 28th position and aspartate at the 30th position. Phenylalanine at the 10th position interacts with methionine at the 16th position and tryptophan at the 17th position. There is a peak depicting the interaction of arginine at the 18th position with aspartate at the 30th position and tryptophan at the 28th position. The other main long-range interactions are - 19A → 21T, 8E → 46R, 22D → 24K, 11Q → 43A, 26A → 28W, 15D → 18R, 46R → 51V, 50G → 52W, and 56K → 59D.

C.

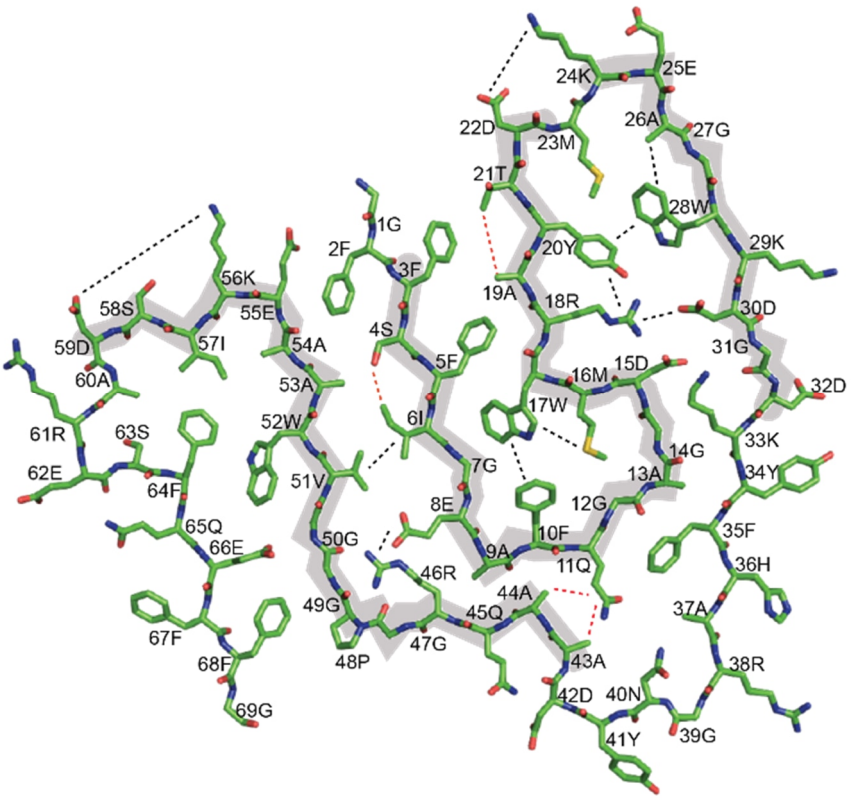

D.

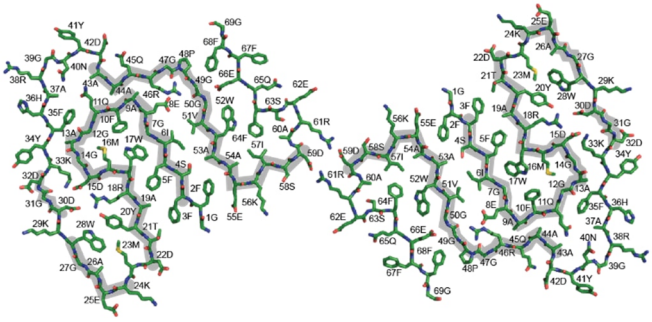

E.

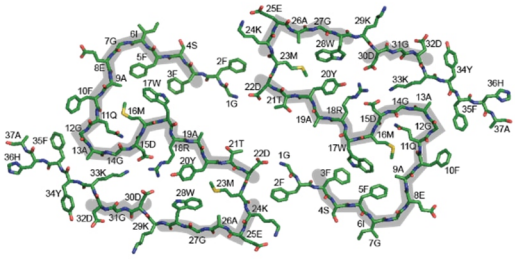

The long-range interaction of isoleucine at the 6th position interacts with serine at the 4th position and with 51V, depicting that isoleucine and serine are neighboring interaction partners, and their side chains face the same direction. Additionally, the β-sheet consisting of isoleucine and serine should interact with the β-sheet carrying valine at the 51st position. Similarly, 10F interacts with both 16M and 17W; therefore, side chains of 16M and 17W should face the same direction. A very stable interaction is between 20Y, 28W, 18R, 15D, and 30D. The side chains of all these amino acids should be facing the core. The interaction between 22D and 24K suggests that the side chains are in the same direction and stabilize each other. The interaction between 8E and 46R verifies the interaction between β2 and β6.

Four different morphologies were deduced from cryo-EM studies of murine SAA fibrils. Among these four structures, two structures describe the different morphologies of mSAA fibrils solved by cryo-EM from the fibrils extracted from the mouse (ex-vivo fibrils), while the other two outlines the morphologies of SAA fibrils attain when fibrils are prepared in vitro without any seeds.

F. G.

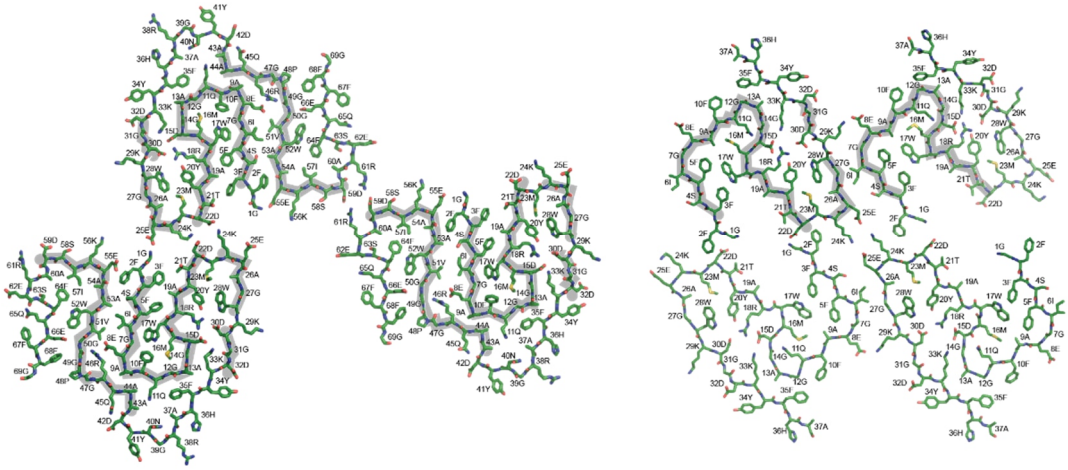

Figure 25. *Comparative analysis of ssNMR observation and cryo-EM structure. A, β-sheets derived from chemical shift index from solid state NMR and β-sheets observed in different fibril morphology investigated by cryo-EM. B, Long range restraints observed in long mixing ^{13}C-^{13}C DARR and 15 ms PAR experiments. C, Overlay of the assignments from ssNMR and long range interactions on the structure of extracted SAA fibrils (PDB ID 6dso). D, E, F, and G Overlay of assignment of ssNMR on fibril morphology with PDB ID 6DSO, 6ZCF, 6ZCH, and 6ZCG, respectively.*

As described by the structures solved by cryo-EM for extracted SAA fibrils adopt two main morphologies. The morphology observed in the highest number of particles, as shown in figure 26D, has two protofilaments. The N-terminal of SAA assembles as the core of fibrils, and the structural part of fibrils constitutes 70 amino acids from the N-terminal. A protofilament in this morphology of SAA fibrils is composed of nine β-sheets. The core starts from the β1, which is stabilized by interactions with β3 and β7. Simultaneously, β3 is sandwiched between β4 and β1, stabilizing the structure with many hydrophobic interactions and salt bridges between ionic residues. The β-sheets, β1, β2, β2, and β7 constitute the core of the fibril, and none of the residues comprising these sheets encounter buffer. In contrast, the other sheets interact buffer with the amino acids in the sequence. The two protofilaments of this morphology are stabilized by the salt bridge between the aspartate at the 59th position and arginine at the 61st position within the two protofilaments.

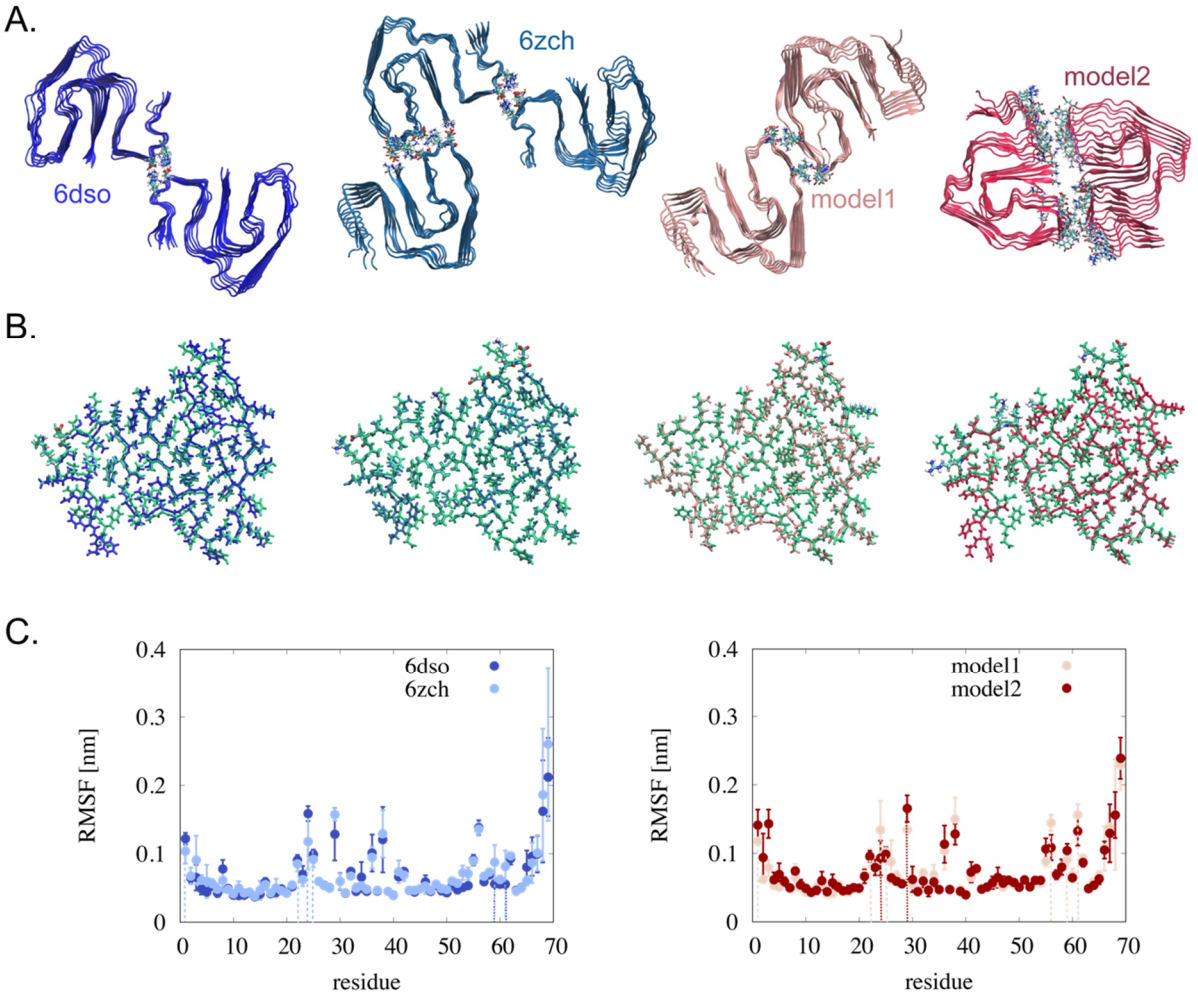

Figure 26. *All-atom molecular dynamics simulation for SAA Fibrils. A, The four models utilised for MD simulations. B, Superposition of one central chain of simulated structures after 100 ns (pink) and the experimental cryo-EM structure 6dso (blue).C, RMSF observed for cryo EM morphology 6dso and 6zch (in blue) and for model with alternate interface (in red). The error bars correspond to standard deviation.*

Another morphology of SAA fibrils extracted from mice was observed in a lower percentage of the particles. The fibrils are composed of three protofilaments, where two protofilaments are stabilized with the same salt bridge between aspartate at the 59th position and arginine at 61st, as observed in previous morphology. At the same time, the middle protofilament interacts with the third protofilament by the salt bridge between lysine at the 24th position to the aspartate at the 22nd position. It comprises nine β-sheets; however, β1 and β9 are smaller than the sheets observed in previous morphology. Nevertheless, the interaction partners and the β-sheets constituting the core remain the same in both morphologies.

The fibrils prepared by SAA *in vitro* without any seeds were also investigated in previous studies by cryo-EM to compare the structure of extracted fibrils with the *in vitro* prepared fibrils. The size of the core is the significant difference in the structure of extracted fibrils from the *in vitro-prepared* non-seeded fibrils. The core of the non-seeded *in vitro*-prepared fibrils

is smaller than the extracted fibrils. Again, two different morphologies were reported for the *in vitro* fibrils, constituting 36 amino acids from the N-terminal. These morphologies comprise seven β-sheets compared to nine β-sheet in the extracted fibrils, and β1 is smaller than its counterpart in the *ex-vivo* fibrils. Also, the β3 and β5 are not present in the extracted fibrils. The number and position of β-sheets in both morphologies are precisely the same. However, the first morphology has two protofilaments constituting the fibrils, while four protofilaments constitute the second morphology. It was also proved in the previous study that *in vitro* fibrils are less stable than the extracted fibrils. It can be the consequence of the absence of a salt bridge stabilizing the protofilaments of the *in vitro* prepared non-seeded fibrils. A salt bridge between lysine at the 24th position of one protofilament and glutamate at the 25th position of another stabilizes the fibril morphology with four protofilaments; however, there is no salt bridge in the fibril morphology with two protofilaments. The study of murine SAA 1.1 using cryo-EM in previous studies proved that SAA fibrils are polymorphic whether extracted or prepared *in vitro.* However, the *in vivo* fibrils are more stable than *in vitro* non-seeded fibrils.

In the current project, the structure deduced by ssNMR for the SAA fibrils prepared *in vitro* with seeds is compared with the different morphologies investigated by cryo-EM. With the ssNMR, 56 residues from the N-terminal have been sequentially assigned. The results implied that seeded *in vitro* prepared fibrils are not similar in structure to *in vitro non-seeded* fibrils. Additionally, the diameter of the fibrils prepared for ssNMR characterization is 8 nm, which confirms that only two protofilaments constitute the fibrils. Therefore, the seeded fibrils are not structurally similar to extracted fibrils with three protofilaments.

The above deductions infer that the fibril structure from ssNMR could only be compared with the extracted fibrils with two protofilaments (pdb:6dso). The secondary structure predicted by chemical shifts obtained by ssNMR is similar to the extracted fibrils. However, an additional β-sheet from 13A to 15D is present in the seeded *in vitro* fibrils and an additional β-sheet in the extracted fibrils from 65Q to 69G. The structured β-sheet (β5) of extracted fibrils is not assigned from the ssNMR. It can be speculated that amino acids from 33 to 41 are dynamic and cannot be assigned sequentially.

The long-range interactions derived from different mixing times of DARRs and PARs are in accordance with the extracted fibrils. The isoleucine at the 6th position interacts with valine at the 51st position and serine at the 4th position, which complies well with the position of isoleucine in the cryo-EM structure. It also proves that the side chains of serine and isoleucine are in the same direction, which is also observed in the cryo-EM structure. The long-range connectivities between 8E → 46R, 10F → 17W → 16 M, 11Q → 43A / 44A, 19A → 21T, 22D → 24K, 18R → 30D, 20Y → 28W, 56K → 58S satisfy the structure of the cryo-EM structure of extracted fibrils (PDB:6dso). The result infers that seeded fibrils are

structurally similar to extracted fibrils, and seeding can be used as a template to prepare *in vivo-like* structures *in vitro.* However, the residues from 33 to 41 can be dynamic, contradicting the structured region from 33 to 41 amino acids.

The observed connectivities align well with the cryo-EM structure of extracted SAA fibrils. However, the structured β-sheet region from 33D to 38R was not assigned in solid-state NMR assignment studies. Therefore, the all-atom molecular dynamic simulation was performed to understand the dynamics of the residues in SAA fibrils which can lead to the absence of NMR resonances. The fibril morphology from the cryo-EM structure (PDB ID: 6dso and PDB ID: 6zch) and possible filament interface based on TEDOR spectra were used to execute the simulation, as shown in Figures 26 A and B. The simulation results showed that the root mean square fluctuations (rmsf) of all the residues are the same for all four models except K24, figure 11 C. Residues from 3-22 and 42-55 show lower fluctuations as they are part of the core of the amyloid fibril and constitute the β-sheet. On the other hand, K29, H36, and R38 showed the largest fluctuation as the residues were solvent exposed. However, the non-assignment of residues from 33-42 by solid-state NMR cannot be explained by the higher conformational dynamics of this region. Therefore, there is a possibility that SAA fibrils adopt an alternative conformation that causes the absence of NMR resonance. The alternative conformations might be separated by a high energy barrier which cannot be observed at the MD simulation timescale.

4.1.7 TEDOR for SAA fibrils

Transferred Echo Double Resonance is a heteronuclear measurement where the distance between dipole-coupled nuclei can be measured. For example, the ^{13}C-^{15}N correlation TEDOR spectrum is shown below in figure 27 A. The TEDOR spectrum at lower mixing time shows all the amino acids in the sequence with nitrogen at the alpha position as well as the nitrogen at the epsilon position. Therefore, the TEDOR at lower mixing time is very useful for deducing which amino acids can be sequentially assigned especially amino acids like lysine and arginine, which have specific chemical shifts because of epsilon nitrogen.

In the TEDOR at 1.9 ms mixing time, three lysines and two arginines are observed, which are in accordance with the assigned number of lysines and arginines in the sequence. However, the spectrum also proves that other arginine and lysine cannot be sequentially assigned. The histidine, which has a specific chemical shift of around 140 ppm, cannot be observed in the TEDOR at 1.9 ms mixing time.

The TEDOR at the higher mixing time provides the internuclear distance between the dipolar coupled nuclei. The distance can be calculated by observing peaks with different mixing times. It also shows the salt bridge, if any, present between two charged residues in the

fibrils. However, no additional peak is observed for SAA fibrils with a long mixing time, demonstrating the absence of the salt bridge in the seeded SAA fibrils. The salt bridge observed in the cryo-EM structure between aspartate at the 59th position, and the arginine at the 61st position is not present in the seeded *in vitro* fibrils.

27 A.

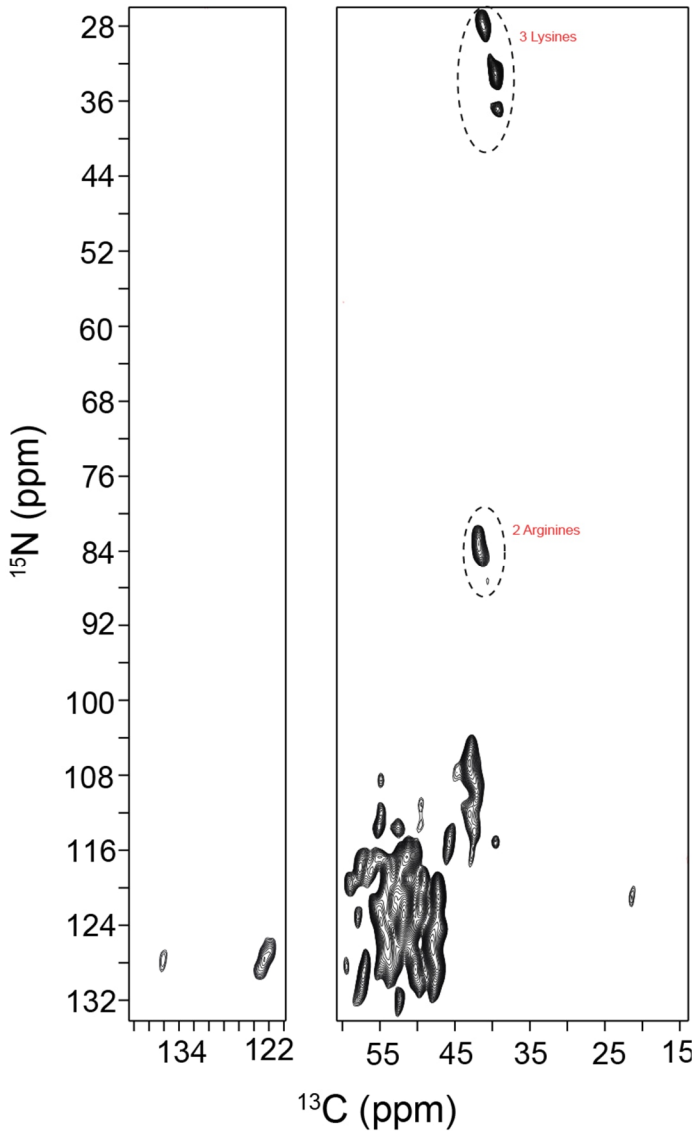

Figure 27. *TEDOR for SAA fibrils. A, The TEDOR spectra recorded for seeded SAA fibrils with 1.9 ms mixing time.*

4.1.8 Comparison of non-seeded in vitro fibrils with the seeded in vitro fibrils

The effect of seeding was studied by comparing the non-seeded *in vitro* fibrils with the seeded *in vitro* fibrils. As discussed before in section 4.1.3, SAA in the presence of seeds does not have any lag phase in the ThT kinetics, while there is a lag phase of approximately 15 hours for the non-seeded SAA. Therefore, the monomeric protein of SAA can use

extracted fibrils as the nuclei and grow into fibrils. In contrast, the monomeric protein interacts and form nuclei which can further develop in fibrils, as reflected in the non-seeded preparation.

A non-seeded fibril sample was prepared in identical conditions and measured with the same ssNMR experiments to compare the effect of seeding on the structure of fibrils. The TEM images, as shown below, depict the morphology of SAA fibrils prepared without seeds. The fibrils are long, twisted, and composed of three protofilaments with a diameter of approx. 19 nm, different from the short, thin, straight fibrils prepared with seeds constituting only two protofilaments.

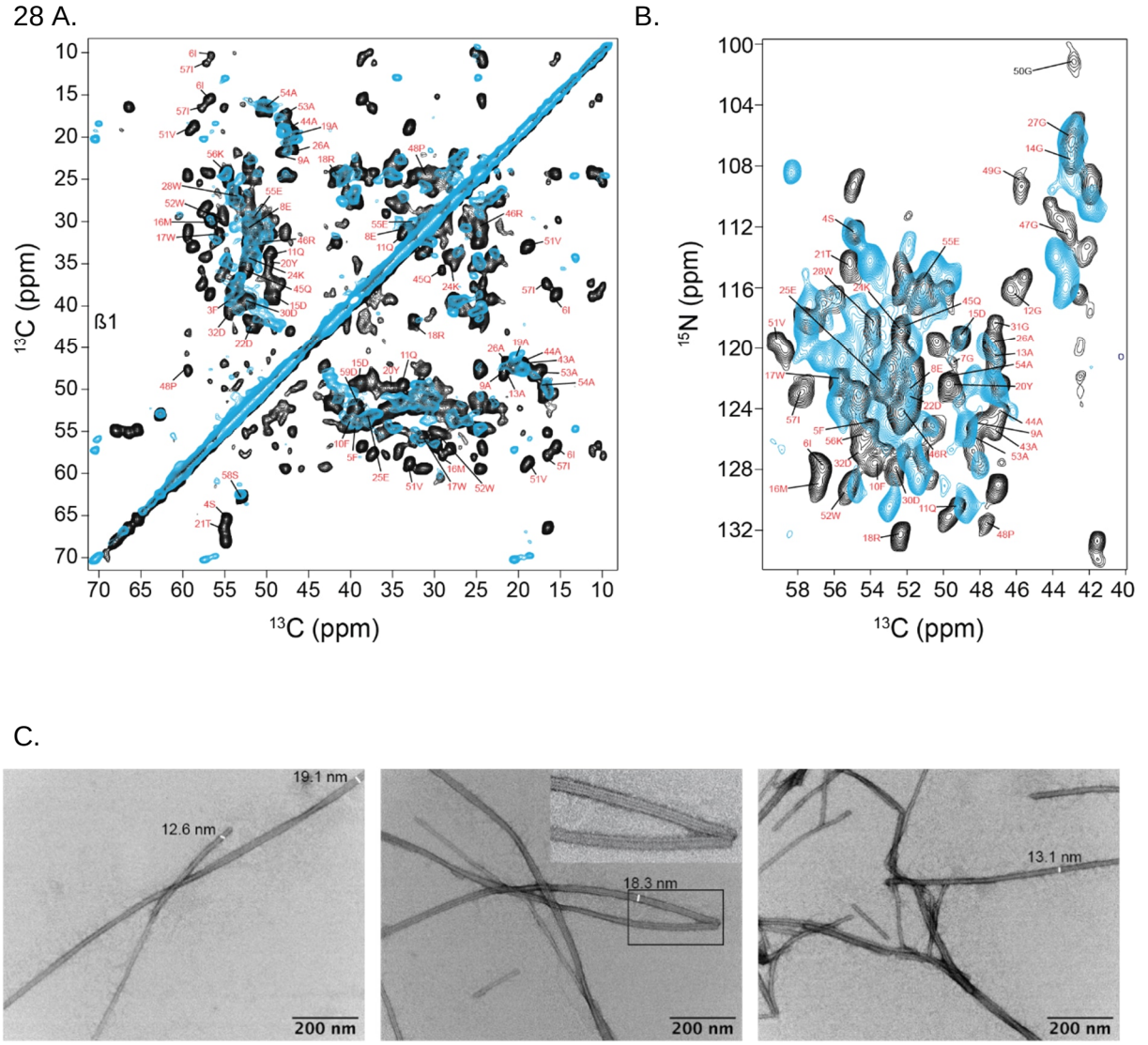

Figure 28. *Characterization of non-seeded SAA fibrils. A, Overlay of 13C-13C DARR spectra of seeded (in blue) and non-seeded (in black) SAA fibrils. B, Overlay of 13C-15N NCA spectra of seeded (in blue) and non-seeded (in black) SAA fibrils. C, TEM images of SAA fibrils depicting two morphologies with diameter of approx. 13 nm and 19 nm.*

Furthermore, the ^{13}C-^{13}C (DARR) and ^{13}C-^{15}N (NCa) correlations of non-seeded fibrils do not match the seeded sample. There are less number of peaks in both spectra of the non-seeded sample compared to the seeded sample. Hence, the non-seeded fibrils have a smaller structured core than the seeded fibrils. The ^{13}C-^{15}N (NCa) correlation of non-seeded fibrils had broader peaks that implicate fibrils'. Additional peaks were observed at the serine and threonine region indicating polymorphism. The smaller size of the structured core is in accordance with the cyro-EM results. However, there is a possibility that the structure of *in vitro* prepared fibrils in the current project is not the same as deduced by cryo-EM in previous publications. Since the signal-to-noise ratio of the non-seeded fibrils is low with polymorphism, a sequential assignment is not possible.

There is only one isoleucine peak present in the non-seeded fibrils corresponding to isoleucine at the 6th position, and the one at the 57th position is missing. Similarly, 45Q, 46R, 48P, 51V, 52 W, and 59D are not present in the structured region of the non-seeded fibrils. The aromatic region of the non-seeded fibrils is also not well resolved as it is for the seeded fibrils. The Cg for three tryptophans are not as high quality in the non-seeded fibrils as the seeded fibrils, and the same applies for the tyrosine and phenylalanine. Only Cg for the tryptophan at the 17th position is present in the non-seeded fibrils. However, the peak is shifted, and it could be corresponding to the same set of peaks that overlap with the Cd, Ce, and Cz for the 52nd tryptophan. It confirms that seeding can prepare high-quality, homogenous SAA fibrils which could be analyzed with ssNMR. In the absence of seeds, only a small region of SAA protein from the N-terminal is amyloidogenic. The other part of protein can be flexible and does not participate in the structure of the fibrils.

4.1.9 Conclusion and Discussion

Murine Serum Amyloid A is an intrinsically disordered protein that attains alpha-helical structure at a lower temperature. The biophysical characterization of the protein proved that with the increase in temperature, SAA unfolds and aggregates at basic pH. Free SAA is unstable at higher temperatures and concentrations, which does not allow the assignment of monomeric protein by NMR.

Seeding the SAA with the extracted fibrils reduces the lag phase, resulting in homogenous, thin fibrils. The fibrils were assigned using solid-state NMR experiments. The position of β-sheets was predicted by the chemical shift index. The long-range interactions were identified by long-mixing DARR and PAR experiments. The connectivities and the β-sheet investigated by solid-state NMR align well with the dominant fibril morphology (PDB ID 6dso) identified by cryo-EM of the extracted fibril. However, NMR assignment was not possible for 33-42 residues, which constitutes a structured region in fibril morphology described by cryo-EM.

The molecular dynamic simulation of different models concludes that the dynamics of these residues do not cause the absence of NMR resonance. This led to the possibility of an alternative conformation. The MD simulation could not predict the alternate conformation as the MD trajectory length was insufficient to overcome the high energy barrier.

Furthermore, non-seeded fibrils were compared with the seeded fibrils. Multiple peaks were observed for a single residue which proved the polymorphism. On the contrary, polymorphism was not observed for the seeded fibrils. This proved that seeds could act as a template and lead to fibril formation of homogenous, well-structured fibrils. Non-seeded fibrils also displayed fewer peaks than the seeded fibrils. This showed that non-seeded fibrils have a smaller core than seeded fibrils, as identified by cryo-EM studies [27].

The INEPT spectra were recorded to identify the dynamic region of SAA fibrils. The INEPT spectra showed that the C-terminal of SAA remains dynamic after the fibril formation. The C-terminal does not affect the SAA fibril and remains attached to the fibril structure. The N-terminal of SAA comprises the structured core while C-terminal remains flanking as a dynamic tail. The current study describes the mechanism of fibril formation and the structure of *in vitro* seeded and non-seeded fibrils. Future studies with cellular components can identify the role of enzymes and cellular components on the aggregation, stability, and structure of SAA fibrils.

4.2 Effect of heparin on the aggregation mechanism of SAA and on the structure of SAA fibrils.

4.2.1 Effect of Heparin on the kinetics of fibril formation

The kinetics of fibril formation describes many processes undergoing, from nucleation to the formation of mature fibrils. It is also used to understand the effect of inhibitors and enhancers on fibril formation. Heparin is known to enhance fibril formation in many amyloidogenic proteins. The previous studies of AL, tau, and IAPP [123, 128, 129] have shown that heparin can enhance aggregation. Heparin belongs to the GAG family and is readily available in the human body. Therefore, it is crucial to study the effect of heparin on the aggregation process and the underlying molecular mechanism.

In the current project, the kinetics of fibril formation by SAA was followed by a ThT assay. The emission fluorescence of ThT was recorded at different time points at different concentrations of heparin, as shown in figure 29 A. It demonstrates the effect of heparin on the kinetics of SAA aggregation. The SAA without seeds follows a sigmoidal growth curve with a slow lag phase of approximately 56 hours. Heparin is a polymer with an average molecular weight of 18 kDa. The heparin with a concentration of 30 times more than the protein concentration causes a decrease in lag phase to approx. 25 hours (reduced to half). Further increase in the heparin concentration reduces the lag phase of SAA fibril formation.

The lag phase and the half-time for the different concentrations of heparin are plotted in figure 30. As depicted in the figure, the lag phase reduces to almost half in the presence of 30X heparin. However, a further increase in heparin concentration reduces the lag phase slowly. At 50X heparin concentration, the lag phase reduces to its minimum. The addition of heparin to 60X does not reduce the lag phase. Further increase of heparin to 70X leads to an increase in lag phase, implying that the kinetics become slower.

The half-time shows similar behavior in the presence of heparin. The increase in heparin concentration leads to decrease in the corresponding half time. The reduction in the lag phase and half time follows the polynomial curve. The kinetics in the presence of heparin confirms that heparin accelerates the fibrillation process. The impact of SAA on the structure and mechanism of fibrillation is described in the following sections.

29 A.

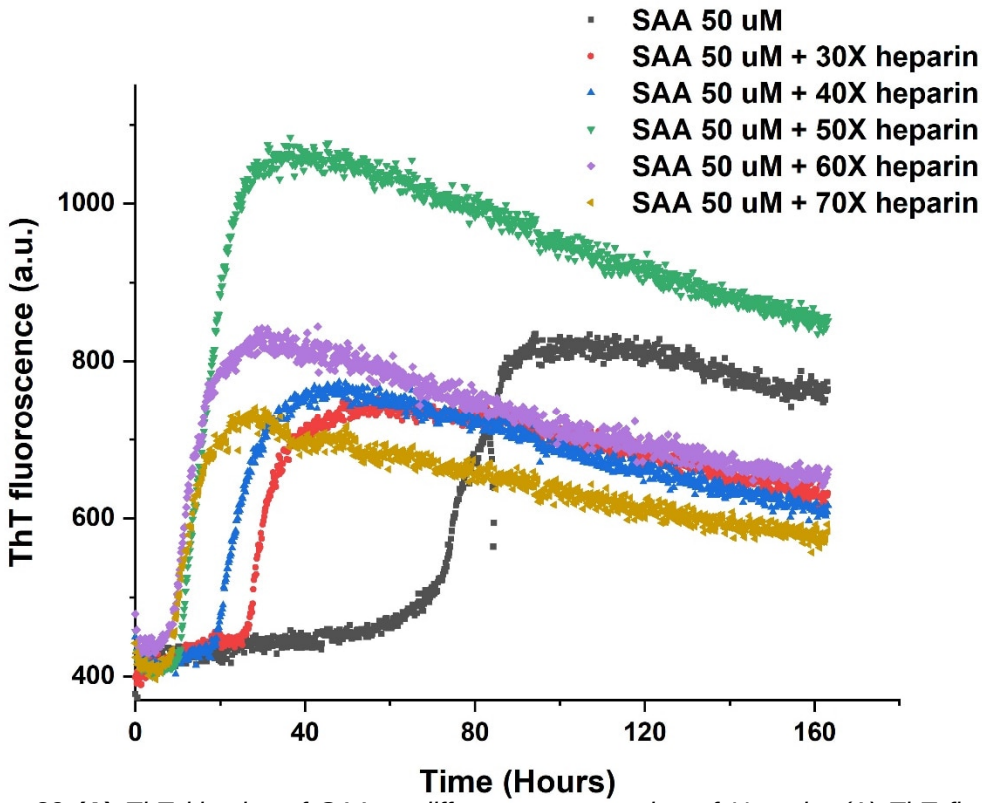

Figure 29 (A) *ThT kinetics of SAA at different concentration of Heparin. (A) ThT fluorescence followed for every 10 minutes at 0mM(black), 1.5mM(red), 2mM(blue), 2.5mM(green), 3mM(purple), and 3.5mM(golden) of heparin.*

30 A.

B.

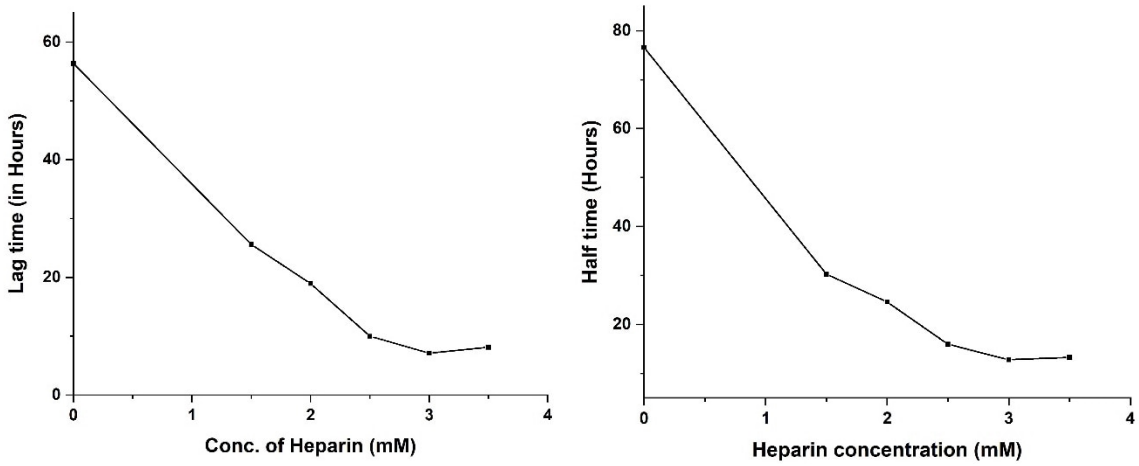

Figure 30. *Effect of heparin on lag phase and half time A. The decrease in the lag time and B. half time with the increase in the concentration of heparin*

4.2.2 Effect of Heparin on the structure of SAA fibrils

The SAA fibrils were prepared with 5% *ex vivo* fibrils as seeds in the presence and absence of heparin. The mature fibrils prepared in the absence of heparin were further titrated with heparin to understand the impact of heparin on mature fibrils.

The two-dimensional ^{13}C-^{13}C correlation spectra of SAA fibrils prepared in the presence of heparin were recorded and compared with SAA fibrils prepared without any heparin. Figures 31 A and C display the comparison of SAA fibrils with seeds (black) and the fibrils prepared in the presence of heparin (blue) and the overlay of SAA fibrils with seeds and the fibrils titrated with heparin (green), respectively. The two spectra do not show any change in the pattern, indicating that SAA fibrils are structurally similar in the presence and absence of heparin. However, there are chemical shifts observed at different residues. Additionally, a few peaks disappeared while some additional peaks appeared in both spectra.

Similar results are observed for the two-dimensional ^{13}C-^{15}N (NCA) correlation of SAA fibrils (figure 31 B and D). Anyhow many residues show chemical shifts in the presence of heparin. However, the SAA fibrils titrated with heparin overlay very well with fibrils without heparin. A few additional peaks are observed after titrating the fibrils with heparin. The Cα in NCA correlation for fibrils prepared with heparin has narrow peaks. The missing peaks are mostly restricted to the glycine region. The alanine region in the NCA correlation shows more shifts than the addition or deletion of peaks. Some unassigned peaks have chemical shifts or are missing in the presence of heparin, which depicts the possibility of the dynamic region of SAA fibrils interacting with heparin.

As in a detailed view (figure 32), the chemical shifts are mainly observed for the positively charged residues or the amino acids in their proximity. For example, the following basic amino acids show chemical shifts in the presence of heparin: R18, K24, and K56. The residues which are in proximity to R18, like D15, M16, W17, and T21, also show minor shifts. Similarly, shifts are observed in S58 and I57, which are in proximity to K56. However, hydrophilic amino acid-like S4 displayed a chemical shift as well.

Interestingly, these residues do not show any chemical shift or splitting after titrating the preformed fibrils with heparin. A chemical shift is observed only for K24 for these fibrils.

This observation confirms that amino acids that are part of the core do not interact with the heparin as the side chains are not accessible to the buffer. Therefore, heparin cannot access these residues, and no chemical shifts are observed. On the other hand, the side-chains for K24 must point towards the buffer, which is accessible to heparin. The observations are

consistent with the proposed cryo-EM structure of SAA fibrils extracted from mice and the current project's NMR studies of seeded SAA fibrils.

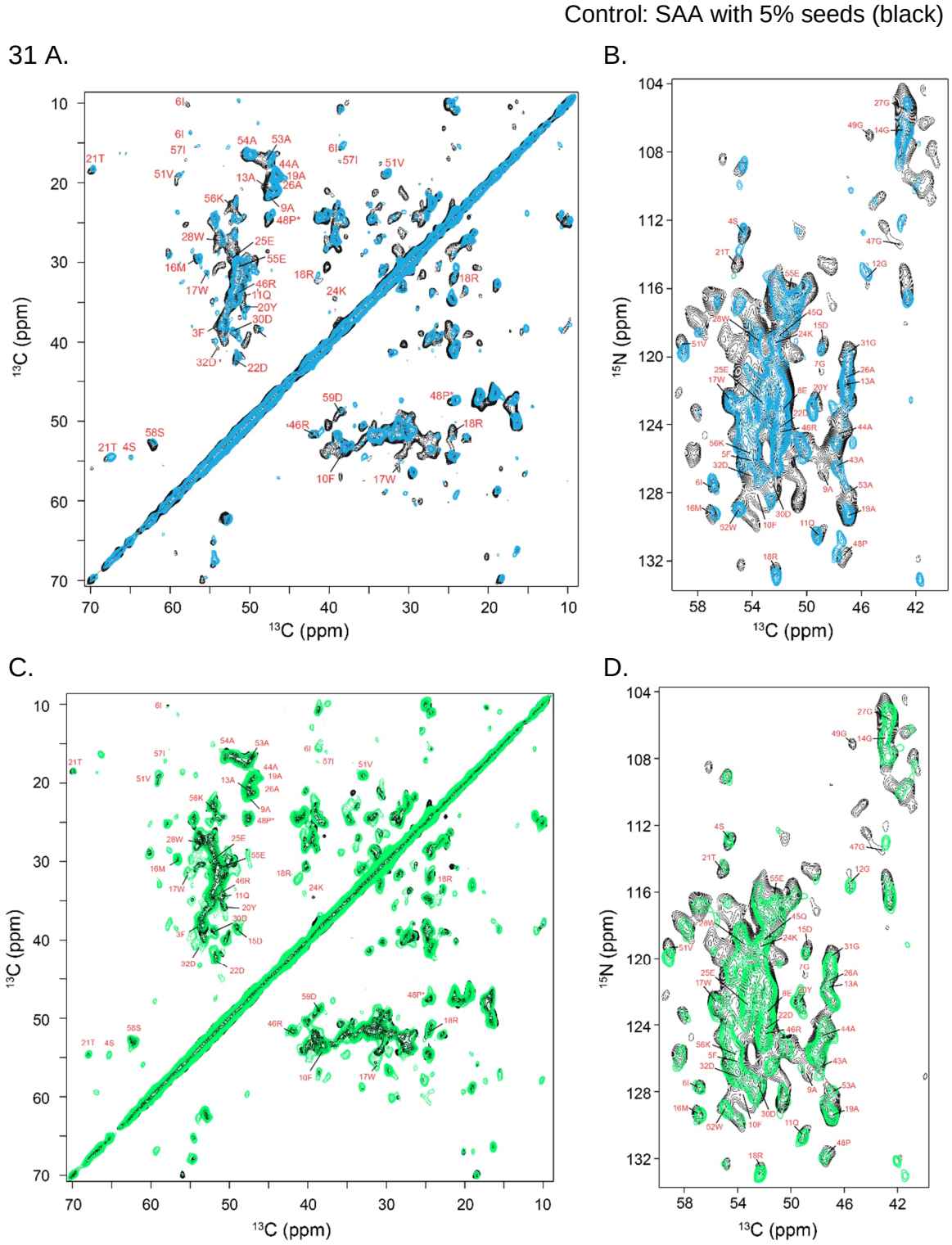

Figure 31. *NMR experiments of SAA fibrils***.** *A. The overlay of ^{13}C-^{13}C correlation (DARR) of SAA fibrils (black) and SAA fibrils prepared in presence of heparin (blue) and B, titrated with heparin (green). C, the overlay of ^{15}N-^{13}C correlation (NCA) of SAA fibrils (black) and* SAA fibrils prepared *in presence of heparin (blue) and D, titrated with heparin (green). All the fibrils were prepared with 5% seeds.*

The SAA unfolds while forming the fibrils as described in the CD spectra detailing the dynamics of SAA fibril formation (section 4.1.1). As a result, all the residues are accessible to heparin during the fibril formation. This leads to many residues showing chemical shifts. The data confirms that heparin interacts with positively charged residues of the protein. Therefore, it can be hypothesized that heparin provides a platform for SAA protein to assemble into fibrils. However, heparin does not play any role in the structure of fibrils.

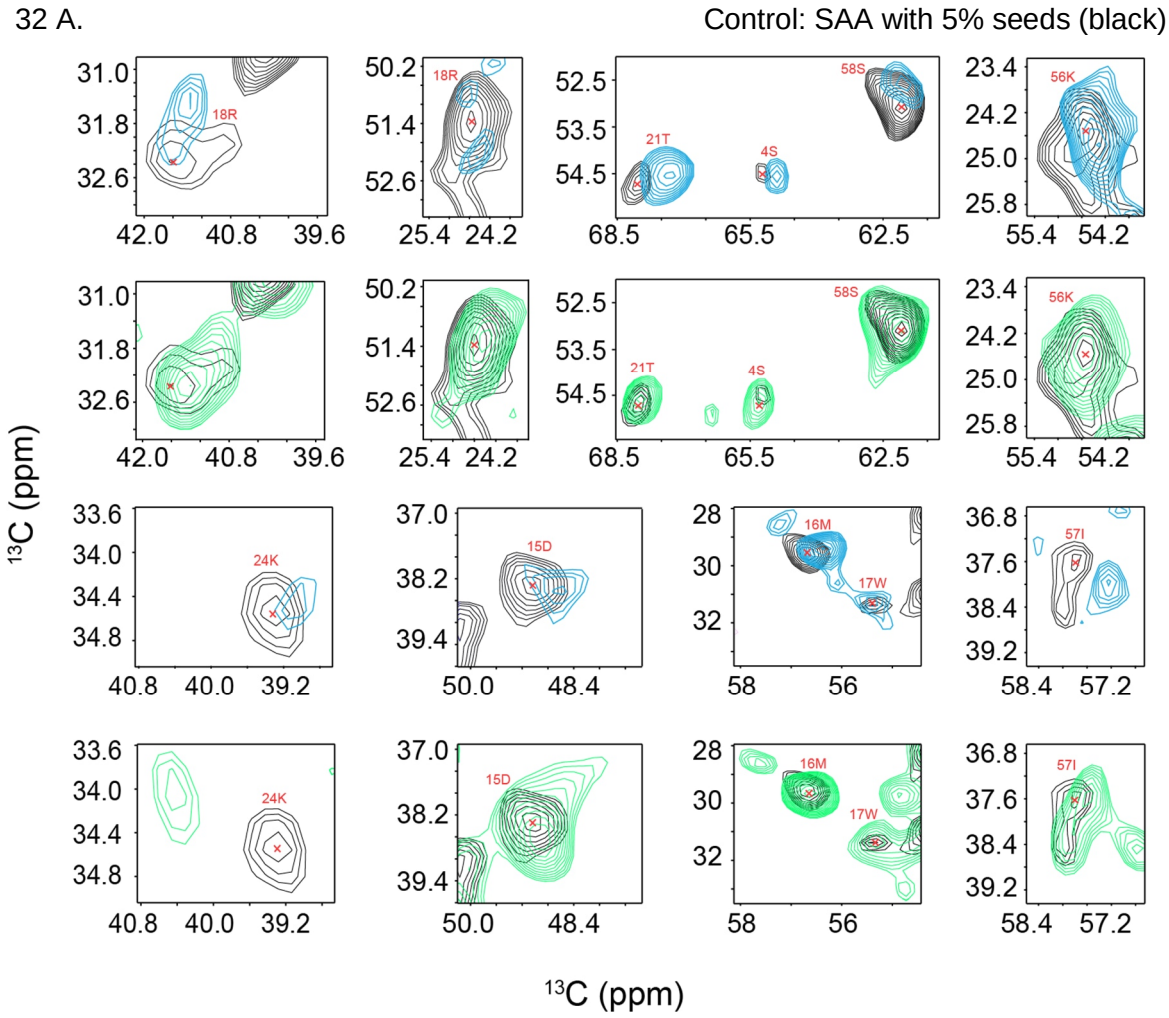

Figure 32. *Detailed view of DARR in presence and absence of heparin. A, the chemical shifts observed for R18, T21, S5, S58, K56, K24, D15, M16, W17, and I57 in SAA fibrils prepared with heparin (blue) and titrated with heparin (green).*

4.2.3 Heparin stabilizes the SAA fibrils

The results described in section 4.2.2 proved that heparin interacts with the positively charged residues of SAA. However, adding heparin does not affect seeding propensity, and the structure of fibrils remains unaltered. The TEDOR spectra were recorded to identify the chemical shifts for the side-chains of positively charged residues. The results from TEDOR are displayed in Figures 33 A and B.

Chemical shifts are observed for all Cε side-chain for lysine (around 40 ppm) in the presence of heparin. In addition to chemical shifts, the splitting of peaks is detected. Argine Cδ side-chain, on the other hand, shows only an intensity change and minor chemical shift for one of the two observed arginines.

Moreover, the Cγ side chain also appears for arginine and lysine in the presence of heparin. The Cγ side chains are present not only for the basic residues but also for other residues of SAA fibrils prepared in the presence of heparin, as observed in Figures 33 A and B. The aromatic side-chains are also visible for SAA fibrils with heparin (125-135 ppm).

Control: SAA with 5% seeds (black)

33 A. SAA with 5% seeds and heparin (blue)

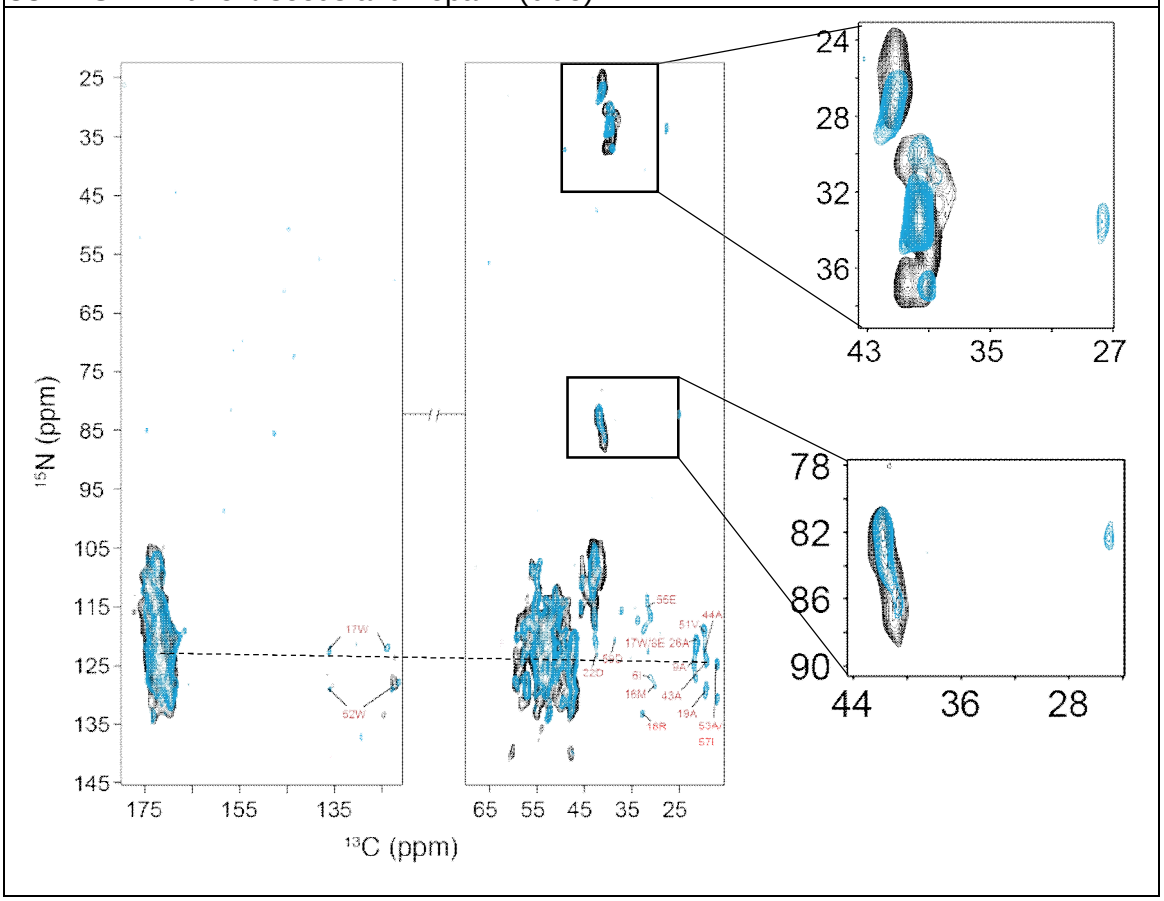

B.

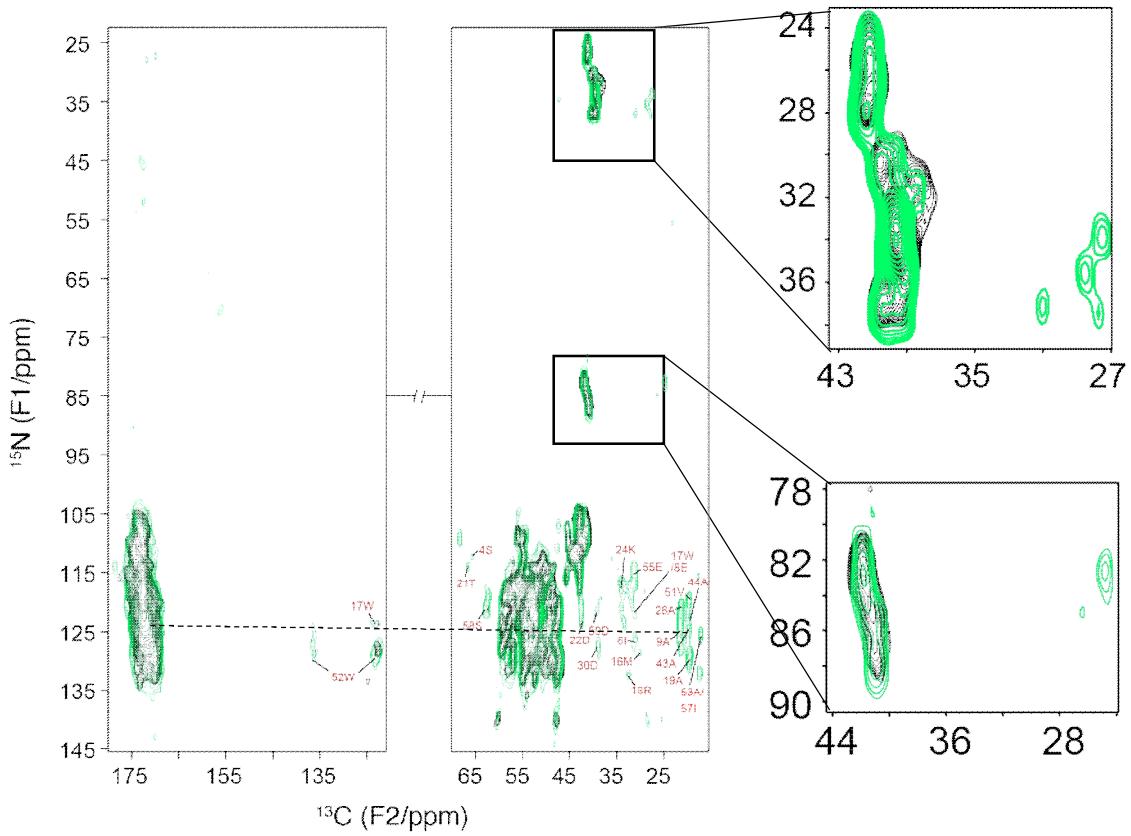

Figure 33. *TEDOR for SAA fibrils. Overlay of TEDOR of SAA fibrils and A, fibrils prepared with heparin(blue), B titrated with heparin (green).*

Similar behavior is observed for preformed SAA fibrils titrated with heparin. The peaks corresponding to the side-chains of positively charged residues and other residues are visible for SAA fibrils titrated with heparin. The chemical shift is observed for only one Cε of lysine while all other residues overlay well on each other. The titrated fibrils have more Cγ side chains than fibrils prepared with heparin. The Cγ side-chain peaks for K24, D30, and Cβ side-chains for S4, T21, and S58 are observed only in SAA fibrils titrated with heparin.

The 1-dimensional extracts from the row show that the intensity of Cα is less for SAA fibrils prepared in the presence of heparin, as shown in figure 34 A. The loss in intensity can be observed because of the low amount of SAA fibrils while accommodating the bound heparin in the rotor. On the contrary, the intensity of Cα enhances for SAA fibrils titrated with heparin (figure 34 B). The results show that the fibril core is more structured after adding heparin; therefore, side-chains are visible, and the intensity of peaks increases for SAA fibrils in the presence of heparin.

Furthermore, the CD spectra of SAA fibrils were recorded for SAA fibrils prepared with seeds in the presence and absence of heparin. The CD spectra of SAA fibrils with seeds display a signal of β-sheet. The SAA fibrils with seeds in the presence of heparin at the same

concentration and volume have a more intense signal for the β-sheet conformation. The heparin itself does not have any minima for β-sheet; however, it shows a slight α-helical characteristic. The higher ellipticity for CD can arise from a more structured fibril which further confirms that heparin stabilizes the structure of fibrils.

34 A.

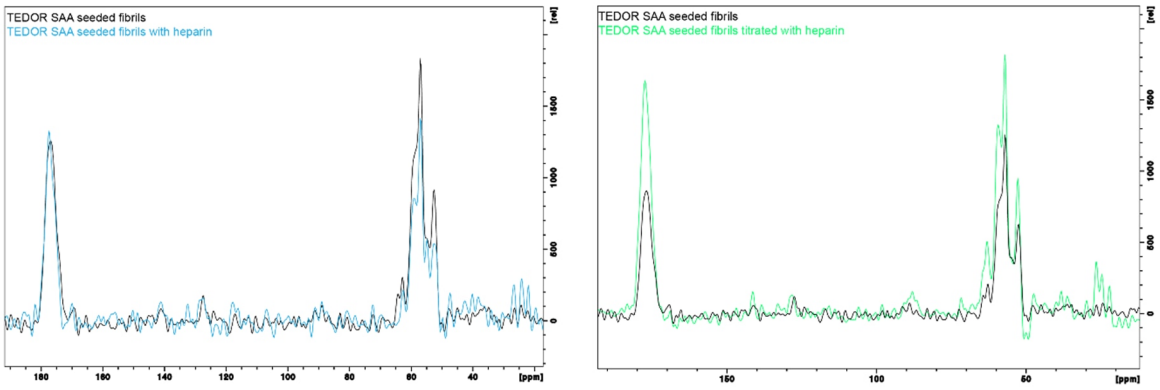

Figure 34. *Overlay of 1D extract of SAA fibrils with seeds (black) and A, SAA fibrils prepared with heparin B, and SAA fibrils titrated with heparin.*

35 A

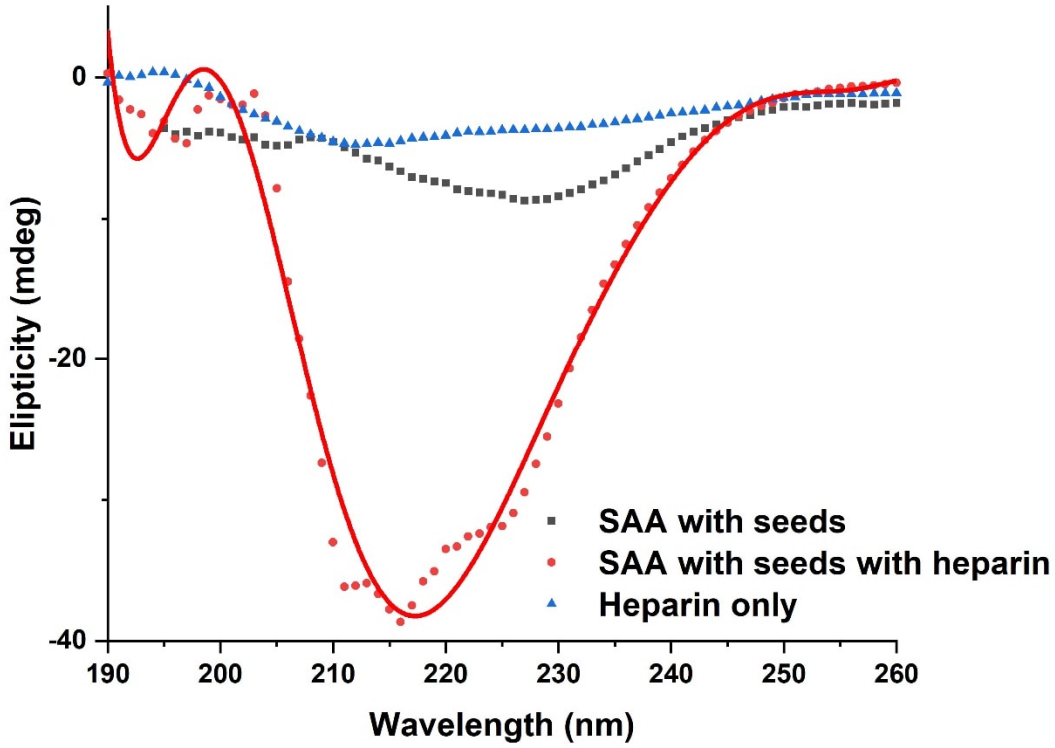

Figure 35. *CD spectrum of SAA fibrils. A, SAA fibrils prepared with seeds (black), SAA fibrils in presence of heparin (red), and only heparin (blue). The fibrils prepared in presence of heparin shows higher ellipticity than in absence of heparin.*

4.2.4 SAA fibrils are more apolar in presence of heparin

The unfolding of a protein and its transition to amyloid fibril is studied using the intrinsic fluorescence of tryptophan. The tryptophan has a λ_{max} of 335 nm when it is buried, and a solvent-accessible tryptophan has a λ_{max} of 355 nm. The fluorescence emission of tryptophan in SAA fibrils is shown in figure 36 A.

The fibrils with heparin have a higher emission at 335 nm than those without any heparin. Furthermore, the emission spectrum's maxima are blue-shifted in the presence of heparin. The blue shift in emission spectra depicts a more apolar environment. Therefore, the residues forming the core of SAA fibrils are more tightly packed for SAA fibrils grown in the presence of heparin. The results are consistent with visible side-chain peaks for TEDOR spectra.

36 A.

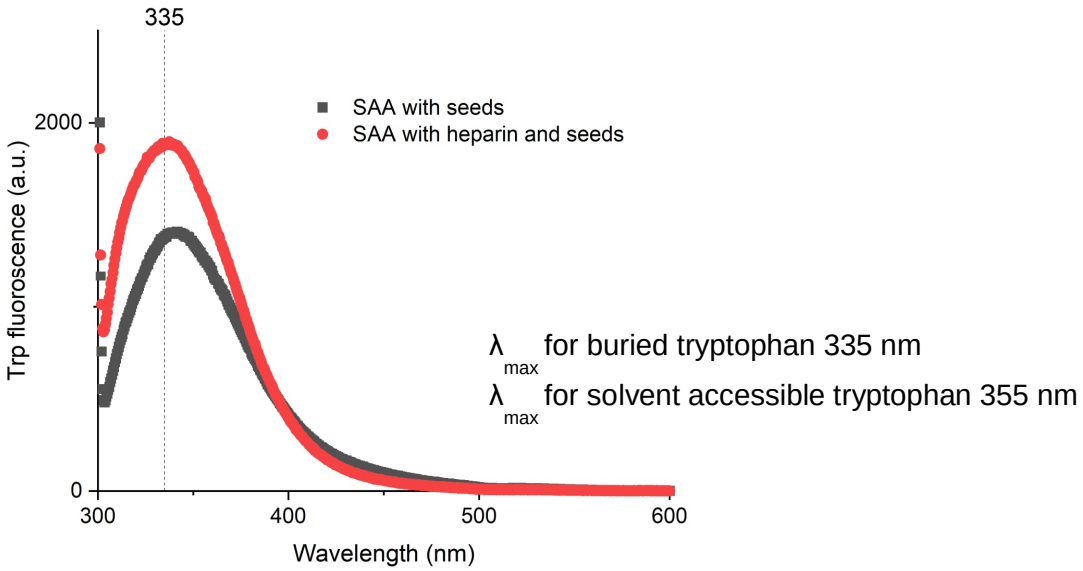

Figure 36 A. *Tryptophan florescence spectrum of SAA fibrils prepared with 5% seeds (black) and SAA fibrils with 5% seeds and heparin (black). The fibrils were excited at 295 nm at 37°C.*

4.2.5 Heparin reduces the heterogeneity of non-seeded SAA fibrils

The effects of heparin were further investigated on SAA fibrils without seeding. The non-seeded SAA fibrils displayed heterogeneity and multiple sets of peaks for a single residue. The heterogeneity is identified clearly at the resolved peaks. For example, the serine and threonine regions have multiple sets of peaks instead of three resolved ones. The quality of spectra reduces for SAA fibrils without seeds, and fewer peaks are observed as compared to seeded fibrils.

In the presence of heparin, the SAA fibrils show fewer peaks, as depicted in the ^{13}C-^{13}C correlation (DARR) overlay of non-seeded SAA fibrils (in black) and non-seeded SAA fibrils with heparin (in blue) in figure 37 B. The peaks superimpose very well on each other. However, some peaks disappear in the presence of heparin. As a result, the DARR spectrum in the presence of heparin displays narrow, strong peaks, while the spectrum is broad in the absence of heparin. Additional peaks are visible in the overlay ^{13}C-^{15}N correlation (NCA) in figure 37 C. The peaks are again more intense in the presence of heparin, and chemical shifts are observed in many peaks. The NCA spectrum with heparin has more peaks than the SAA fibrils without heparin. The glycine and alanine regions show considerable chemical shifts and additional peaks in the presence of heparin.

37 A. ^{13}C-^{13}C Correlation (DARR) for SAA non-seeded fibrils

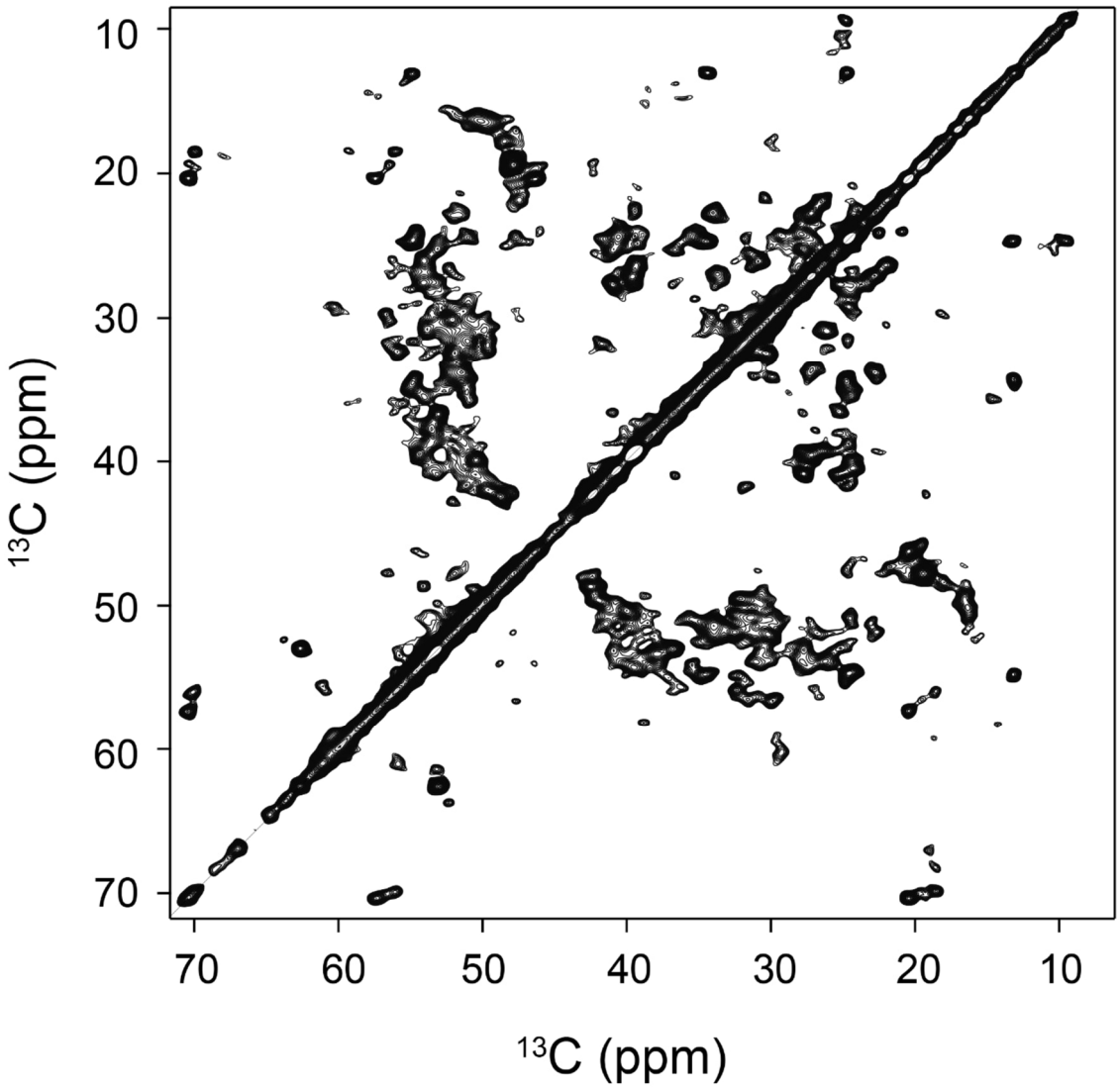

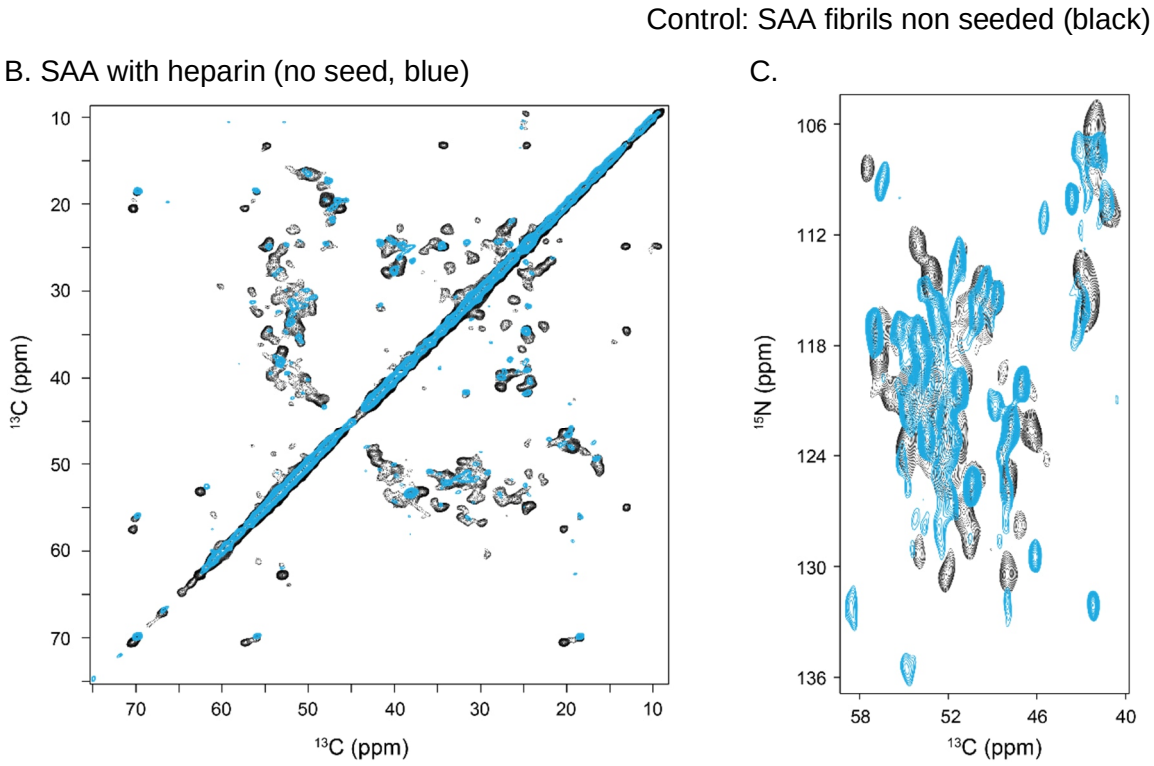

Figure 37. *NMR spectra for SAA without seeding. A, ^{13}C-^{13}C correlation (DARR) of non-seeded SAA fibrils. B, Overlay of ^{13}C-^{13}C correlation (DARR) and C, ^{15}N-^{13}C correlation (NCA) of non-seeded SAA fibrils in the absence (black) and presence of 50X heparin (blue).*

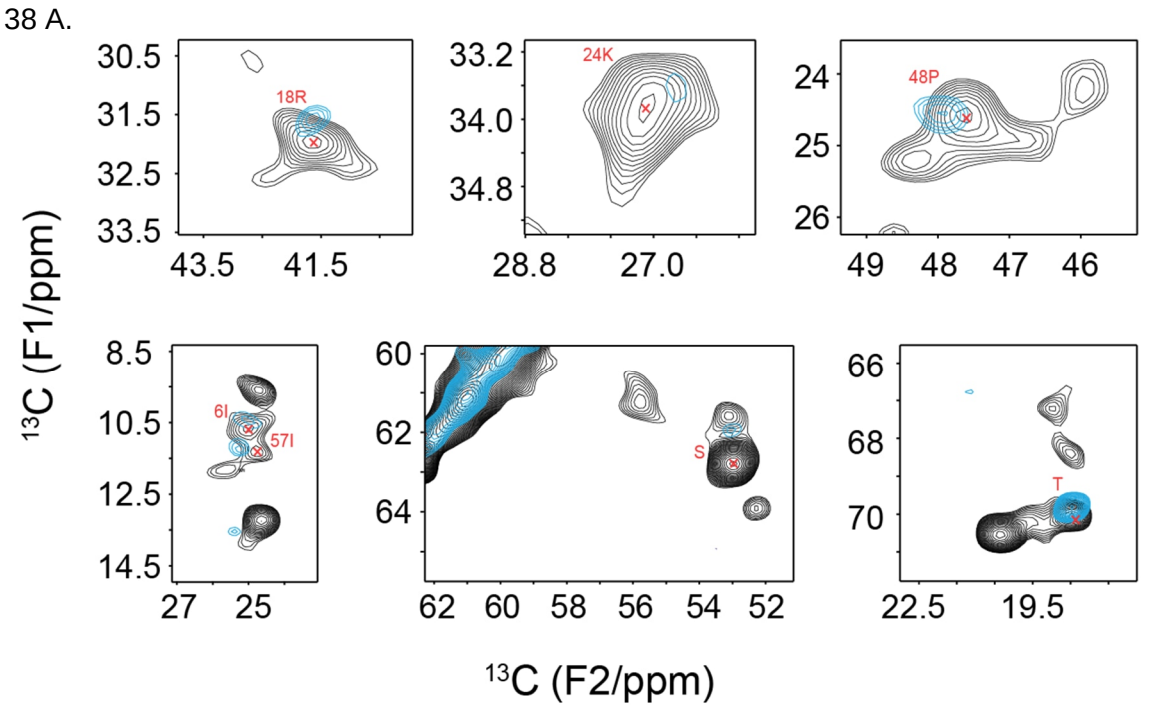

Figure 38. *Selected peaks to demonstrate the effect of heparin. A. The SAA fibrils without seeds are depicted in black and in presence of heparin in blue. The R18 and K24 show chemical shifts. The multiple sets of peaks for P48, I6, I57, S, and T21 are reduced to a single peak.*

A detailed view of the ^{13}C-^{13}C correlation (DARR), as depicted in figure 38 A, shows the effects of heparin on SAA fibrils. R18 and K24 show a chemical shift in the presence of heparin. Additionally, multiple peaks observed for R18, P48, I6, I57, S58, and T21 are narrowed to a single peak in the presence of heparin. The NMR results propose that heparin allows the growth of only certain conformers of SAA.

The results are further evidenced by the TEM images of SAA fibrils, as shown in figure 39. The SAA fibrils without seeds consist of three protofilaments with a diameter of 18-19 nm, and thinner fibrils with protofilaments of diameter approx. 12-13 nm. On the other hand, the fibrils in the presence of heparin have only thinner fibrils with protofilaments of a diameter of approx. 12-13 nm.

The heparin somehow does not allow SAA assembly in a trimeric structure. The cryo-EM structure of *ex-vivo* fibrils with three protofilaments shows that D22, K24, and E25 are involved in the inter-protofilament interface to stabilize the structure [27]. Since K24 shows a chemical shift in the presence of heparin, it is verified that heparin binds at K24. Therefore, SAA cannot stabilize in a three-protofilament conformation.

39 A.

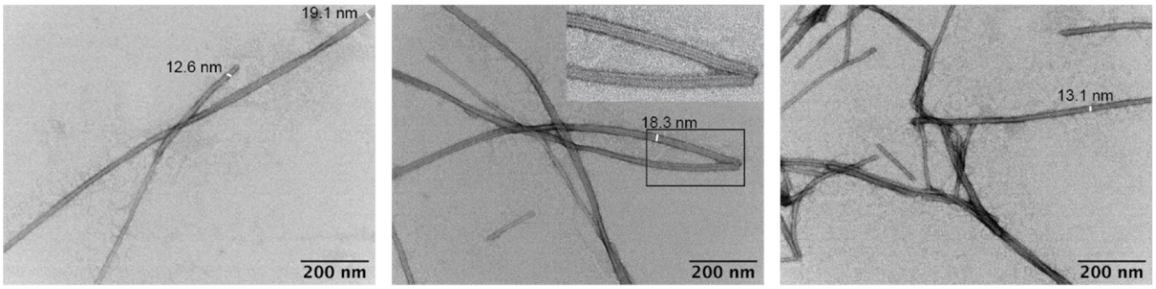

B.

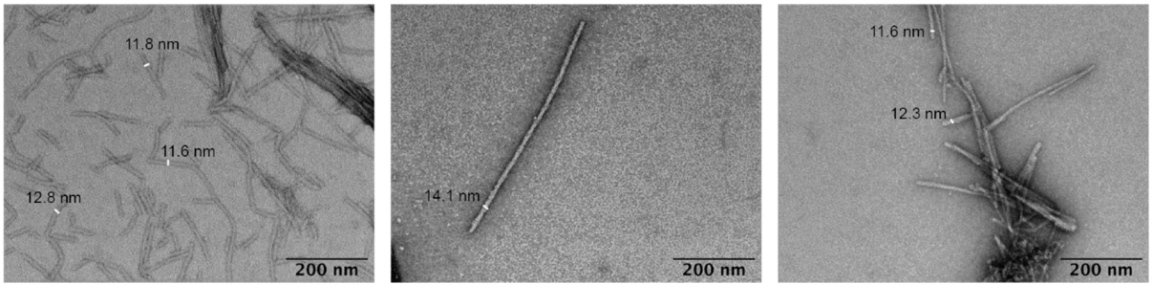

Figure 39. *TEM images of unseeded SAA fibrils. A, TEM images of unseeded fibrils in absence of heparin. SAA fibrils consist of fibrils with 2 and 3 protofilaments. B, SAA fibrils in presence of heparin consisting of fibrils only with 2 protofilaments*

4.2.6 Effect of heparin on the non-structured region flanking from SAA fibrils

The SAA fibrils are formed with a structured core region and a flexible C-terminal flanking out of the core, as deduced from INEPT experiments on SAA fibrils. The INEPT experiments were performed for seeded SAA and non-seeded SAA fibrils in the presence of heparin.

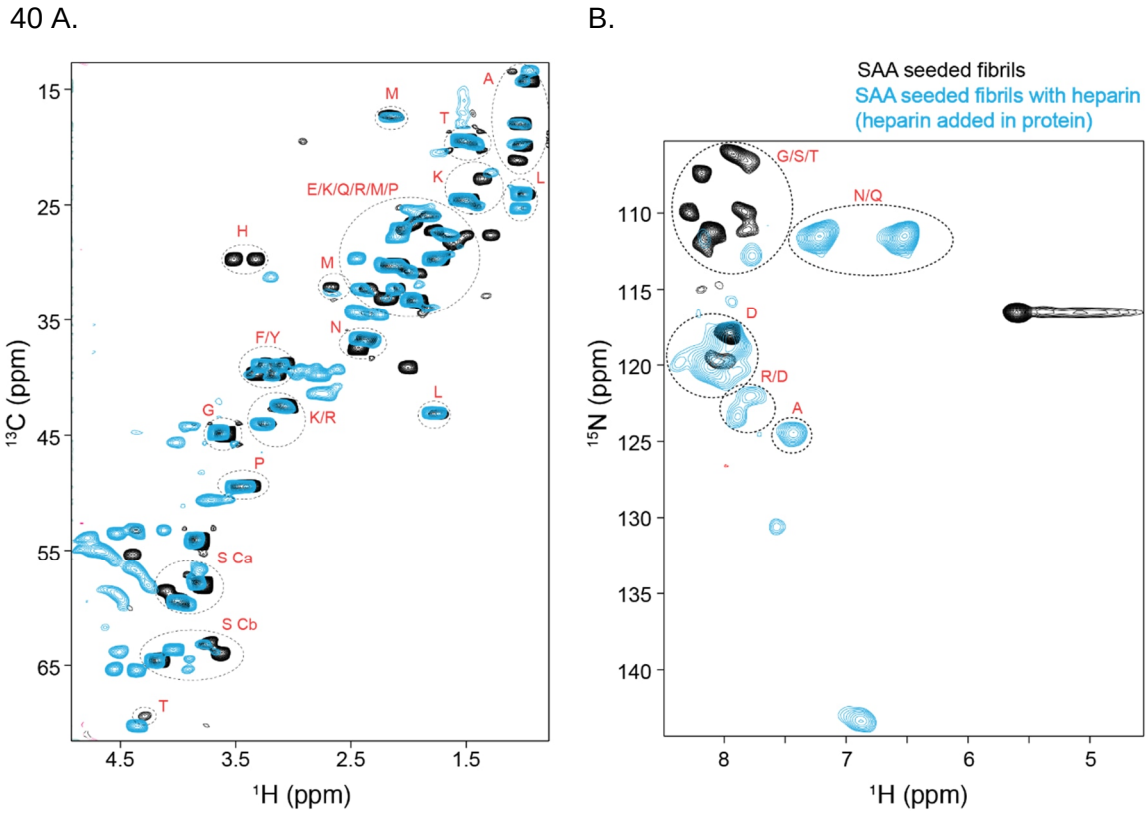

Figure 40. *INEPT spectra of seeded SAA fibrils. A, Overlay of ^{1}H-^{13}C correlation spectra of seeded fibrils in the presence (blue) and absence (black) of heparin. B, Overlay of ^{1}H-^{15}N correlation spectra of seeded fibrils in the presence (blue) and absence (black) of heparin. The INEPT spectra show the flexible region of fibrils. (Fibrils grown in the presence of heparin)*

With the addition of heparin, a few more peaks are observed in the aromatic and S/T regions of ^{1}H-^{13}C INEPT spectra, as depicted in figure 40. The residues in the heparin sample overlay very well with seeded fibrils without heparin. However, the histidine peak for seeded SAA fibrils with heparin shows a chemical shift, while there is no peak visible corresponding to the other heparin. The glycine peaks are missing in ^{1}H-^{15}N INEPT spectra for seeded SAA fibrils prepared with heparin. However, additional peaks are observed in the region of charged residues. Although few chemical shifts are observed, heparin does not bind to the flexible C-terminal of seeded SAA fibrils, as all the peaks are visible in the presence of heparin.

For the non-seeded SAA fibrils, fewer peaks are visible in the presence of heparin in both ^{1}H-^{13}C and ^{1}H-^{15}N INEPT spectra (figure 41). The disappearance of peaks can correspond to

either having fewer polymorphs in the presence of heparin or binding of heparin to the C-terminal of the non-seeded fibrils.

41 A. B.

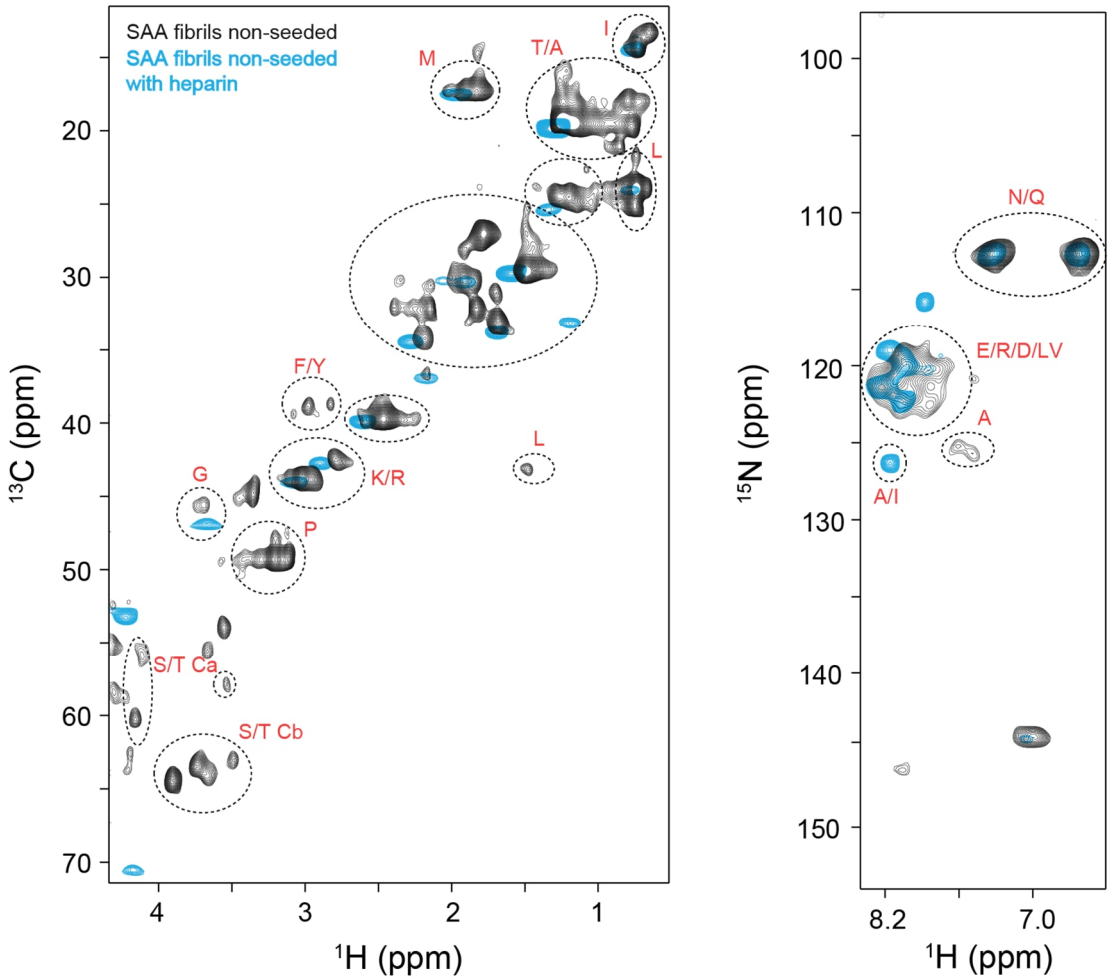

Figure 41. *INEPT spectra of non-seeded SAA fibrils. A, Overlay of ^{1}H-^{13}C correlation spectra of non-seeded fibrils in the presence (blue) and absence (black) of heparin. B, Overlay of ^{1}H-^{15}N correlation spectra of non-seeded fibrils in the presence (blue) and absence (black) of heparin. The INEPT spectra show the flexible region of fibrils. (Fibrils grown in the presence of heparin)*

4.2.7 Binding of Heparin with SAA fibrils

The addition of heparin causes chemical shifts, disappearance, and appearance of new peaks. However, it is not clear whether heparin remains bound to SAA after fibril formation or only affects the process of fibril formation. The ^{13}C direct 1D spectrum was recorded to observe whether SAA remains bound to the SAA fibrils.

42 A.

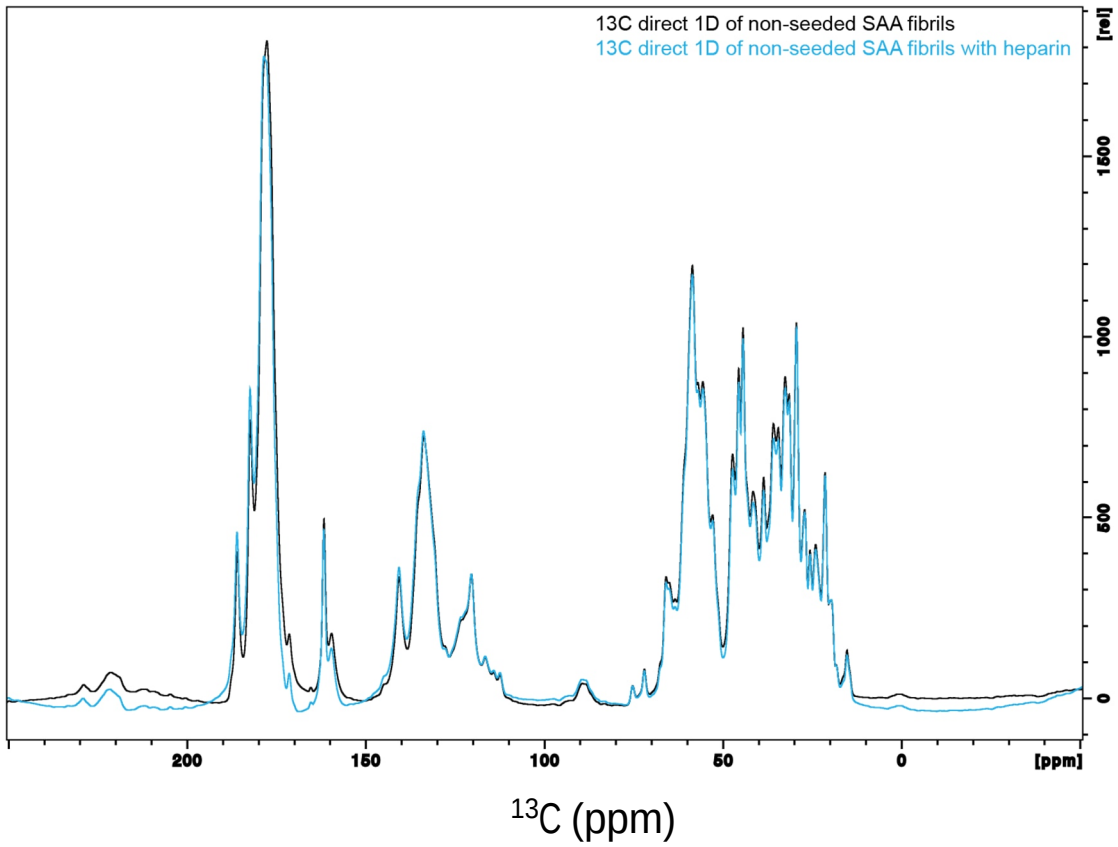
13C direct 1D of non-seeded SAA fibrils
13C direct 1D of non-seeded SAA fibrils with heparin
[rel]
1500
1000
500
0
200
150
100
50
0
[ppm]
13C (ppm)

B.

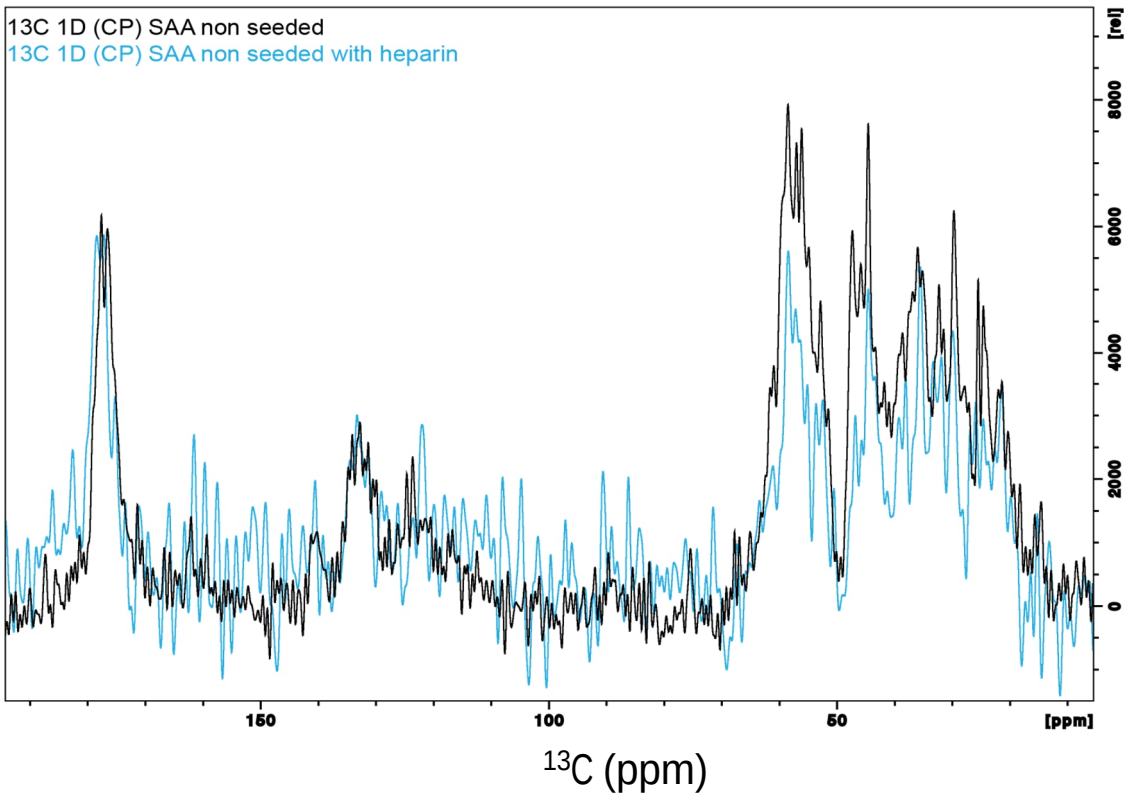
13C 1D (CP) SAA non seeded
13C 1D (CP) SAA non seeded with heparin
[rel]
8000
6000
4000
2000
0
150
100
50
[ppm]
13C (ppm)

C.

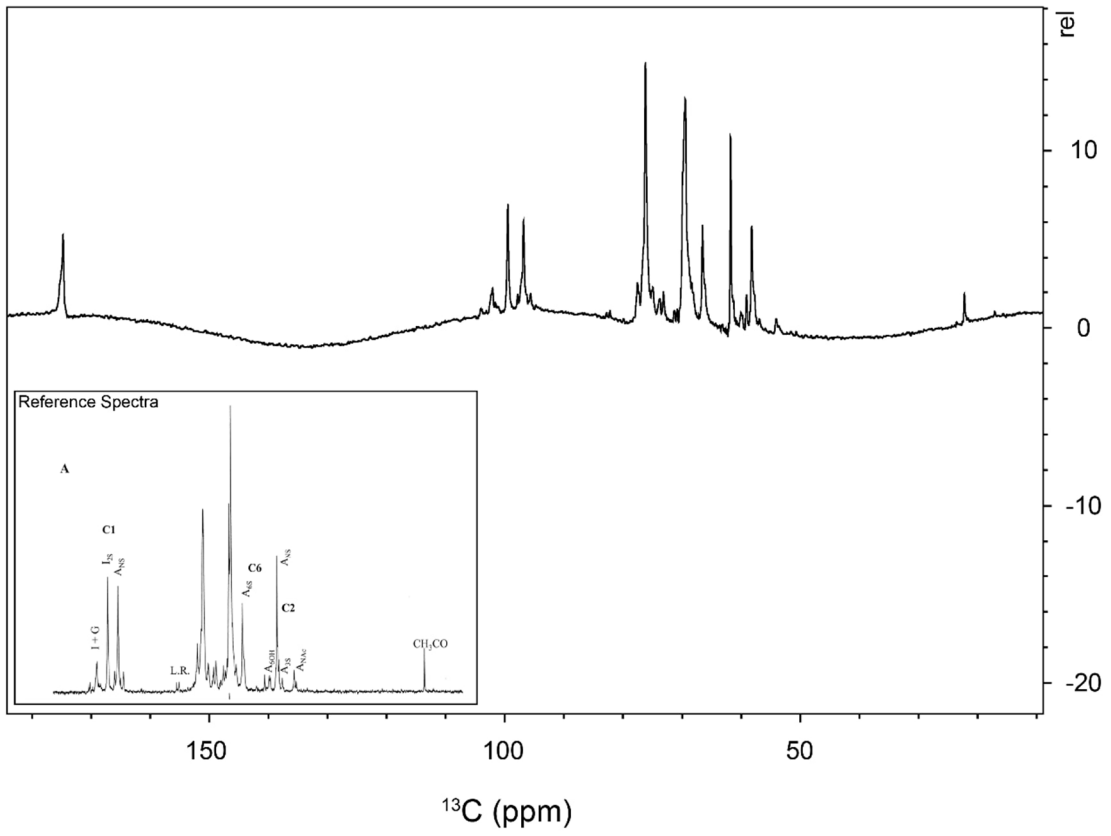
rel
10
0
-10
-20
Reference Spectra
A
C1
C6
C2
L.R.
CH3CO
150
100
50
13C (ppm)

D.

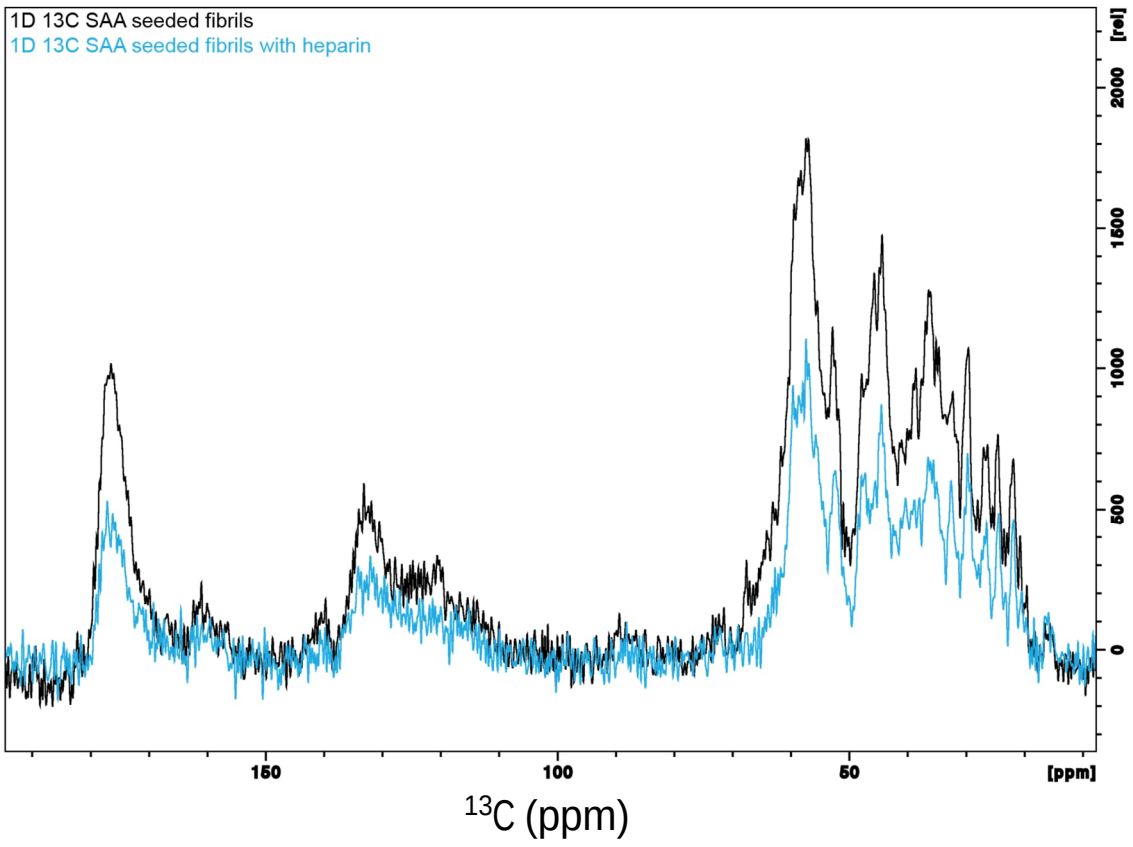
1D 13C SAA seeded fibrils
1D 13C SAA seeded fibrils with heparin
[rel]
2000
1500
1000
500
0
150
100
50
[ppm]
13C (ppm)

Figure 42. *1D spectra of SAA fibrils. A, Overlay of 13C direct spectra of non-seeded SAA fibrils in the presence (blue) and absence (black) of heparin. B, Overlay of 1D CP spectra of non-seeded SAA fibrils in the presence (blue) and absence (black) of heparin. C, 1 D 13 C spectra recorded by solution NMR for unlabelled Heparin only with 20k scans and reference spectra in the inset from labeled heparin [173]. D, Overlay of 1D CP spectra of seeded SAA fibrils in the presence (blue) and absence (black) of heparin. The fibrils were grown in the presence of heparin.*

The ^{13}C 1D spectrum does not show any heparin peak (figure 42 A). The cross-polarization spectra of the SAA fibrils with and without heparin were also compared, as shown in figure 42 B. However, no heparin peak was observed in the cross-polarization spectra as well. An isolated isoleucine peak (Cγ) in the ^{13}C-^{13}C correlation spectrum has an S/N of 4,39 for non-seeded SAA fibrils. For unlabelled heparin with an average molecular weight of 18 kDa (1% natural abundance), assuming 1:1 binding with protein should have a 6 times less S/N ratio for an isolated carbon peak in heparin. Therefore, it is highly possible that heparin peaks are not visible and are part of the noise. The results, as shown in the figure 42 B and D, display that SAA fibrils in the presence of heparin have lower S/N for both seeded and non-seeded fibrils. The observation suggests that heparin remains bound to the SAA fibrils, and lower S/N corresponds to less sample in the rotor. Since the S/N is less, the SAA fibrils prepared with heparin cannot be assigned using 3D ssNMR experiments. However, the amount of heparin bound to fibrils cannot be quantified with these experiments.

4.2.8 Mechanism involved in SAA fibrillation in presence of heparin

The amyloids are formed by the interaction of a protein with itself, resulting in insoluble protein aggregates. The fibrils can be formed after mutation, misfolding, or a biological component that promotes aggregation. It has been verified in previous studies that Aβ aggregates faster in the presence of membranes [174]. However, the reason behind enhancement in aggregation is difficult to deduce. Therefore, elucidating the molecular mechanism involved in the fibrillation process is crucial to understanding the aggregation and the disorders caused by the fibrils. Amylofit [167] is an online software developed to investigate the dominant molecular mechanism contributing the fibril formation using the results of the ThT kinetic assay.

The ThT kinetics of SAA were studied at different concentrations as a function of time. The resultant plots were uploaded on the Amylofit. The fitting of the curves for different concentrations of SAA is depicted in figure 43 A. The dominant mechanism responsible for SAA aggregation is unseeded secondary nucleation. The SAA fibrils can grow with the addition of secondary nuclei on the surface of fibrils which further elongates to form the mature fibrils. The fitting is performed globally over all the concentrations. The parameters for primary nucleation and elongation are shown in figure 43 B. The mean residual error for the fitting is 0.00413, which describes the goodness of the fit.

The plot for half-time for the SAA at different concentrations is shown in figure 44 A. The half-time plot is a linear curve with a scaling factor γ of -2.393. The linear curvature of half-time indicates that the dominant mechanism does not vary with the monomer concentrations. In addition, only a single dominant mechanism should be prevailing, and competition or supersaturation does not play any role in the aggregation process.

43 A.

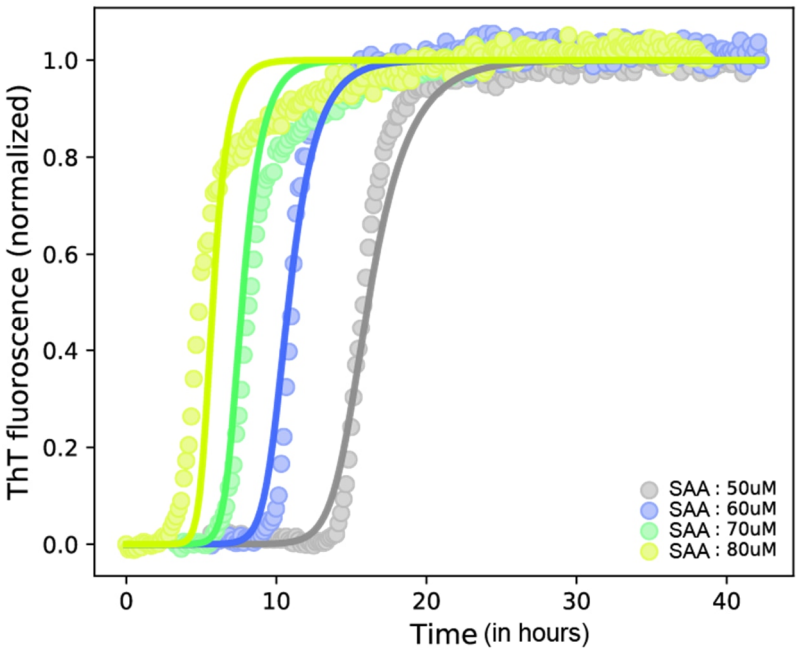

B.

Global parameters

k_+k_n = 2.95e+13

n_c = 4.94

k_+k_2 = 2.32e+18

n_2=3.31

Figure 43. *Fitting of curves using Amylofit (at constant rotation) A, the SAA aggregation kinetics at different concentrations in the absence of heparin using ThT fluorescence. The data are fit using amylofit. B, The fitting is performed with global parameters as described.*

The effect of heparin was determined by using a constant concentration of SAA and gradually adding the heparin. With the addition of heparin, the lag phase reduces drastically. However, further addition of heparin does not affect the lag phase after a certain concentration. The mechanism involved in the enhancement of fibrillation was studied using Amylofit. The ThT fluorescence curves were obtained from the ThT assay in the presence of heparin and were fitted with Amylofit. The fitted plots are shown in the figure 45 A.

44 A

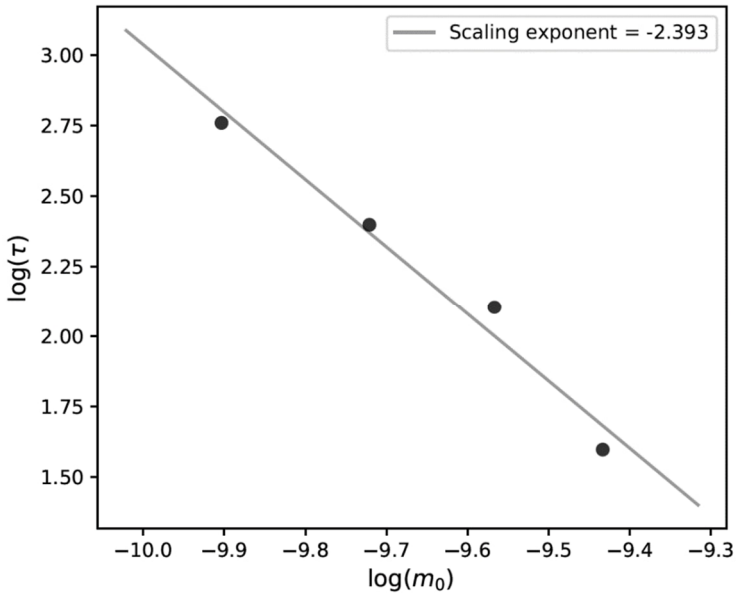

Function used:

log(tau) = a * log(m0) + b

a = -2.392900

b = -20.892265

Figure 44. *Half time obtained from Amylofit. A, the half-time plot attained from the ThT curves of SAA for different concentrations in Amylofit. The values of constants obtained from Amylofit are depicted in right.*

45 A.

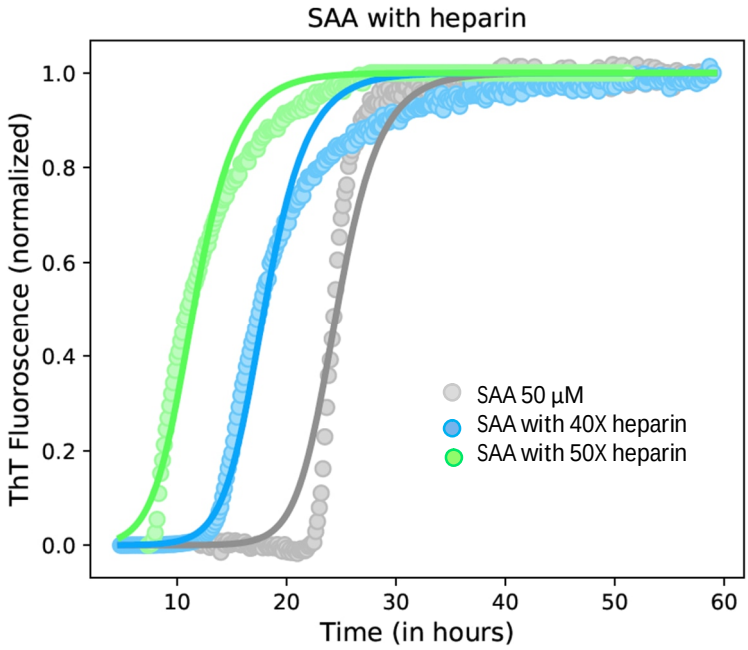

B.

Global parameters:

n_c = 1.87

k_2 = 2.77e9

n_2 = 2.00

k_+ = 3.08e+7

Fitted parameters

k_n = 7.62e-5 (0X heparin)

k_n = 0.00531 (40 X Hep)

k_n = 0.330 (50 X Hep)

Figure 45. *Fitting of ThT kinetics plots in presence of heparin at constant rotation using Amylofit. A, the fitting of ThT curves at different concentrations of heparin with amylofit. B, the global and fitted parameters obtained while fitting.*

The ThT plots follow the secondary nucleation dominant mechanism. The global parameters and their respective values are depicted in figure 45 B. The addition of heparin increases the primary nucleation rate of SAA. There is approx. 10^2 fold increase in primary nucleation rate

constant at the highest added heparin concentration. The amylofit fitting of the ThT curves proves that heparin enhances the primary nucleation of the SAA protein.

The ThT assay was repeated with more heparin concentrations. However, the experiment was repeated with intermittent rotation, which caused an increased lag time of aggregation. Nevertheless, the fitting of ThT curves yielded similar results and showed that heparin enhances the rate of primary nucleation, figure 46 A and B.

46 A.

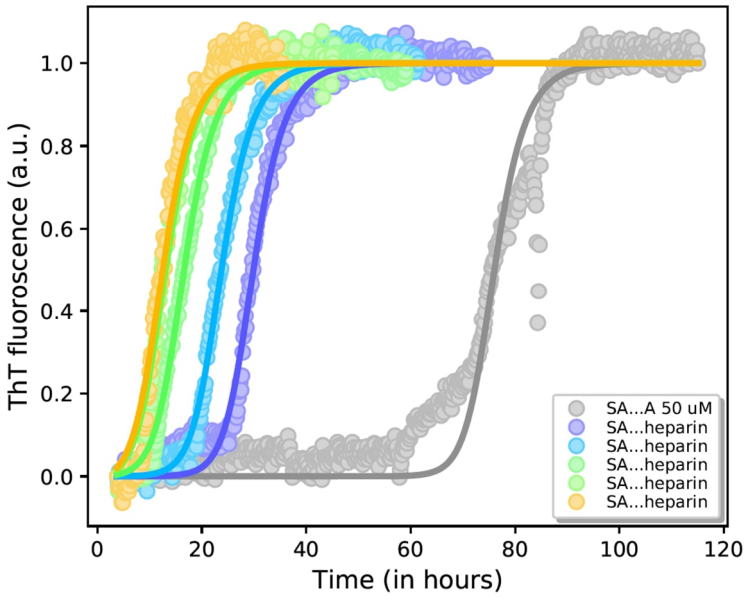

B.

Global parameters:

n_c = 1.87

k_2 = 2.77e9

n_2 = 2.00

k_+ = 3.08e+7

Fitted parameters

k_n = 1.77e-12 (0X heparin)

k_n = 0.000340 (30 X Hep)

k_n = 0.00428 (40 X Hep)

k_n = 0.828 (50 X Hep)

k_n = 0.360 (60 X Hep)

k_n = 0.454 (70 X Hep)

Figure 46. *Fitting of ThT kinetics plots in the presence of heparin with intermittent rotation using Amylofit. A, the fitting of ThT curves at different concentrations of heparin with amylofit. B, the global and fitted parameters obtained while fitting.*

The fitting of the ThT kinetic plots demonstrated the enhancement of the primary nucleation rate constant from 1.77e-12 to 3.4e-4 with adding 1.5 mM heparin. The primary nucleation rate constant further increases to 4.28e-3, 0.828, 0.360, and 0.454 at 2 mM, 2.5 mM, 3 mM, and 3.5 mM heparin concentration, respectively. The heparin at 2.5 mM shows the maximum primary rate constant value. With a further increase in heparin concentration, the k_n reduces. The mean residual error for the fitting is 0.00282, which describes the goodness of the fit.

4.2.9 Conclusion and Discussion

Amyloids are the cause of many life-threatening diseases and inspired many researchers to understand the structure and molecular mechanism behind aggregation. Various enhancers and inhibitors have been found in recent years, which are of great importance to deducing the importance of the underlying role of the biological components. Heparin is one of the most known enhancers, which increases aggregation. It has been verified that heparin enhances the aggregation for IAPP, AL amyloidosis, and many other amyloidogenic proteins

[128, 129]. The current project aimed to analyze the effect of heparin on SAA aggregation and its impact on the structure and mechanism of fibrillation.

The kinetics of SAA fibril growth is studied using the ThT assay, which concluded that Heparin enhances fibrillation for SAA protein. The lag time and half time reduce with the increase of heparin concentrations. Solid-state NMR was employed to deduce the impact of heparin on the structure of SAA fibrils.

The solid-state NMR investigation of seeded SAA fibrils proved that heparin does not affect the structure of SAA fibrils. The seeded fibrils studied using ssNMR are structurally similar to only one polymorph deduced from cryo-EM [175]. The seeded SAA fibrils grown in the presence of heparin have a similar structure as the seeded fibrils in the absence of heparin. However, in the presence of heparin, chemical shifts are observed for positively charged and their neighboring amino acids. In addition to chemical shifts, the splitting of peaks is also observed, for example, R18. The ssNMR and ThT assay results confirm that heparin interacts with and affect the aggregation process of SAA fibrils. The TEDOR spectra further proved that heparin stabilizes the SAA fibrils. The chemical shifts are observed for a few amino acids after titrating the pre-formed fibrils with heparin. The above result is attributed to the fact that the core of SAA fibrils is stabilized with salt bridges and hydrophobic interactions. Therefore, only a few side chains of charged residues are accessible to heparin. However, the presence of additional Cγ peaks in TEDOR spectra and an increase in the intensity of Cα peaks verify that heparin stabilizes the SAA fibrils. The results are in correspondence with the previous cryo-EM and ssNMR [27, 175] studies and suggest that one polymorph of SAA is more prevalent than the others and the extracted fibrils are more stable than the in vitro prepared fibrils.

The biophysical characterizations of SAA fibrils using CD and tryptophan fluorescence spectroscopy align with the solid-state NMR study. The SAA fibrils in the presence of heparin have minima at β-sheet conformer and have higher ellipticity. Furthermore, the spectrum for tryptophan fluorescence in the presence of heparin has higher intensity and is blue-shifted. The result verifies that SAA fibrils in the presence of heparin have more stable hydrophobic interactions and packed structure.

The structure of non-seeded fibrils is also similar in the presence and absence of heparin, as deduced using solid-state NMR. However, heparin reduces SAA fibrils' heterogeneity and allows only a few conformers. The TEM images of non-seeded SAA fibrils have many conformers with two or three protofilaments. On the contrary, in the presence of heparin, SAA fibrils with only two protofilaments can be formed. Since a chemical shift is observed at K24, which is crucial for stabilizing SAA fibril morphology with three and four protofilaments,

the SAA fibrils cannot form three protofilaments morphology in the presence of heparin. The TEM images are consistent with the observation of single peaks in the presence of heparin for multiple sets of peaks in the absence of heparin. The above-mentioned results suggest that heparin can be a reason for observing different polymorphs for fibrils extracted and *in vitro* prepared fibrils.

Secondary nucleation, unseeded, is the dominant molecular mechanism for SAA fibril formation, as deduced from the ThT kinetics assay. Adding heparin does not affect the dominant molecular process but affects the primary rate constant of the nucleation. The results obtained from fitting ThT curves using Amylofit prove that heparin enhances the nucleation of the SAA fibrils. The charged residues of SAA protein interact with heparin, allowing a local increase in the concentration of heparin. This augmented concentration of SAA leads to a faster aggregation process.

47 A.

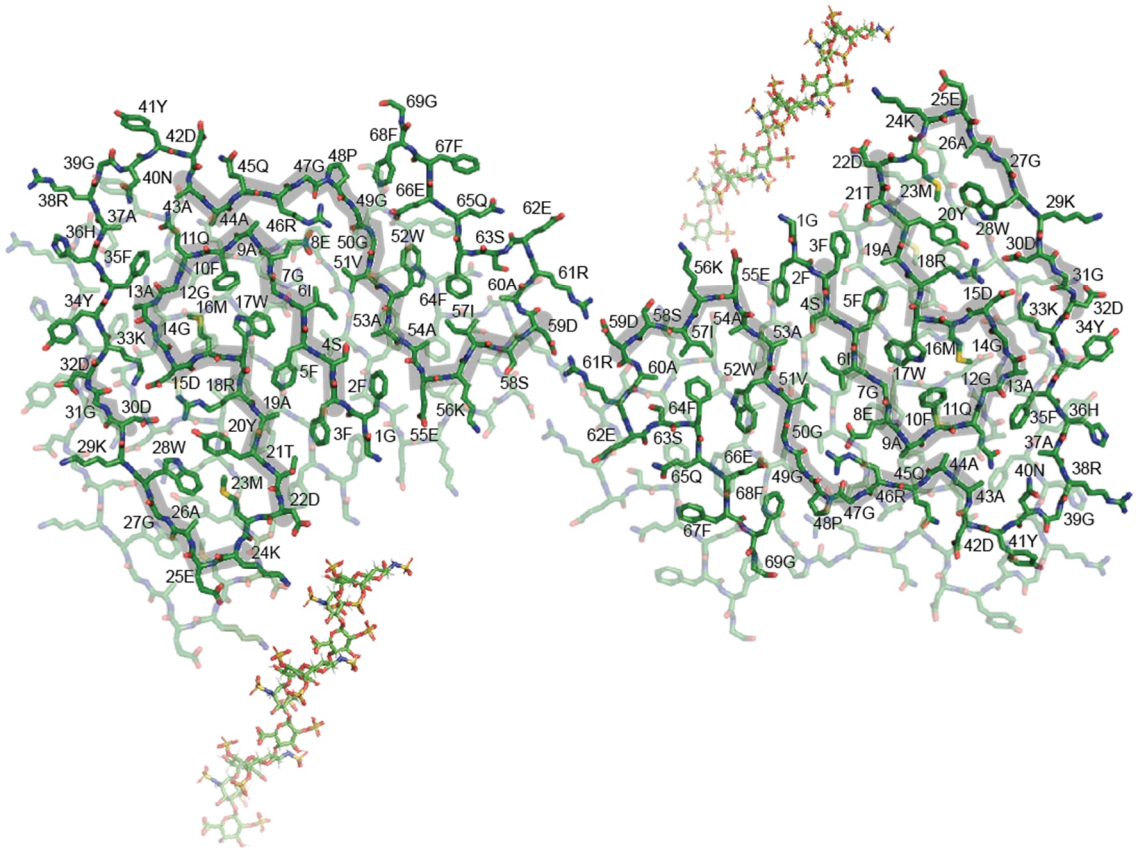

Figure 47. *Binding of heparin to SAA fibrils. A, proposed model of SAA binding to the solvent-accessible positively charged residue of SAA fibrils.*

The results mentioned above were attained from different biophysical characterization and structural studies; it can be hypothesized that heparin interacts with the SAA protein. The effect of heparin is a consequence of the interaction of negatively charged SO_4^{-2} with positively charged residues of SAA protein. The interaction leads to a local increase in the

concentration of SAA protein. Therefore, the rate of nucleation increases, hence the aggregation process. However, heparin only provides a platform for SAA to aggregate quickly; consequently, it does not affect the structure of SAA fibrils in the presence of seeds. The heparin remains attached to the side chains of positively charged residues accessible to the solvent. These heparin molecules caged the whole fibril structure, leading to more stable fibrils. The hypothesized interaction of heparin and SAA fibrils is shown in figure 47 A.

The basis of the structural polymorphism of amyloid fibrils is still not well understood. It has been reported that few morphologies are more prevalent than others. The SAA fibrils extracted from the mouse were reported to have three fibril morphologies. However, 95% of fibrils belong to a dominant morphology [176] which was solved using cryo-EM. Solid-state NMR studies using seeds extracted from mice have replicated similar fibril morphology. The seeded SAA fibrils attain the same morphology in the presence of heparin with minor chemical shifts at the positively charged residues. However, the trimeric fibril morphology, as observed in the SAA fibrils solved using cryo-EM, was not reproduced in vitro as well as in the presence of heparin. Hence, the effect of seeding is more on the structure of fibrils than heparin.

Additionally, trimeric and tetrameric morphology solved by cryo-EM for *in vitro* prepared fibrils were not observed in the presence of heparin. The interaction stabilizing the trimeric and tetrameric morphology of SAA fibrils involves K24. The DARR spectra for seeded and non-seeded SAA fibrils have depicted a chemical shift at K24 in the presence of heparin. These results suggest that cellular components can shield few amino acids of the protein, which leads to the unavailability of these residues for fibril formation. Therefore, the morphologies formed in the *in vitro* fibril formation are different from extracted fibrils. Moreover, the interaction can also affect the rate or mechanism of fibril formation, allowing one morphology to be more prevalent than others.

In the presence of seeds, the fibrils tend to organize in a structure similar to the seeds. However, the dominant morphology can be a consequence of the interaction of allowed amino acids which are not interacting with any other cellular component. The study put light on the importance of cellular components on the aggregation process and the molecular structure of fibrils. The fibrils are not only result of a sequence of protein but a complex interaction of cellular conditions, components, and interactions. The polymorphism of fibril structure can be attributed to the interaction of a protein and cellular components. The polymorphism is a result of only possible paths where protein can aggregate in the presence of cellular components and the condition of aggregation. The understanding of how the fibrils

are formed and only particular structure are allowed is possible by investigating the role of cellular components in the process of fibril formation.

4.3 Interaction of SAA with Lipids

4.3.1 SAA aggregation in presence of lipids

Lipids are one of the major constituents that co-precipitates with the fibrils. Therefore, the interaction of lipids and their effect on amyloidogenic protein is a topic of intense research. Previous studies have proven that lipids play a crucial role in the aggregation of fibrils. The lipids can enhance or inhibit aggregation. Different interaction and aggregation mechanisms were observed for lipid and amyloidogenic proteins. It has been proven that Aβ ruptures the cellular membrane and forms fibrils [177]. Lipids also enhance IAPP aggregation via the secondary nucleation pathway [178]. However, different amyloidogenic proteins behave differently in the presence of lipids. SAA is an apolipoprotein that plays a crucial role in lipid metabolism. Investigating the effect of lipids on the stability and aggregation of SAA provides an insight into the possible triggers for AA amyloidosis.

The ThT kinetics for SAA aggregation in presence of liposomes and nanodiscs were followed to determine the effect of lipids on SAA fibril formation. Figure 48 A depicts the aggregation kinetics of SAA at different concentrations and diameters of liposomes. Figure 48 B, describes the effect of nanodiscs on SAA aggregation kinetics in the presence and absence of seeds.

48 A. B.

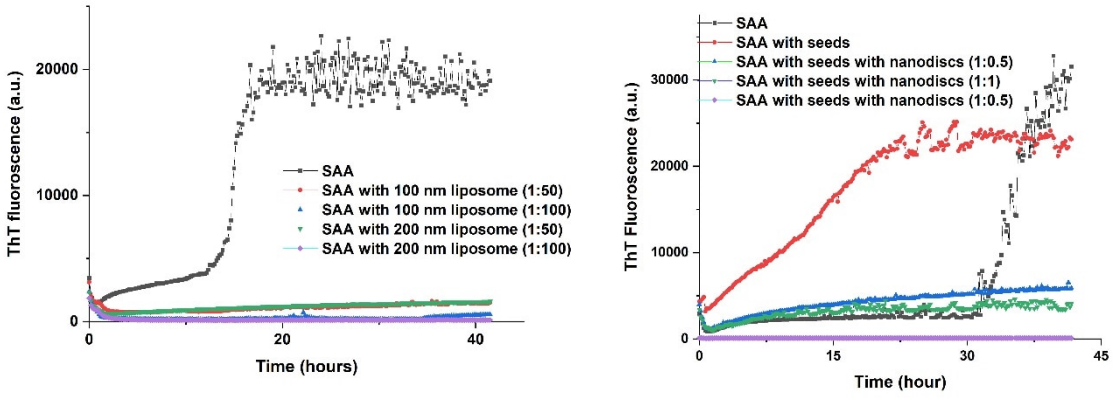

Figure 48. *SAA kinetics in presence of lipids. ThT assay A, in presence of liposomes at different concentrations and diameters and B, in presence of nanodiscs at different concentrations.*

The above figures conclude that lipids have inhibitory effect on SAA fibrillations. The POPC liposomes at all concentrations and diameters inhibit the SAA aggregation. In addition to it, nanodiscs can inhibit the seeding effects. As shown in figure 48 B, the SAA in the presence

of seeds does not have a lag phase, and the aggregation kinetics resume from the elongation phase. However, in the presence of nanodiscs, SAA does not aggregate and shows only a slight increase in fluorescence. Moreover, in the absence of seeds, ThT fluorescence does not show any increase in intensity.

The kinetics results are verified using Transmission Electron Microscopy. The TEM images, as shown in figure 49 A, display long thin fibrils in the absence of lipids. On the contrary, in the presence of nanodiscs, figure 49 B and C, only short aggregates or amorphous aggregates are formed. It has been verified that lipids inhibit the fibril formation of SAA. Various biophysical characterizations have been performed to elucidate the effect of lipids on SAA.

49 A. B. C.

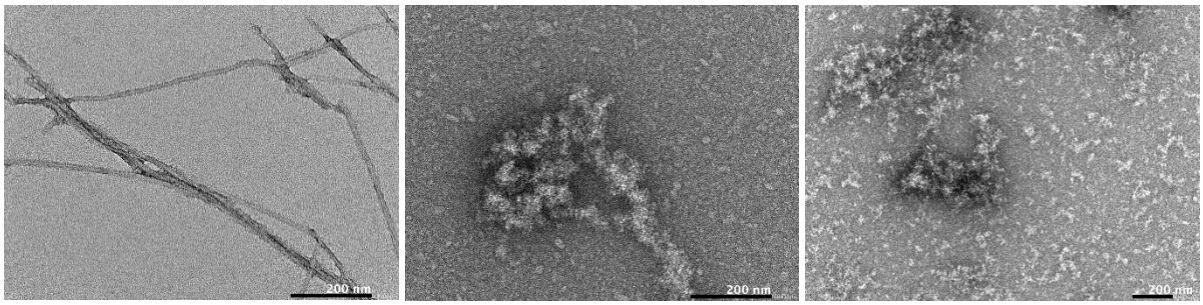

Figure 49. *EM images in presence of lipids. A, TEM image of SAA fibrils B and C, SAA in presence of nanodiscs.*

4.3.2 Binding of SAA with Nanodiscs

The pull-down assay was performed to verify whether SAA binds with Nanodiscs, which inhibits SAA aggregation, or it is merely a crowding effect. Additionally, the pull-down assay can confirm whether SAA disintegrates the nanodiscs and bind only with lipids or if MSP remains bound to Nanodiscs.

The experiment was performed with His-tagged nanodiscs and pure SAA without any tag. Only His-tagged protein can remain bound to the Ni-beads. The bound protein will remain in the sediment while the unbound protein will stay in the supernatant.

The pure SAA was added to his-tagged preformed nanodiscs. The construct was used to perform a pull-down assay where it was incubated with Ni-beads. Since only MSP is His-tagged, only nanodiscs or any protein-bound to nanodiscs will be observed in the precipitate. As depicted in the gel image in figure 50 A, both SAA and MSP are present in the sedimented fraction with the nickel beads.

The result proves that SAA binds with the nanodiscs. In addition, SAA does not disintegrate nanodiscs or remove MSP protein from the nanodisc structure.

The SAA and MSP proteins are also observed in the supernatant. This could be from the higher concentration used, which surpasses the binding capacity of the Nickel beads.

50 A.

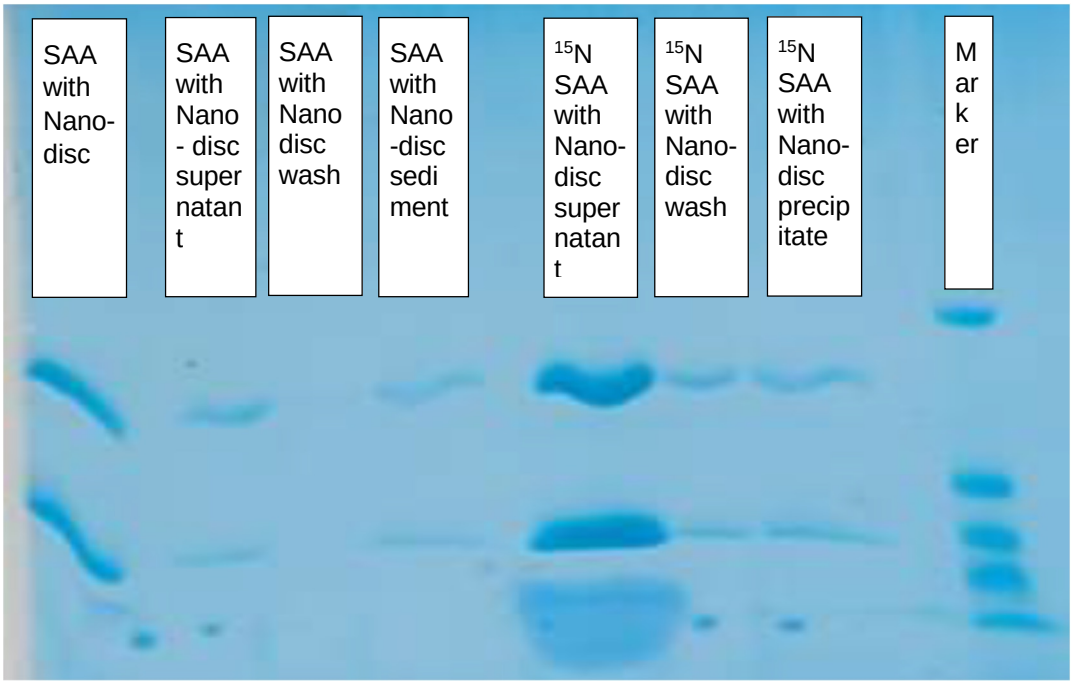

Figure 50. *Pull down assay using His-tagged nanodiscs. A, the gel image depicting the different fractions obtained from pull down assay. The supernatant as well as the precipitate shows both SAA and MSP. The control of SAA and MSP is run in the first well to compare the results.*

4.3.3 Effect of lipids on the stability of SAA

SAA is unstable protein at higher temperatures. It has been established in the previous section that SAA has an alpha-helical secondary structure at lower temperatures and attains random coil at higher temperatures, using CD spectroscopy. Therefore, CD spectroscopy was utilized to determine the effect of lipids on the secondary structure of SAA.

SAA was incubated with different concentrations of liposomes, and their CD spectra were recorded at 25^{o}C. As depicted in Figure 51 A, SAA has a random coil structure at room temperature. However, in the presence of liposomes, SAA has an alpha-helical structure at room temperature instead of a random coil.

With the addition of liposomes from 1 mM to 2 mM, the intensity of the CD signal increases. On the contrary, further increasing the liposome concentration to 4 mM reduces the CD

signal intensity. The decrease in the CD signal intensity can be attributed to the tendency of liposomes to coalesce and form larger liposome-like entities.

The CD spectra in the presence of liposomes confirm that lipids stabilize the SAA and keep it in its alpha-helical secondary structure.

51 A.

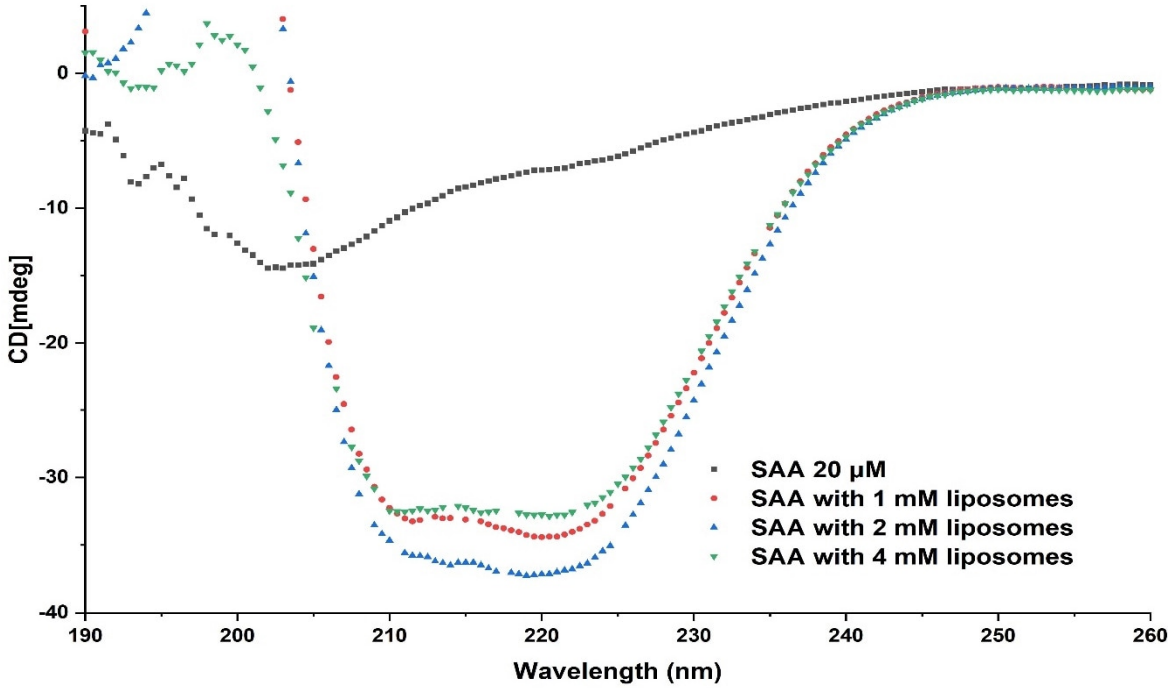

Figure 51. *CD spectra in presence of liposomes. A, CD spectrum of SAA (black) depicting its random coil structure at room temperature and alphal helical structure of SAA in presence of liposomes at 1mM (red), 2 mM (blue), and 4mM (green) concentration, respectively.*

Furthermore, the thermal unfolding of SAA was performed using the CD spectrometer. The thermal scans of SAA in the presence and absence of liposomes were recorded with a temperature range of 4°C to 90°C at 220 nm wavelength.

The SAA in the buffer is unstable and has a melting temperature of around 17°C. After the addition of liposomes, the stability of SAA increases, and the melting temperature increases to approximately 49 °C. However, the concentration of liposomes does not affect the melting temperature. Therefore, the melting temperature of SAA is approximately the same at 1:10 (48.8 °C) and 1:100 (48.5 °C) SAA to liposome molar ratio (Figure 52 A).

The secondary structure characterization and thermal unfolding using CD spectroscopy have confirmed that lipids stabilize the SAA protein and do not allow it to unfold. Therefore, it can be deduced that while SAA is bound to lipids, it remains stable at the human body temperature. Therefore, at healthy physiological temperature and conditions, SAA should not unfold and undergo fibril formation.

52 A

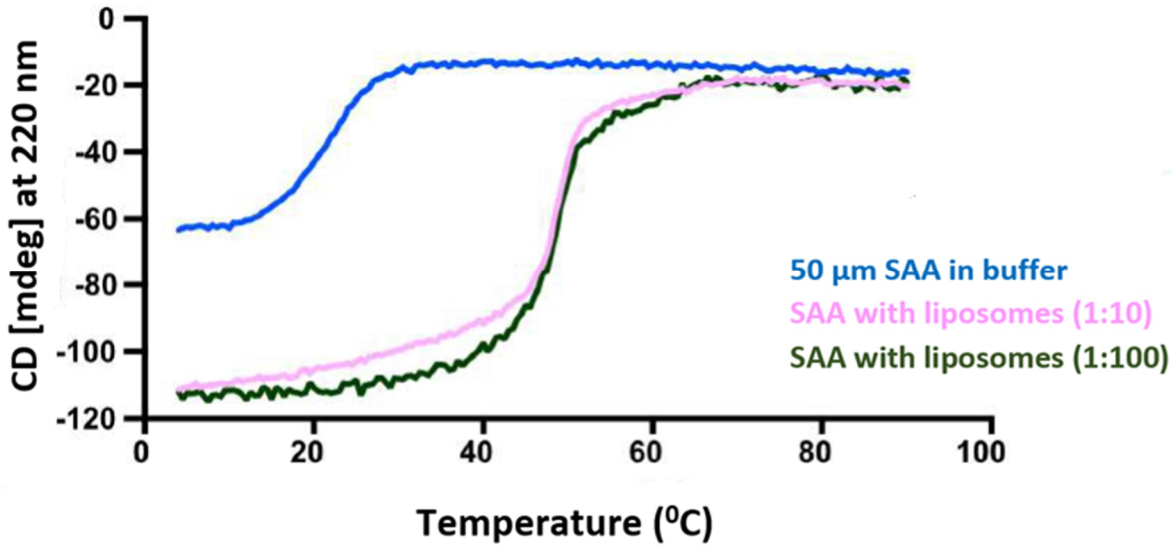

Figure 52. *The thermal scan of SAA from* 4°C to 90°C at 220 nm*. A, thermal melting curve of SAA (blue), and in presence of POPC liposome at 1:10 (pink), and 1:100 (green) molar ratio.*

Moreover, the interaction of SAA and lipids was investigated using nanodiscs (ND). The alpha-helical secondary structure of nanodiscs originates from MSP protein. These nanodiscs are very stable and maintain their secondary structure higher temperatures. Hence, nanodiscs should display an alpha-helical secondary structure in CD spectra at physiological temperature. To deduce the SAA-nanodisc complex, CD spectra of nanodiscs were recorded in the presence and absence of SAA.

53 A.

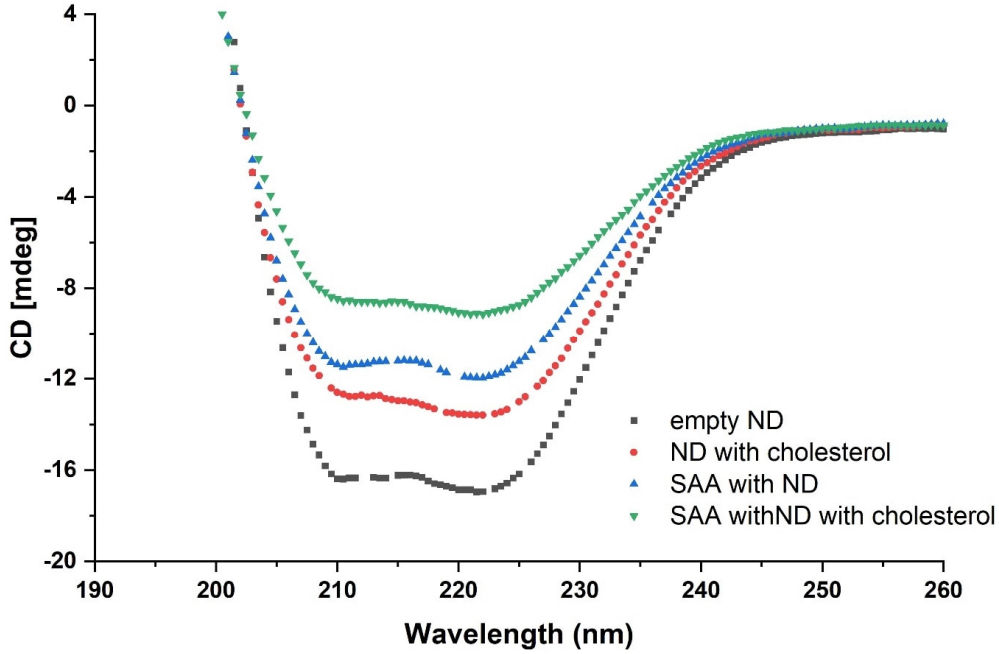

Figure 53. *CD spectra of nanodiscs. A, the CD spectrum of empty nanodiscs with cholesterol (red) and without cholesterol (black) depicting its alpha-helical structure and decrease in intensity after adding SAA in ND (blue) and with cholesterol (green).*

As depicted in figure 53, empty lipid nanodiscs and nanodiscs with cholesterol have alpha-helical secondary structure at room temperature. The intensity of the CD signal decreases after adding SAA to the nanodiscs. It is interesting to note that nanodisc with cholesterol has a higher decrease in CD signal intensity as compared to only nanodisc after adding SAA.

The above results prove that lipids stabilize the SAA protein. However, the effect of SAA on lipid entities like liposomes and nanodisc is not apparent. The CD spectra showed that the secondary structure of nanodiscs does not change with the addition of SAA, only the intensity of the CD signal decreases for the nanodisc and SAA complex.

4.3.4 The influence of lipids on the structure of SAA

As demonstrated in above sections that lipids bind to SAA and stabilize it. Simultaneously SAA also has an effect on nanodiscs and liposomes. Fluorescence spectroscopy, NMR, and electron microscopy were utilized to understand the underlying mechanism.

The tryptophans are sensitive to their environment, and emitted fluorescence from tryptophan display a blue or red shift or intensity deviation for any change in the tryptophan's environment (e.g., folding or unfolding of a protein). The phenomenon was employed to investigate the effect of lipids on the SAA. The lipids do not have any tryptophan; therefore, the fluorescence spectroscopy in the presence of liposomes depicts the effect on tryptophan's environment in SAA.

As depicted in figure 54, the fluorescence spectrum shifts to a lower wavelength in the presence of liposomes. The behavior is known as blue shift and attributes to the more hydrophobic tryptophan environment. The fluorescence spectrum confirms that the non-polar amino acids (tryptophan) interact with lipids.

The SAA protein has a fluorescence emission maximum of around 345 nm. With the addition of liposomes, the fluorescence maxima are blue-shifted to around 325 nm. The concentration of added liposome does not affect the shift in the fluorescence maxima. The fluorescence maximum for SAA to liposomes at 1:50 is the same as SAA to liposomes at 1:100. However, there is a slight shift to a lower wavelength at SAA to liposomes at 1:200.

54 A.

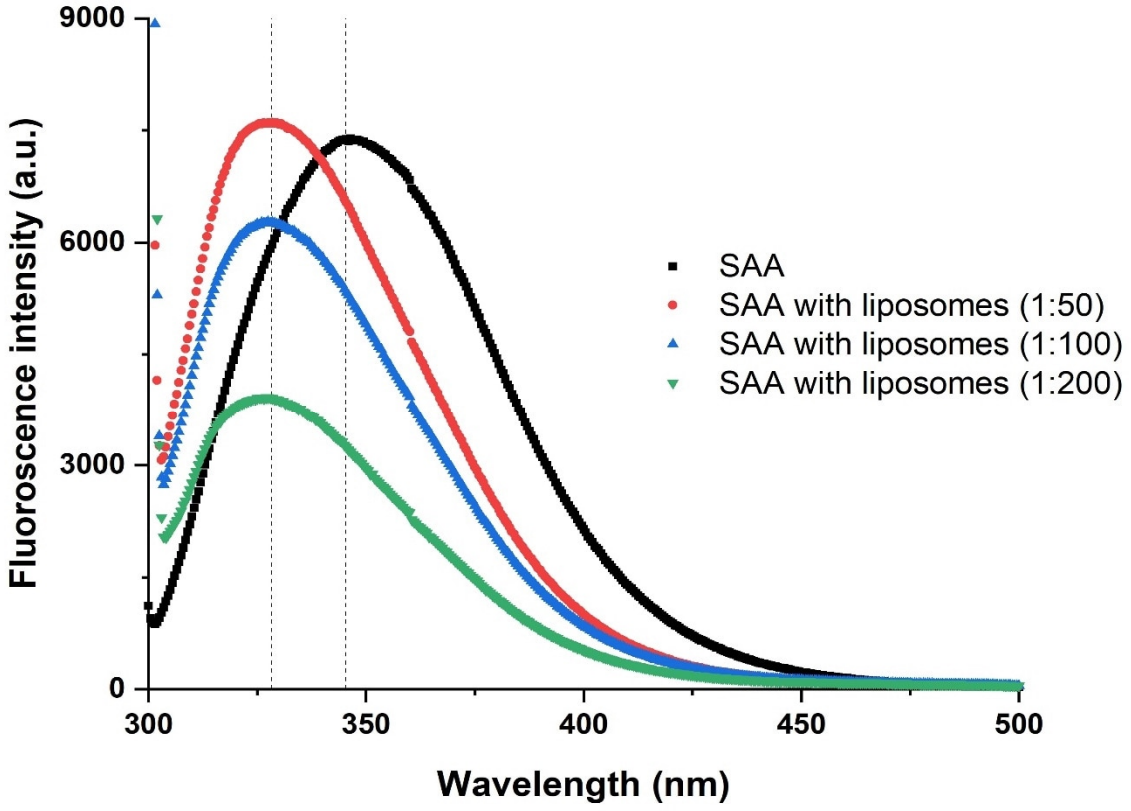

Figure 54. *Fluoroscence spectra of SAA with liposomes. A, the fluorescence emission of SAA (black), SAA with liposomes 1:50 (red), 1:100 (blue), and 1:200 (green).*

In addition to the effect of lipids on SAA, SAA also affects the structure of nanodiscs. The nanodiscs are lipids bilayers screened by the membrane scaffolding protein (MSP). Nanodiscs are homogenous, structurally similar to HDL, and highly stable. MSPs are amphipathic proteins and a modified version of apolipoprotein A with two tryptophans. These tryptophans were utilized to perform tryptophan fluorescence on nanodisc and SAA interaction. The fluorescence spectroscopy was performed for nanodiscs in the presence and absence of SAA, as depicted in figure 55. The tryptophan emission for nanodiscs shows a slight blue shift after adding SAA. However, the fluorescence emission intensity for nanodiscs decreases in the presence of SAA. A similar result is observed in the presence of cholesterol.

The lipids create a more non-polar environment for the SAA. Therefore, a blue shift in tryptophan fluorescence is observed. However, the precise reason for the decrease in tryptophan fluorescence intensity is unknown. The SAA-nanodisc complex requires further investigation to understand their effect on each other.

55 A.

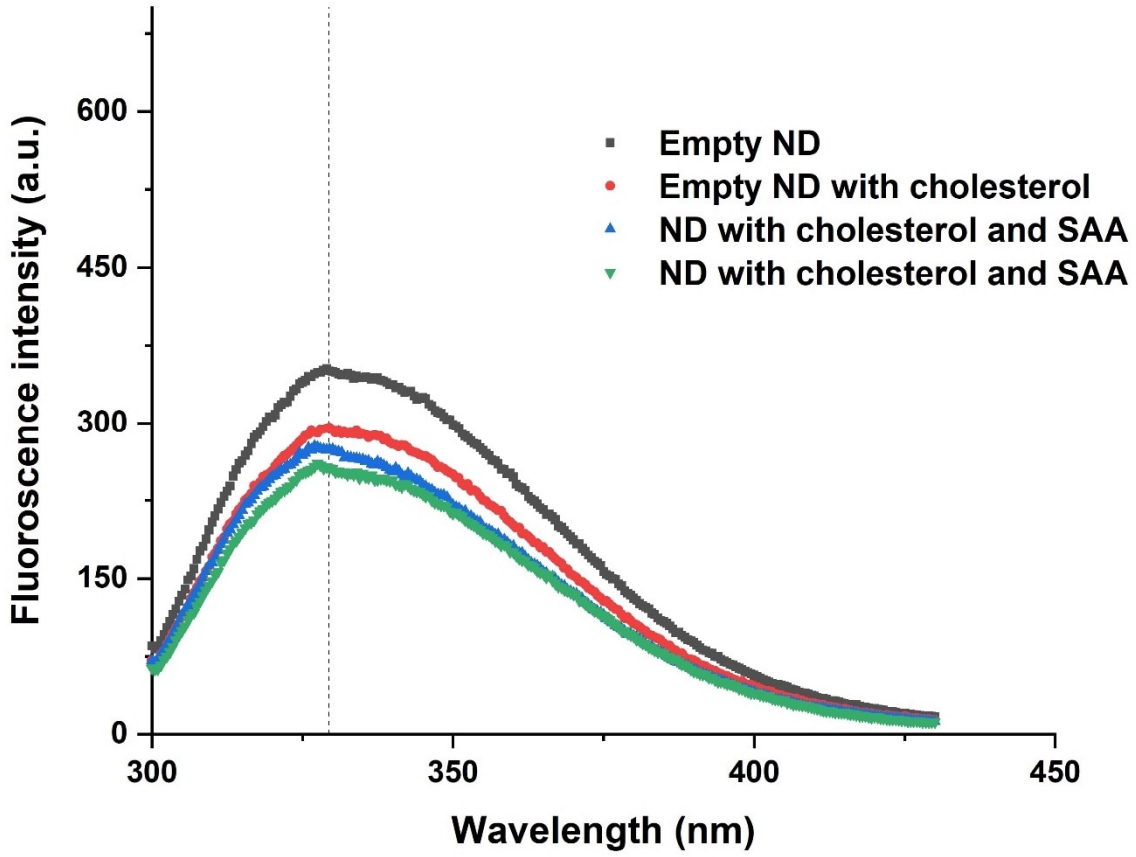

Figure 55. *Fluoroscence spectra of nanodiscs with SAA. A, the fluorescence emission of empty POPC nanodiscs (black), empty POPC-cholesterol nanodiscs (red), POPC nanodiscs with SAA (blue), and POPC-cholesterol nanodiscs with SAA (green).*

4.3.5 The structural study of SAA with nanodiscs

NMR spectroscopy was utilized to investigate the SAA-nanodiscs complex. First, the purified SAA is incubated with prepared nanodiscs at 4°C overnight. Then, the incubated complex is purified with size exclusion chromatography. The resulting SAA-nanodiscs complex in a buffer is a clear solution without any trace of precipitation, unlike the SAA solution in the buffer at room temperature.

The NMR spectroscopy was performed at 4°C to compare the NMR spectra of SAA in the presence and absence of nanodiscs. The temperature was chosen to keep the SAA stable, as discussed in the previous section (Section 4.1.1). The ^{1}H-^{15}N (HSQC) correlation shows around 90 peaks from the 103 peaks of the SAA protein, as shown in figure 56 A. In addition, the three distinct peaks of tryptophans are visible, which infer stable, folded SAA protein. However, there are no peaks observed for nanodiscs reconstituted with SAA, as shown in figure 56 B. A similar NMR spectrum was observed for SAA with liposomes, as

displayed in figure 56 C, where only side chains are visible. The results from NMR infer that SAA with lipids is a large complex that cannot be studied using solution NMR.

Electron microscopy was performed to elucidate the NMR results and SAA-lipids complex. TEM images for empty nanodiscs and nanodiscs reconstituted with SAA were recorded. The TEM images of empty nanodiscs show highly structured 7-8 nm round discs-like structures, as shown in figure 57 A. However, nanodiscs incubated with SAA are slightly larger and clumped together, as depicted in Figures 57 B and C. The nanodiscs have distorted shape in some places. However, nanodiscs stick together and form a huge assembly. This assembly can attribute to the loss of peaks in solution NMR

56 A.

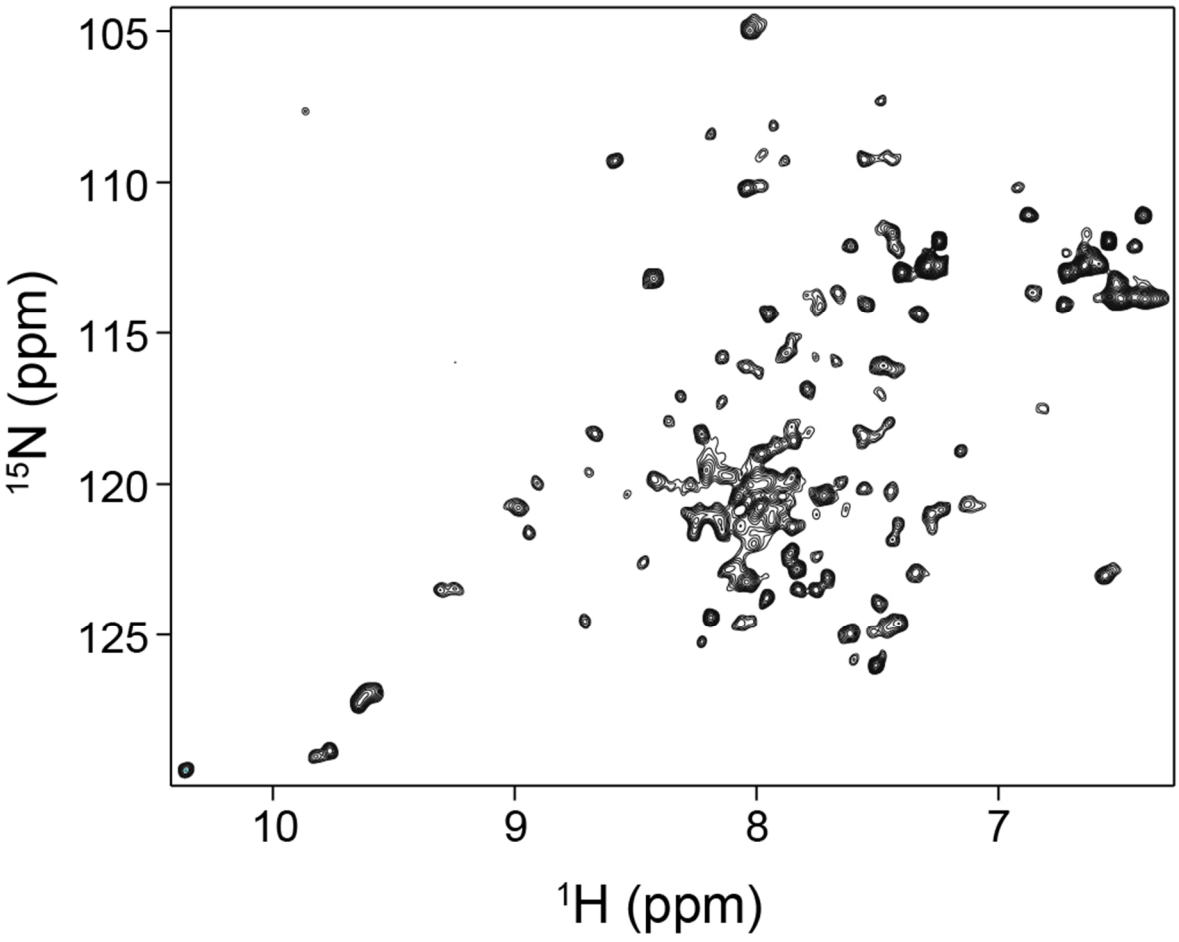

B. C.

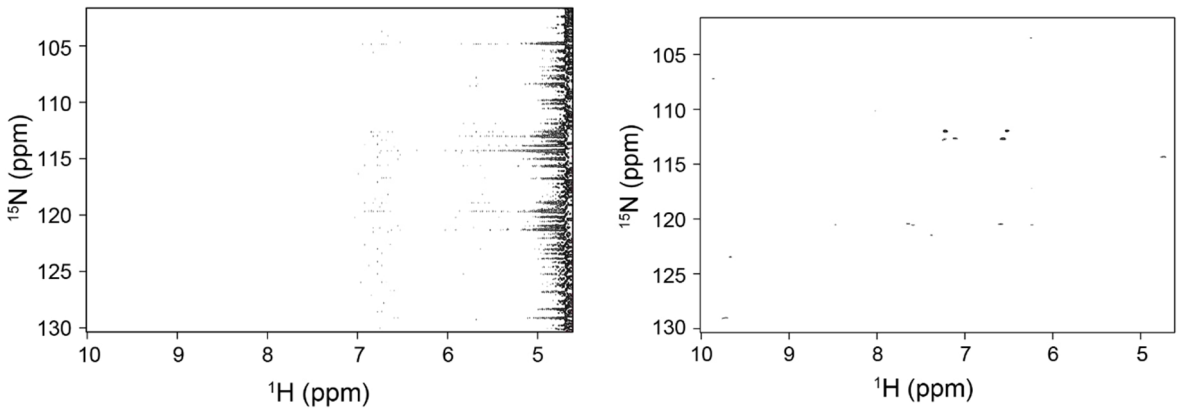

Figure 56. *NMR Spectroscopy of SAA. A, ^{1}H-^{15}N HSQC of SAA at 4^{o}C in the buffer. B and C, ^{1}H-^{15}N HSQC of SAA-nanodisc complex and SAA with liposomes, respectively.*

Furthermore, TEM images of empty liposomes and liposomes with SAA were observed. The empty liposomes are circular vesicle-like structures. The empty liposomes were incubated with SAA at 37^{o}C, and the TEM images were recorded.

The SAA without any liposomes assembled into fibrils as displayed in figure 57 G. However, the SAA incubated with liposomes does not make fibrils, and the size of liposomes increases. There are fewer fibril structures that can be observed for SAA incubated with liposomes.

In addition, SAA was incubated with heparin, and liposomes and TEM images were recorded. In the presence of heparin, SAA forms fibrils irrespective of the presence of liposomes. However, the fibrils are short and come out of liposomes. While in the absence of liposomes, SAA incubated with heparin assembles in long fibrils, figure 57 I.

57 A. Empty Nanodiscs B. Nanodiscs with SAA

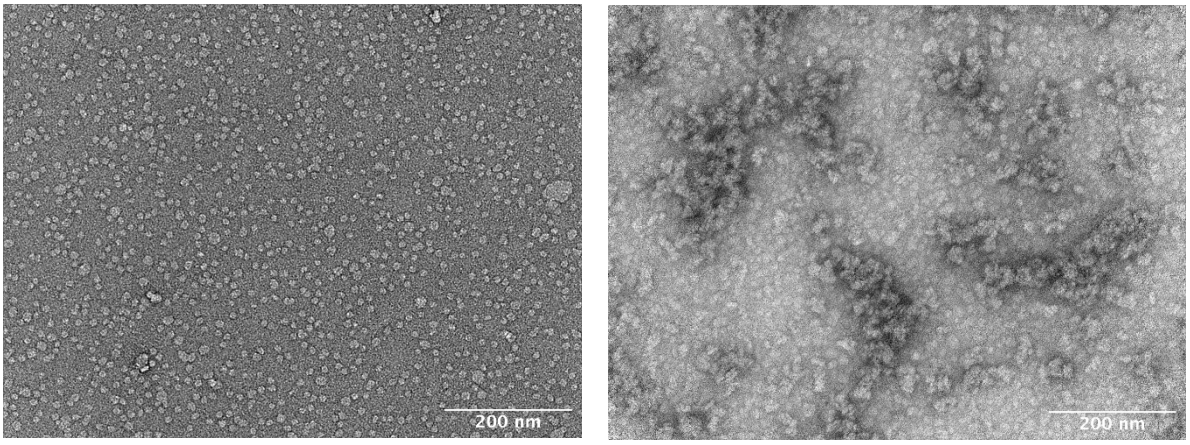

C. Nanodiscs with SAA

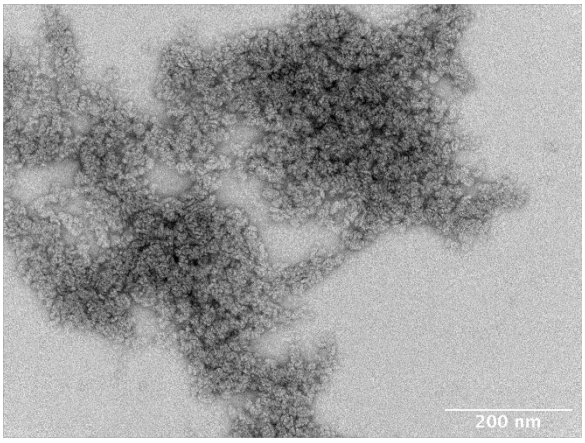

D. Empty liposomes

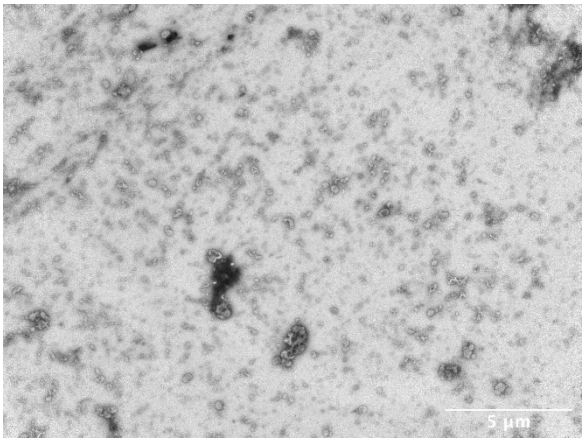

E. Liposome with SAA 37ºC

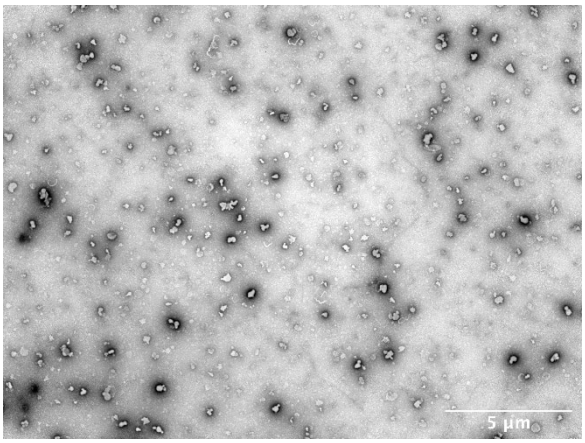

F. Liposomes with SAA at 37ºC

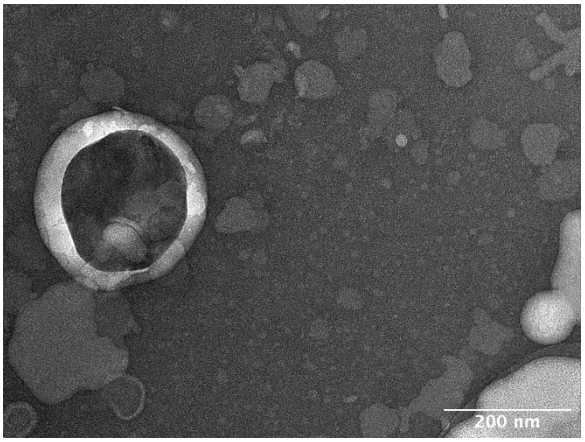

G. SAA incubated at 37ºC

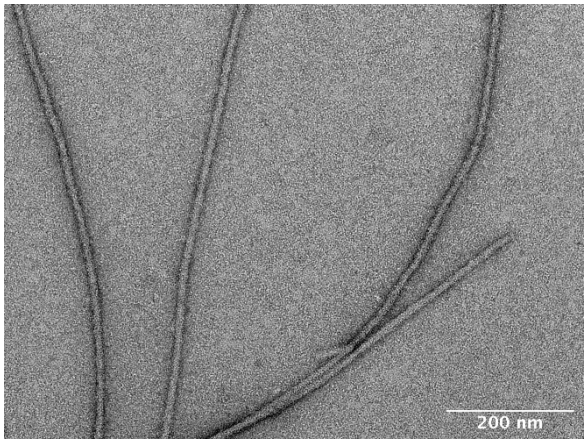

H. SAA incubated with heparin at 37ºC

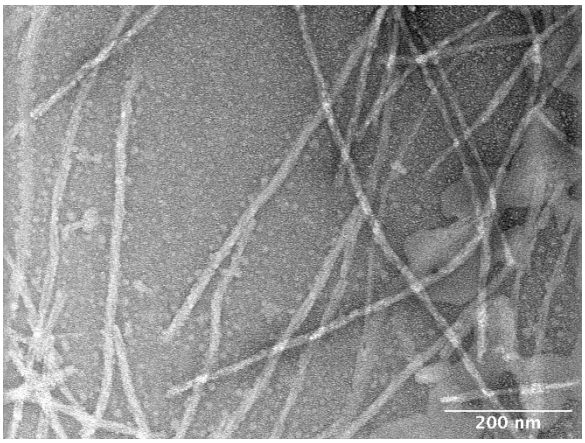

I. SAA incubated with liposomes and heparin at 37°C

J. SAA incubated with liposomes and heparin at 37°C

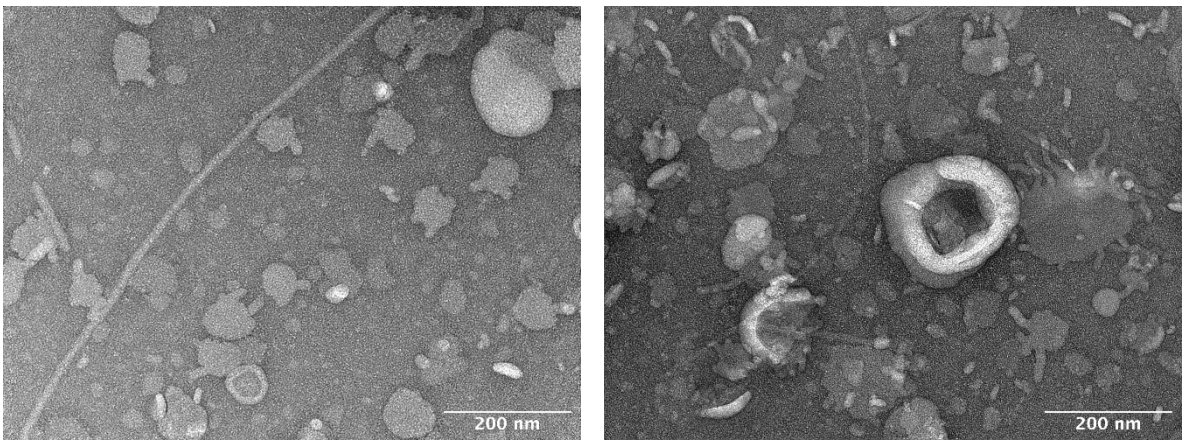

Figure 57. *TEM Images of SAA. A, Empty nanodiscs after purification. B and C, SAA-nanodisc complex after gel filtration. D, Empty liposomes prepared with Hamilton syringe. E and F, Liposomes incubated with SAA at 37°C. G and H, SAA fibrils formed after incubation at 37°C in the absence and presence of heparin, respectively. I and J, SAA incubated with liposomes and heparin at 37°C.*

4.3.6 Conclusion and Discussion

The current study demonstrates that lipids stabilize the SAA and do not allow it to assemble into fibrils. The biophysical studies like CD and fluorescence spectroscopy established that SAA is a helical, stable protein in the presence of lipids. The stability of SAA can be attributed to hydrophobic interaction with lipids, as depicted in the blue shift in the fluorescence spectrum (Figure 54 A). The melting temperature of SAA also increases to approx. 50°C from 15°C in the presence of lipids.

Nanodiscs are stable bilayer assembly of phospholipids. These are novel tools to study the structure and function of membrane proteins for their proven advantages over detergents and liposomes [179]. The structure and function of various membrane proteins have been elucidated using nanodiscs [180, 181]. Nanodiscs reconstituted with SAA were employed to study the structure of SAA. However, the SAA-nanodisc complex assembly was not visible in solution-NMR. It is possible that SAA reconstituted nanodiscs make a massive aggregate-like structure that cannot be visualized using solution NMR. The TEM images verify the findings from NMR. The clump-like assembly was observed for the nanodiscs reconstituted with SAA. Interestingly, the diameter of nanodiscs increases, and distortion appears in the nanodiscs after reconstitution with SAA. The addition of SAA to nanodiscs affects their behavior.

Similar results were obtained for liposomes. Liposomes do not allow SAA to make fibrils (figure 48 A) and keep SAA in an alpha-helical structure (figure 51 A). However, only peaks for side chains are visible in HSQC for SAA sample incubated with liposomes (figure 56C).

The TEM images of SAA with liposomes show that the diameter of liposomes increases (figure 57 E). Furthermore, TEM images were recorded for SAA for the fibril formation process. SAA without any lipid counterpart forms long fibrils. However, in the presence of liposomes only a few short fibrils are observed. With the addition of heparin to SAA in the presence of liposomes, more fibrils are formed. The images in figure 57 I and J, confirmed that heparin could induce fibril formation in the presence of lipids. Previous study on SAA had proved that it remodels lipids and make nanoparticle size lipoprotein when incubated with lipids [120]. Therefore, there is a possibility that SAA remodels the lipids in nanodiscs and liposomes, as depicted in the fluorescence spectroscopy and TEM images. The distorted structure of nanodiscs and increase in the diameter of nanodiscs and liposomes can be attributed to the interaction of lipids with SAA. However, the exact mechanism cannot be elucidated with the obtained results. The above results prove that lipids inhibit the aggregation of SAA and stabilize the protein in the buffer. The presence of lipids *in vivo* does not allow SAA to aggregate. However, the *in vivo* structure of SAA in the presence of lipids cannot be studied using solution NMR. Therefore, the SAA-lipid complex should be explored more in detail using solid-state NMR to annotate the structure of SAA.

5. References

1. Haschemeyer, A.E.V., *Kinetic Analysis of Synthesis and Secretion of Plasma Proteins in a Marine Teleost.* Journal of Biological Chemistry, 1973. **248**(5): p. 1643-1649.
2. Anfinsen, C.B., *Principles that govern the folding of protein chains.* Science, 1973. **181**(4096): p. 223-30.
3. Roth, C.M., B.L. Neal, and A.M. Lenhoff, *Van der Waals interactions involving proteins.* Biophys J, 1996. **70**(2): p. 977-87.
4. Dill, K.A., *Dominant forces in protein folding.* Biochemistry, 1990. **29**(31): p. 7133-55.
5. Makhatadze, G.I. and P.L. Privalov, *Energetics of protein structure.* Adv Protein Chem, 1995. **47**: p. 307-425.
6. Nick Pace, C., J.M. Scholtz, and G.R. Grimsley, *Forces stabilizing proteins.* FEBS Lett, 2014. **588**(14): p. 2177-84.
7. Go, N., *The consistency principle in protein structure and pathways of folding.* Adv Biophys, 1984. **18**: p. 149-64.
8. Lin, B.C., et al., *A conformational switch in nuclear hormone receptors is involved in coupling hormone binding to corepressor release.* Mol Cell Biol, 1997. **17**(10): p. 6131-8.
9. Jones, P.M. and A.M. George, *The Switch and Reciprocating Models for the Function of ABC Multidrug Exporters: Perspectives on Recent Research.* Int J Mol Sci, 2023. **24**(3).
10. Filipek, S., *Molecular switches in GPCRs.* Curr Opin Struct Biol, 2019. **55**: p. 114-120.
11. Browning, K.S. and J.M. Clark, Jr., *Translation initiation site of the coat protein messenger ribonucleic acid of the cowpea strain of tobacco mosaic virus.* Biochemistry, 1980. **19**(25): p. 5922-6.
12. Widmann, M. and P. Christen, *Differential effects of molecular chaperones on refolding of homologous proteins.* FEBS Lett, 1995. **377**(3): p. 481-4.
13. Azem, A., et al., *The protein-folding activity of chaperonins correlates with the symmetric GroEL14(GroES7)2 heterooligomer.* Proc Natl Acad Sci U S A, 1995. **92**(26): p. 12021-5.
14. Bohley, P., *The fates of proteins in cells.* Naturwissenschaften, 1995. **82**(12): p. 544-50.
15. Chiti, F. and C.M. Dobson, *Protein Misfolding, Amyloid Formation, and Human Disease: A Summary of Progress Over the Last Decade.* Annu Rev Biochem, 2017. **86**: p. 27-68.

16. Soto, C., *Unfolding the role of protein misfolding in neurodegenerative diseases.* Nat Rev Neurosci, 2003. **4**(1): p. 49-60.
17. Riek, R. and D.S. Eisenberg, *The activities of amyloids from a structural perspective.* Nature, 2016. **539**(7628): p. 227-235.
18. Eanes, E.D. and G.G. Glenner, *X-ray diffraction studies on amyloid filaments.* J Histochem Cytochem, 1968. **16**(11): p. 673-7.
19. Glenner, G.G., et al., *Beta-pleated sheet fibrils. A comparison of native amyloid with synthetic protein fibrils.* J Histochem Cytochem, 1974. **22**(12): p. 1141-58.
20. Stoppini, M. and V. Bellotti, *Systemic amyloidosis: lessons from beta2-microglobulin.* J Biol Chem, 2015. **290**(16): p. 9951-8.
21. Tasaki, M., et al., *Age-related amyloidosis outside the brain: A state-of-the-art review.* Ageing Res Rev, 2021. **70**: p. 101388.
22. Tjernberg, L.O., et al., *Transmissible amyloid.* J Intern Med, 2016. **280**(2): p. 153-63.
23. Nichols, M.R., et al., *Amyloid-beta protofibrils differ from amyloid-beta aggregates induced in dilute hexafluoroisopropanol in stability and morphology.* J Biol Chem, 2005. **280**(4): p. 2471-80.
24. Petkova, A.T., et al., *Self-propagating, molecular-level polymorphism in Alzheimer's beta-amyloid fibrils.* Science, 2005. **307**(5707): p. 262-5.
25. Matiiv, A.B., et al., *Structure and Polymorphism of Amyloid and Amyloid-Like Aggregates.* Biochemistry (Mosc), 2022. **87**(5): p. 450-463.
26. Acquasaliente, L. and V. De Filippis, *The Role of Proteolysis in Amyloidosis.* Int J Mol Sci, 2022. **24**(1).
27. Bansal, A., et al., *AA amyloid fibrils from diseased tissue are structurally different from in vitro formed SAA fibrils.* Nat Commun, 2021. **12**(1): p. 1013.
28. Karamanos, T.K., A.P. Kalverda, and S.E. Radford, *Generating Ensembles of Dynamic Misfolding Proteins.* Front Neurosci, 2022. **16**: p. 881534.
29. Ball, K.A., et al., *Homogeneous and heterogeneous tertiary structure ensembles of amyloid-beta peptides.* Biochemistry, 2011. **50**(35): p. 7612-28.
30. Bondos, S.E., A.K. Dunker, and V.N. Uversky, *Intrinsically disordered proteins play diverse roles in cell signaling.* Cell Commun Signal, 2022. **20**(1): p. 20.
31. Ayyadevara, S., et al., *Intrinsically disordered proteins identified in the aggregate proteome serve as biomarkers of neurodegeneration.* Metab Brain Dis, 2022. **37**(1): p. 147-152.
32. Miklossy, J., et al., *Beta-amyloid deposition and Alzheimer's type changes induced by Borrelia spirochetes.* Neurobiol Aging, 2006. **27**(2): p. 228-36.
33. Huang, W.J., X. Zhang, and W.W. Chen, *Role of oxidative stress in Alzheimer's disease.* Biomed Rep, 2016. **4**(5): p. 519-522.

34. Ghazanfar, H., et al., *Hepatic Amyloidosis as a Rare Cause of Liver Failure: A Case Report.* Cureus, 2022. **14**(7): p. e27274.
35. Blencowe, M., et al., *IAPP-induced beta cell stress recapitulates the islet transcriptome in type 2 diabetes.* Diabetologia, 2022. **65**(1): p. 173-187.
36. Hay, D.L., et al., *Amylin: Pharmacology, Physiology, and Clinical Potential.* Pharmacol Rev, 2015. **67**(3): p. 564-600.
37. Schweighauser, M., et al., *Age-dependent formation of TMEM106B amyloid filaments in human brains.* Nature, 2022. **605**(7909): p. 310-314.
38. Westermark, P., A. Andersson, and G.T. Westermark, *Islet amyloid polypeptide, islet amyloid, and diabetes mellitus.* Physiol Rev, 2011. **91**(3): p. 795-826.
39. Steinebrei, M., et al., *Cryo-EM structure of an ATTRwt amyloid fibril from systemic non-hereditary transthyretin amyloidosis.* Nat Commun, 2022. **13**(1): p. 6398.
40. Turbat-Herrera, E.A., *beta 2-Microglobulin and the kidney: an overview.* Ultrastruct Pathol, 1994. **18**(1-2): p. 99-103.
41. Sharpley, F.A., et al., *Amyloidosis Diagnosed in Solid Organ Transplant Recipients.* Transplantation, 2020. **104**(2): p. 415-420.
42. Holub, D., et al., *Mass Spectrometry Amyloid Typing Is Reproducible across Multiple Organ Sites.* Biomed Res Int, 2019. **2019**: p. 3689091.
43. Westermark, G.T., M. Fandrich, and P. Westermark, *AA amyloidosis: pathogenesis and targeted therapy.* Annu Rev Pathol, 2015. **10**: p. 321-44.
44. Deshayes, S., et al., *Infections and AA amyloidosis: An overview.* Int J Clin Pract, 2021. **75**(6): p. e13966.
45. Rambaran, R.N. and L.C. Serpell, *Amyloid fibrils: abnormal protein assembly.* Prion, 2008. **2**(3): p. 112-7.
46. Wells, C., et al., *The role of amyloid oligomers in neurodegenerative pathologies.* Int J Biol Macromol, 2021. **181**: p. 582-604.
47. Hampel, H., et al., *Precision pharmacology for Alzheimer's disease.* Pharmacol Res, 2018. **130**: p. 331-365.
48. Chuang, E., et al., *Amyloid assembly and disassembly.* J Cell Sci, 2018. **131**(8).
49. Hazenberg, B.P., *Amyloidosis: a clinical overview.* Rheum Dis Clin North Am, 2013. **39**(2): p. 323-45.
50. Lachmann, H.J. and P.N. Hawkins, *Systemic amyloidosis.* Curr Opin Pharmacol, 2006. **6**(2): p. 214-20.
51. Helen J. Lachmann, M.B., B.CHIR., David R. Booth, PH.D., Sussane E. Booth, Alison Bybee, PH.D., Janeta. Gilbertson, Julian D. Gillmore, M.B., B.S., M.D., Mark B. Pepys, M.D., PH.D., AND Philip N. Hawkins, M.B., B.S., PH.D., *Misdiagnosis of*

Hereditary Amyloidosis as AL (Primary) Amyloidosis. The New England Journal of Medicine, 2002. **346**.

52. Raymond L. Comenzo, Y.Z., Carmen Martinez, Keren Osman, and Guillermo A. Herrera, *The tropism of organ involvement in primary systemic amyloidosis: contributions of Ig VL germ line gene use and clonal plasma cell burden.* Immunobiology, 2001. **98**.
53. Theodorakakou, F., et al., *Future Developments in the Treatment of AL Amyloidosis.* Hemato, 2022. **3**(1): p. 131-152.
54. Gertz, R.L.C.a.M.A., *Autologous stem cell transplantation for primary systemic amyloidosis.* Blood, 2002. **99**.
55. Seldin, D.C., et al., *Tolerability and efficacy of thalidomide for the treatment of patients with light chain-associated (AL) amyloidosis.* Clin Lymphoma, 2003. **3**(4): p. 241-6.
56. Rabah, S.A., et al., *Thyroid Hormone Distributor Proteins During Development in Vertebrates.* Front Endocrinol (Lausanne), 2019. **10**: p. 506.
57. Steinhoff, J.S., A. Lass, and M. Schupp, *Biological Functions of RBP4 and Its Relevance for Human Diseases.* Front Physiol, 2021. **12**: p. 659977.
58. Pastorelli, F., et al., *Neurological involvement in Ile68Leu (p.Ile88Leu) ATTR amyloidosis: not only a cardiogenic mutation.* Amyloid, 2021. **28**(3): p. 173-181.
59. Li, Z., et al., *TTR Gly83Arg Mutation: Beyond Familial Vitreous Amyloidosis.* Front Neurol, 2021. **12**: p. 821003.
60. Suhr, O.B., E. Lundgren, and P. Westermark, *One mutation, two distinct disease variants: unravelling the impact of transthyretin amyloid fibril composition.* J Intern Med, 2017. **281**(4): p. 337-347.
61. Ihse, E., et al., *Amyloid fibrils containing fragmented ATTR may be the standard fibril composition in ATTR amyloidosis.* Amyloid, 2013. **20**(3): p. 142-50.
62. Ihse, E., et al., *Variation in amount of wild-type transthyretin in different fibril and tissue types in ATTR amyloidosis.* J Mol Med (Berl), 2011. **89**(2): p. 171-80.
63. Pedro P. Costa, A.S.F., and Fernanda R. Bravo, *Amyloid fibril protein related to prealbumin in familial amyloidotic polyneuropathy.* PNAS, 1978. **75**: p. 4499-4503.
64. Mana Joao Mascarenhas Saraiva, S.B., Pedro P. Costa, and DeWitt S. Goodman, *Amyloid Fibril Protein in Familial Amyloidotic Polyneuropathy, Portuguese Type Definition of Molecular Abnormality in Transthyretin (Prealbumin).* J. Clin. Invest., 1984. **74**: p. 104-119.
65. Nakagawa, M., et al., *Carpal tunnel syndrome: a common initial symptom of systemic wild-type ATTR (ATTRwt) amyloidosis.* Amyloid, 2016. **23**(1): p. 58-63.

66. Isabel Conceição, A.G.-D., Laura Obici, Hartmut H.-J. Schmidt, Damien Simoneau5, Moh-Lim Ong, and Leslie Amass, *Red-flag" symptom clusters in transthyretin familial amyloid polyneuropathy.* Journal of the Peripheral Nervous System, 2016. **21**: p. 5-9.
67. Adams, D., et al., *Patisiran, an RNAi Therapeutic, for Hereditary Transthyretin Amyloidosis.* N Engl J Med, 2018. **379**(1): p. 11-21.
68. Kristen, A.V., et al., *Green tea halts progression of cardiac transthyretin amyloidosis: an observational report.* Clin Res Cardiol, 2012. **101**(10): p. 805-13.
69. Maurer, M.S., et al., *Tafamidis Treatment for Patients with Transthyretin Amyloid Cardiomyopathy.* N Engl J Med, 2018. **379**(11): p. 1007-1016.
70. J Floege , G.E., *Beta-2-microglobulin-associated amyloidosis.* Nephron, 1996. **72**: p. 9-26.
71. C Bernabeu, M.v.d.R., P G Lerch, C P Terhorst, *Beta 2-microglobulin from serum associates with MHC class I antigens on the surface of cultured cells.* Nature, 1984. **308**.
72. Kaneko, S. and K. Yamagata, *Hemodialysis-related amyloidosis: Is it still relevant?* Semin Dial, 2018. **31**(6): p. 612-618.
73. Mink, S.R., et al., *Beta-2-microglobulin expression correlates with high-grade prostate cancer and specific defects in androgen signaling.* The Prostate, 2010. **70**(11): p. 1201-1210.
74. NARITA, F.G.a.I., *Current clinical and pathogenetic understanding of b2-m amyloidosis in long-term haemodialysis patients.* Nephrology, 2003. **8**: p. S45-S49.
75. Martin Tran, G.W.R., and Stuart M. Sprague, *The Pathogenesis of 2-Microglobulin Induced Bone Lesions in Dialysis-Related.* Seminars in Dialysis, 2001. **14**: p. 131-133.
76. Iadanza, M.G., et al., *The structure of a beta2-microglobulin fibril suggests a molecular basis for its amyloid polymorphism.* Nat Commun, 2018. **9**(1): p. 4517.
77. Muta, H., et al., *Amyloid Formation under Complicated Conditions in Which beta2-Microglobulin Coexists with Its Proteolytic Fragments.* Biochemistry, 2019. **58**(49): p. 4925-4934.
78. G. Esposito, R.M., G. Verdone, P. Viglino, H. Hherna´ndez, C.V. Robinson A. Amoresano, F. Dal Piaz, M. Monti, P. Pucci, P. Mangione, M. Stoppini, G. Merlini, G. Ferri, and V. Bellotti, *Removal of the N-terminal hexapeptide from human b2-microglobulin facilitates protein aggregation and fibril formation.* Protein Science, 2000. **9**: p. 831-845.
79. de Rosa, M., et al., *Decoding the Structural Bases of D76N ss2-Microglobulin High Amyloidogenicity through Crystallography and Asn-Scan Mutagenesis.* PLoS One, 2015. **10**(12): p. e0144061.

80. Perfetto, F., et al., *Systemic amyloidosis: a challenge for the rheumatologist.* Nat Rev Rheumatol, 2010. **6**(7): p. 417-29.
81. Drueke, T.B., *Dialysis-related amyloidosis.* Nephrol Dial Transplant, 1998. **13 Suppl 1**: p. 58-64.
82. Yang, M., et al., *Apolipoprotein A-II induces acute-phase response associated AA amyloidosis in mice through conformational changes of plasma lipoprotein structure.* Sci Rep, 2018. **8**(1): p. 5620.
83. Magro-Checa, C., et al., *Successful use of tocilizumab in a patient with nephrotic syndrome due to a rapidly progressing AA amyloidosis secondary to latent tuberculosis.* Amyloid, 2011. **18**(4): p. 235-9.
84. Jyunji Sato , K.K., Toshiyuki Yamada *Accumulation and absorption of serum amyloid A and apolipoprotein E fragments in the course of AA amyloidosis: a study in a mouse model.* Annals of Clinical & Laboratory Science, 2014. **44**.
85. Satoshi Baba*, S.A.M., Toshie Takahashi, Takeshi Kasama, Haruhiko Sugimura, Shoichiro Tsugane, Yoshihiro Tsutsui and Haruyuki Shirasawa, *A novel allelic variant of serum amyloid A, SAA1 y: genomic evidence, evolution, frequency, and implication as a risk factor for reactive systemic AA-amyloidosis.* Human Molecular Genetics, 1995. **4**: p. 1083-1097.
86. Niemi, K., et al., *Serum amyloid A (SAA) activates human mast cells which leads into degradation of SAA and generation of an amyloidogenic SAA fragment.* Biochim Biophys Acta, 2006. **1762**(4): p. 424-30.
87. Gunilla T. Westermark, K.S., Anders Grubb, and Per Westermark, *AA amyloidosis Tissue Component-specific Association of Various Protein AA Subspecies and Evidence of a Fourth SAA Gene Product.* AmericanJournal ofPathology,, 1990. **137**: p. 377-383.
88. G. T. Westermark, K.S.P.W., *Massive Vascular AA-Amyloidosis:A Histologically and Biochemically DistinctiveSubtype of Reactive Systemic Amyloidosis.* Scand J Immunol., 1989. **30**: p. 605-613.
89. Wang, W., P. Khatua, and U.H.E. Hansmann, *Cleavage, Downregulation, and Aggregation of Serum Amyloid A.* J Phys Chem B, 2020. **124**(6): p. 1009-1019.
90. Aguilar-Calvo, P., et al., *Prion and prion-like diseases in animals.* Virus Res, 2015. **207**: p. 82-93.
91. Murakami, T., N. Ishiguro, and K. Higuchi, *Transmission of systemic AA amyloidosis in animals.* Vet Pathol, 2014. **51**(2): p. 363-71.
92. Sorby, R., et al., *Rapid induction of experimental AA amyloidosis in mink by intravenous injection of amyloid enhancing factor.* Amyloid, 2008. **15**(1): p. 20-8.

93. Omoto, M., et al., *Inactivation of amyloid-enhancing factor (AEF): study on experimental murine AA amyloidosis.* Med Mol Morphol, 2007. **40**(2): p. 88-94.
94. Manabu Yamada, Y.K., Kikuyasu Nakamura, Yoshiyasu Kobayashi, Noriyuki Horiuchi, Takuya Doi, Satoshi Suzuki, Norihiro Sato, Takeshi Kanno, and Takane Matsui, *Immunohistochemical Distributio of Amyloid Deposits in 25 Cows Diagnosed with Systemic AA Amyloidosis.* J. Vet. Med. Sci., 2006. **68**: p. 725-729.
95. Ishihara, T., et al., *Amyloid protein of vessels in leptomeninges, cortices, choroid plexuses, and pituitary glands from patients with systemic amyloidosis.* Human Pathology, 1989. **20**(9): p. 891-895.
96. Kendi Celebi, Z., et al., *Kidney biopsy in AA amyloidosis: impact of histopathology on prognosis.* Amyloid, 2017. **24**(3): p. 176-182.
97. Okuda, Y., et al., *Comparison of the clinical utility of tocilizumab and anti-TNF therapy in AA amyloidosis complicating rheumatic diseases.* Mod Rheumatol, 2014. **24**(1): p. 137-43.
98. Kluve-Beckerman, B., et al., *Antisense oligonucleotide suppression of serum amyloid A reduces amyloid deposition in mice with AA amyloidosis.* Amyloid, 2011. **18**(3): p. 136-46.
99. Bodin, K., et al., *Antibodies to human serum amyloid P component eliminate visceral amyloid deposits.* Nature, 2010. **468**(7320): p. 93-7.
100. Tennent, G.A., L.B. Lovat, and M.B. Pepys, *Serum amyloid P component prevents proteolysis of the amyloid fibrils of Alzheimer disease and systemic amyloidosis.* Proc Natl Acad Sci U S A, 1995. **92**(10): p. 4299-303.
101. Kisilevsky, R., et al., *Arresting amyloidosis in vivo using small-molecule anionic sulphonates or sulphates: implications for Alzheimer's disease.* Nat Med, 1995. **1**(2): p. 143-8.
102. Ancsin, J.B. and R. Kisilevsky, *The heparin/heparan sulfate-binding site on apo-serum amyloid A. Implications for the therapeutic intervention of amyloidosis.* J Biol Chem, 1999. **274**(11): p. 7172-81.
103. Benditt, E.P. and N. Eriksen, *Amyloid protein SAA is associated with high density lipoprotein from human serum.* Proc Natl Acad Sci U S A, 1977. **74**(9): p. 4025-8.
104. Husby, G. and J.B. Natvig, *A serum component related to nonimmunoglobulin amyloid protein AS, a possible precursor of the fibrils.* J Clin Invest, 1974. **53**(4): p. 1054-61.
105. Cohen, A.S. and L.H. Connors, *The pathogenesis and biochemistry of amyloidosis.* The Journal of Pathology, 1987. **151**(1): p. 1-10.

106. Betts, J.C., et al., *The human acute-phase serum amyloid A gene family: structure, evolution and expression in hepatoma cells.* Scand J Immunol, 1991. **34**(4): p. 471-82.
107. Uhlar, C.M. and A.S. Whitehead, *Serum amyloid A, the major vertebrate acute-phase reactant.* Eur J Biochem, 1999. **265**(2): p. 501-23.
108. Sellar, G.C., et al., *The human serum amyloid A protein (SAA) superfamily gene cluster: mapping to chromosome 11p15.1 by physical and genetic linkage analysis.* Genomics, 1994. **19**(2): p. 221-7.
109. Sipe, J., *Revised nomenclature for serum amyloid A (SAA). Nomenclature Committee of the International Society of Amyloidosis. Part 2.* Amyloid, 1999. **6**(1): p. 67-70.
110. Yu, J., et al., *Cloning, expression analysis, and antibacterial propertiesof three serum amyloid A in common carp (Cyprinus carpio).* Fish Shellfish Immunol, 2017. **65**: p. 267-277.
111. Malle, E. and F.C. De Beer, *Human serum amyloid A (SAA) protein: a prominent acute-phase reactant for clinical practice.* Eur J Clin Invest, 1996. **26**(6): p. 427-35.
112. Milan, E., et al., *SAA1 is over-expressed in plasma of non small cell lung cancer patients with poor outcome after treatment with epidermal growth factor receptor tyrosine-kinase inhibitors.* J Proteomics, 2012. **76 Spec No.**: p. 91-101.
113. Ren, Y., et al., *Expression of serum amyloid A in uterine cervical cancer.* Diagn Pathol, 2014. **9**: p. 16.
114. Hari-Dass, R., et al., *Serum amyloid A protein binds to outer membrane protein A of gram-negative bacteria.* J Biol Chem, 2005. **280**(19): p. 18562-7.
115. Shah, C., R. Hari-Dass, and J.G. Raynes, *Serum amyloid A is an innate immune opsonin for Gram-negative bacteria.* Blood, 2006. **108**(5): p. 1751-7.
116. Hu, Z., et al., *Molecular basis for retinol binding by serum amyloid A during infection.* Proc Natl Acad Sci U S A, 2019. **116**(38): p. 19077-19082.
117. Lu, J., et al., *Structural mechanism of serum amyloid A-mediated inflammatory amyloidosis.* Proc Natl Acad Sci U S A, 2014. **111**(14): p. 5189-94.
118. Wang, Y., et al., *Serum amyloid A 2.2 refolds into a octameric oligomer that slowly converts to a more stable hexamer.* Biochem Biophys Res Commun, 2011. **407**(4): p. 725-9.
119. Jayaraman, S., C. Haupt, and O. Gursky, *Thermal transitions in serum amyloid A in solution and on the lipid: implications for structure and stability of acute-phase HDL.* J Lipid Res, 2015. **56**(8): p. 1531-42.
120. Frame, N.M., et al., *Serum amyloid A self-assembles with phospholipids to form stable protein-rich nanoparticles with a distinct structure: A hypothetical function of*

SAA as a "molecular mop" in immune response. J Struct Biol, 2017. **200**(3): p. 293-302.

121. Frame, N.M. and O. Gursky, *Structure of serum amyloid A suggests a mechanism for selective lipoprotein binding and functions: SAA as a hub in macromolecular interaction networks.* Amyloid, 2017. **24**(sup1): p. 13-14.
122. Alavi Naini, S.M. and N. Soussi-Yanicostas, *Heparan Sulfate as a Therapeutic Target in Tauopathies: Insights From Zebrafish.* Front Cell Dev Biol, 2018. **6**: p. 163.
123. Zhang, W., et al., *Heparin-induced tau filaments are polymorphic and differ from those in Alzheimer's and Pick's diseases.* Elife, 2019. **8**.
124. Stephen R. NELSON, M.L., t John T. GALLAGHER,t Edward A. JOHNSON and Mark B. PEPYS, *Isolation and characterization of the integral glycosaminoglycan constituents of human amyloid A and monoclonal light-chain amyloid fibrils.* Biochemical Journal, 1991. **275**.
125. Alan D. Snow, R.B., Henderson Mar, Thomas N. Wight, and Robert Kisilevsky, *A Temporal and Ultrastructural Relationship Between Heparan Sulfate Proteoglycans and AA Amyloid in Experimental Amyloidosis'.* The Journal of Histochemistry and Cytochemistry, 1991. **39**.
126. Maszota-Zieleniak, M., A. Danielsson, and S.A. Samsonov, *The potential role of glycosaminoglycans in serum amyloid A fibril formation by in silico approaches.* Matrix Biol Plus, 2021. **12**: p. 100080.
127. Aguilera, J.J., et al., *Divergent effect of glycosaminoglycans on the in vitro aggregation of serum amyloid A.* Biochimie, 2014. **104**: p. 70-80.
128. Jha, S., et al., *Mechanism of amylin fibrillization enhancement by heparin.* J Biol Chem, 2011. **286**(26): p. 22894-904.
129. Ren, R., et al., *Role of glycosaminoglycan sulfation in the formation of immunoglobulin light chain amyloid oligomers and fibrils.* J Biol Chem, 2010. **285**(48): p. 37672-82.
130. Nunes, Q.M., et al., *The heparin-binding proteome in normal pancreas and murine experimental acute pancreatitis.* PLoS One, 2019. **14**(6): p. e0217633.
131. Noborn, F., et al., *Heparan sulfate dissociates serum amyloid A (SAA) from acute-phase high-density lipoprotein, promoting SAA aggregation.* J Biol Chem, 2012. **287**(30): p. 25669-77.
132. Digre, A., et al., *Heparin interactions with apoA1 and SAA in inflammation-associated HDL.* Biochem Biophys Res Commun, 2016. **474**(2): p. 309-314.
133. Egashira, M., et al., *Identification of regions responsible for heparin-induced amyloidogenesis of human serum amyloid A using its fragment peptides.* Arch Biochem Biophys, 2011. **511**(1-2): p. 101-6.

134. Kisilevsky, J.B.A.a.R., *The Heparin/Heparan Sulfate-binding Site on Apo-serum Amyloid A.* THE JOURNAL OF BIOLOGICAL CHEMISTRY, 1999. **274**(March 12).
135. Jha, N.N., et al., *Characterization of amyloid formation by glucagon-like peptides: role of basic residues in heparin-mediated aggregation.* Biochemistry, 2013. **52**(49): p. 8800-10.
136. So, M., et al., *Heparin-induced amyloid fibrillation of beta2 -microglobulin explained by solubility and a supersaturation-dependent conformational phase diagram.* Protein Sci, 2017. **26**(5): p. 1024-1036.
137. Cardin, A.D. and H.J. Weintraub, *Molecular modeling of protein-glycosaminoglycan interactions.* Arteriosclerosis, 1989. **9**(1): p. 21-32.
138. Vilasi, S., et al., *Heparin induces harmless fibril formation in amyloidogenic W7FW14F apomyoglobin and amyloid aggregation in wild-type protein in vitro.* PLoS One, 2011. **6**(7): p. e22076.
139. Nitani, A., et al., *Heparin-dependent aggregation of hen egg white lysozyme reveals two distinct mechanisms of amyloid fibrillation.* J Biol Chem, 2017. **292**(52): p. 21219-21230.
140. Potter, K.J., et al., *Amyloid formation in human islets is enhanced by heparin and inhibited by heparinase.* Am J Transplant, 2015. **15**(6): p. 1519-30.
141. Li, J.P., et al., *In vivo fragmentation of heparan sulfate by heparanase overexpression renders mice resistant to amyloid protein A amyloidosis.* Proc Natl Acad Sci U S A, 2005. **102**(18): p. 6473-7.
142. Spiess, H.W., *NMR spectroscopy: pushing the limits of sensitivity.* Angew Chem Int Ed Engl, 2008. **47**(4): p. 639-42.
143. Bax, A. and G.M. Clore, *Protein NMR: Boundless opportunities.* J Magn Reson, 2019. **306**: p. 187-191.
144. Rovnyak, D., et al., *Accelerated acquisition of high resolution triple-resonance spectra using non-uniform sampling and maximum entropy reconstruction.* J Magn Reson, 2004. **170**(1): p. 15-21.
145. Li, D., et al., *Non-Uniform and Absolute Minimal Sampling for High-Throughput Multidimensional NMR Applications.* Chemistry, 2018. **24**(45): p. 11535-11544.
146. Takeuchi, K., et al., *15*

N-Detection with TROSY Selection Enables the Study of Large Nondeuterated Macromolecular Systems, in *eMagRes*. 2017. p. 369-380.
147. Pervushin, K., et al., *Attenuated T2 relaxation by mutual cancellation of dipole-dipole coupling and chemical shift anisotropy indicates an avenue to NMR structures of very*

large biological macromolecules in solution. Proc Natl Acad Sci U S A, 1997. **94**(23): p. 12366-71.

148. Prestegard, J.H., C.M. Bougault, and A.I. Kishore, *Residual dipolar couplings in structure determination of biomolecules.* Chem Rev, 2004. **104**(8): p. 3519-40.
149. Levitt, M.H., *Spin Dynamics: Basics of Nuclear Magnetic Resonance, 2nd Ed. John Wiley & Sons.* 2008.
150. Keeler, J., *Understanding NMR Spectroscopy*
151. Andrew, E.R., *Magic Angle Spinning in Solid State n.m.r. Spectroscopy.* Philosophical Transactions of the Royal Society of London, 1981(299(1452)): p. 505-520.
152. Duer, M.J., *Solid-State NMR Spectroscopy Principles and Applications.* 2002.
153. Hartmann, S.R. and E.L. Hahn, *Nuclear Double Resonance in the Rotating Frame.* Physical Review, 1962. **128**(5): p. 2042-2053.
154. Takegoshi, K., S. Nakamura, and T. Terao, *– dipolar-assisted rotational resonance in magic-angle spinning NMR.* Chemical Physics Letters, 2001. **344**(5-6): p. 631-637.
155. Manolikas, T., T. Herrmann, and B.H. Meier, *Protein structure determination from 13C spin-diffusion solid-state NMR spectroscopy.* J Am Chem Soc, 2008. **130**(12): p. 3959-66.
156. Pauli, J., et al., *Backbone and side-chain 13C and 15N signal assignments of the alpha-spectrin SH3 domain by magic angle spinning solid-state NMR at 17.6 Tesla.* Chembiochem, 2001. **2**(4): p. 272-81.
157. Ward, M.E., L.S. Brown, and V. Ladizhansky, *Advanced solid-state NMR techniques for characterization of membrane protein structure and dynamics: application to Anabaena Sensory Rhodopsin.* J Magn Reson, 2015. **253**: p. 119-28.
158. Luca, S., et al., *Secondary chemical shifts in immobilized peptides and proteins: a qualitative basis for structure refinement under magic angle spinning.* J Biomol NMR, 2001. **20**(4): p. 325-31.
159. Cornilescu, G., F. Delaglio, and A. Bax, *Protein backbone angle restraints from searching a database for chemical shift and sequence homology.* J Biomol NMR, 1999. **13**(3): p. 289-302.
160. Addison, B., et al., *Selective One-Dimensional (13)C-(13)C Spin-Diffusion Solid-State Nuclear Magnetic Resonance Methods to Probe Spatial Arrangements in Biopolymers Including Plant Cell Walls, Peptides, and Spider Silk.* J Phys Chem B, 2020. **124**(44): p. 9870-9883.
161. De Paepe, G., et al., *Proton assisted recoupling and protein structure determination.* J Chem Phys, 2008. **129**(24): p. 245101.

162. Hing, A.W., S. Vega, and J. Schaefer, *Transferred-echo double-resonance NMR.* Journal of Magnetic Resonance (1969), 1992. **96**(1): p. 205-209.
163. Jaroniec, C.P., C. Filip, and R.G. Griffin, *3D TEDOR NMR experiments for the simultaneous measurement of multiple carbon-nitrogen distances in uniformly (13)C,(15)N-labeled solids.* J Am Chem Soc, 2002. **124**(36): p. 10728-42.
164. Gopinath, T., et al., *Hybridization of TEDOR and NCX MAS solid-state NMR experiments for simultaneous acquisition of heteronuclear correlation spectra and distance measurements.* J Biomol NMR, 2019. **73**(3-4): p. 141-153.
165. Matlahov, I. and P.C.A. van der Wel, *Hidden motions and motion-induced invisibility: Dynamics-based spectral editing in solid-state NMR.* Methods, 2018. **148**: p. 123-135.
166. Elena, B., et al., *Proton to carbon-13 INEPT in solid-state NMR spectroscopy.* J Am Chem Soc, 2005. **127**(49): p. 17296-302.
167. Meisl, G., et al., *Molecular mechanisms of protein aggregation from global fitting of kinetic models.* Nat Protoc, 2016. **11**(2): p. 252-72.
168. Van Der Spoel, D., et al., *GROMACS: fast, flexible, and free.* J Comput Chem, 2005. **26**(16): p. 1701-18.
169. Hess, B., et al., *GROMACS 4: Algorithms for Highly Efficient, Load-Balanced, and Scalable Molecular Simulation.* J Chem Theory Comput, 2008. **4**(3): p. 435-47.
170. Lindorff-Larsen, K., et al., *Improved side-chain torsion potentials for the Amber ff99SB protein force field.* Proteins, 2010. **78**(8): p. 1950-8.
171. Horn, H.W., et al., *Development of an improved four-site water model for biomolecular simulations: TIP4P-Ew.* J Chem Phys, 2004. **120**(20): p. 9665-78.
172. Mamatkulov, S. and N. Schwierz, *Force fields for monovalent and divalent metal cations in TIP3P water based on thermodynamic and kinetic properties.* J Chem Phys, 2018. **148**(7): p. 074504.
173. Guerrini, M., A. Bisio, and G. Torri, *Combined quantitative (1)H and (13)C nuclear magnetic resonance spectroscopy for characterization of heparin preparations.* Semin Thromb Hemost, 2001. **27**(5): p. 473-82.
174. Khondker, A., R.J. Alsop, and M.C. Rheinstadter, *Membrane-Accelerated Amyloid-beta Aggregation and Formation of Cross-beta Sheets.* Membranes (Basel), 2017. **7**(3).
175. Sundaria, A., et al., *SAA fibrils involved in AA amyloidosis are similar in bulk and by single particle reconstitution: A MAS solid-state NMR study.* J Struct Biol X, 2022. **6**: p. 100069.

176. Liberta, F., et al., *Cryo-EM fibril structures from systemic AA amyloidosis reveal the species complementarity of pathological amyloids.* Nat Commun, 2019. **10**(1): p. 1104.
177. Kotler, S.A., et al., *Differences between amyloid-beta aggregation in solution and on the membrane: insights into elucidation of the mechanistic details of Alzheimer's disease.* Chem Soc Rev, 2014. **43**(19): p. 6692-700.
178. Elenbaas, B.O.W., et al., *Membrane-Catalyzed Aggregation of Islet Amyloid Polypeptide Is Dominated by Secondary Nucleation.* Biochemistry, 2022. **61**(14): p. 1465-1472.
179. Klopfer, K. and F. Hagn, *Beyond detergent micelles: The advantages and applications of non-micellar and lipid-based membrane mimetics for solution-state NMR.* Prog Nucl Magn Reson Spectrosc, 2019. **114-115**: p. 271-283.
180. Zhang, X.X., et al., *Nanodisc-Based Proteomics Identify Caj1 as an Hsp40 with Affinity for Phosphatidic Acid Lipids.* J Proteome Res, 2021. **20**(10): p. 4831-4839.
181. Krishnarjuna, B., et al., *Nanodisc reconstitution of flavin mononucleotide binding domain of cytochrome-P450-reductase enables high-resolution NMR probing.* Chem Commun (Camb), 2021. **57**(39): p. 4819-4822.

Appendix I

Protein Sequence

GFFSFIGEAFQGAGDMWRAY TDMKEAGWKDGDKYFHARGN YDAAQRGPGG VWAAEKISDA RESFQEFFGRGHEDTMADQE ANRHGRSGKDPNYYRPPGLP AKY*

Chemical shifts for SAA fibrils

Chemical shifts are submitted in BMRB under the accession code 51285.

Residue Number	Amino Acid	C	CA	CB	CG	CD
3	PHE	-	54.626	39.240	-	-
4	SER	169.755	54.751	65.501	-	-
5	PHE	171.975	54.181	38.109	-	-
6	ILE	171.735	56.609	38.680	29.378 15.474	-
7	GLY	172.507	49.626	-	-	-
8	GLU	173.488	51.509	30.569	33.358	-
9	ALA	173.623	47.917	21.723	-	-
10	PHE	170.139	53.547	38.186	-	128.378 130.830
11	GLN	172.272	49.698	31.547	33.762	-
12	GLY	169.897	45.877	-	-	-
13	ALA	173.231	47.151	21.162	-	-
14	GLY	167.961	43.005	-	-	-
15	ASP	175.507	48.869	38.808	177.617	-
16	MET	171.941	56.761	29.695	28.190	-
17	TRP	173.390	55.626	31.400	109.238	124.312
18	ARG	169.755	52.308	32.408	24.835	41.584
19	ALA	172.403	46.900	19.618	-	-
20	TYR	172.505	49.703	35.141	124.542	131.359
21	THR	-	55.094	66.492	-	-
22	ASP	170.793	51.859	42.240	173.678	-
23	MET	-	-	-	-	-
24	LYS	172.223	52.131	34.667	-	28.026
25	GLU	171.350	53.171	37.114	180.146	171.350
26	ALA	173.538	47.366	21.067	-	-
27	GLY	168.901	43.005	-	-	-

28	TRP	171.985	53.822	-	109.371	126.300
30	ASP	172.707	52.466	39.339	-	-
31	GLY	173.348	47.267	-	-	-
32	ASP	170.274	53.850	40.329	-	-
43	ALA	172.101	46.765	19.511	-	-
44	ALA	172.299	46.916	19.446	-	-
45	GLN	170.829	51.889	29.161	35.673	-
46	ARG		51.717	33.462	-	42.309
47	GLY	166.033	42.971	-	-	-
48	PRO		59.404	30.922	-	47.677
49	GLY	172.343	45.866	-	-	-
50	GLY	168.095	42.857	-	-	-
51	VAL	168.095	42.857	168.095	42.857 168.095	-
52	TRP	171.486	55.230	29.624	127.783	171.486
53	ALA	48.013	17.733	172.707	-	-
54	ALA		49.506	16.920	-	-
55	GLU	173.342	50.928	30.651	32.975	-
56	LYS	171.763	54.418	34.028	24.827	-
57	ILE	57.491	37.406	16.795	11.530	-
58	SER	172.170	52.926	62.693	-	-
59	ASP	173.672	51.650	39.122	-	-

Appendix II

Publication and Presentation:

Arpita Sundaria, Falk Liberta, Dilan Savran, Riddhiman Sarkar, Natalia Rodina, Carsten Peters, Nadine Schwierz, Christian Haupt, Matthias Schmidt, Bernd Reif, SAA fibrils involved in AA amyloidosis are similar in bulk and by single particle reconstitution: A MAS solid-state NMR study, J. Struct Biol X, 2022. doi: 10.1016/j.yjsbx.2022.100069.

Poster presentation at 4th Ulm Meeting Biophysics of Amyloid Formation, 2020: Solid-state NMR study of SAA amyloid fibrils.

Poster presentation at Düsseldorf-Julich Symposium on Neurodegenerative Diseases, Düsseldorf, 2019: Structural and Kinetics study of Serum Amyloid A – Principal Component of AA amyloidosis.

Poster presentation at EURO/ISMAR, Berlin, 2019: Structural and Kinetics study of Serum Amyloid A – Principal Component of AA amyloidosis